

# THESIS

## DEVELOPING A POWER DISSIPATION MODEL FOR PLANETARY ROLLER SCREWS

for obtaining the  
doctor's degree

specialty  
Mechanical Engineering

delivered by  
INSA de Lyon

defended before the examination committee on  
December 7, 2018

by  
**Sebastian Sandu**

### Jury

Nans	BIBOULET	Associate Professor (INSA de Lyon, France)
Jean-Paul	GIRAUDEAU	Process Development Manager (SKF Motion Technologies, France)
Michele	GUINGAND	Associate Professor (INSA de Lyon, France)
Matthew	JONES	Senior R&D Systems Engineer (Sandia National Laboratories, US)
Jean-Marc	LINARES	Professor (Université Aix-Marseille, France)
Jean-Charles	MARÉ	Professor (INSA de Toulouse, France)
Daniel	NELIAS	Professor (INSA de Lyon, France)

**Supervisors:** Nans Biboulet and Daniel Nelias

**Referees:** Jean-Charles Maré and Matthew Jones

**Research unit:** LaMCoS - UMR CNRS 5259 - INSA de Lyon

**Doctoral school:** MEGA - Université de Lyon





# INSA

N°d'ordre NNT : 2018LYSEI096

**THESE de DOCTORAT DE L'UNIVERSITE DE LYON**  
opérée au sein de  
**l'Institut National des Sciences Appliquées de Lyon**

**École Doctorale N° ED162**  
**MEGA**

**Spécialité/ discipline de doctorat :**

Génie Mécanique

Soutenue publiquement le 07/12/2018 par :  
**Sebastian Sandu**

---

**Développement d'un modèle de  
dissipation de puissance pour les vis à  
rouleaux planétaires**

---

Devant le jury composé de :

Linares, Jean-Marc	Professeur des Universités	Univ. d'Aix-Marseille	Président
Jones, Matthew	Senior R&D Systems Engineer	Sandia National Labs	Rapporteur
Maré, Jean-Charles	Professeur des Universités	INSA Toulouse	Rapporteur
Guingand, Michele	Maître de conférences	INSA Lyon	Examinatrice
Biboulet, Nans	Maître de conférences	INSA Lyon	Codirecteur de thèse
Nelias, Daniel	Professeur des Universités	INSA Lyon	Directeur de thèse
Giraudeau, Jean-Paul	Process Development Manager	SKF Motion Tech	Invité

**Département FEDORA – INSA Lyon - Ecoles Doctorales – Quinquennal 2016-2020**

<b>SIGLE</b>	<b>ECOLE DOCTORALE</b>	<b>NOM ET COORDONNEES DU RESPONSABLE</b>
<b>CHIMIE</b>	<b>CHIMIE DE LYON</b> <a href="http://www.edchimie-lyon.fr">http://www.edchimie-lyon.fr</a> Sec. : Renée EL MELHEM Bât. Blaise PASCAL, 3e étage <a href="mailto:secretariat@edchimie-lyon.fr">secretariat@edchimie-lyon.fr</a> INSA : R. GOURDON	<b>M. Stéphane DANIELE</b> Institut de recherches sur la catalyse et l'environnement de Lyon IRCELYON-UMR 5256 Équipe CDFA 2 Avenue Albert EINSTEIN 69 626 Villeurbanne CEDEX <a href="mailto:directeur@edchimie-lyon.fr">directeur@edchimie-lyon.fr</a>
<b>E.E.A.</b>	<b>ÉLECTRONIQUE, ÉLECTROTECHNIQUE, AUTOMATIQUE</b> <a href="http://edeea.ec-lyon.fr">http://edeea.ec-lyon.fr</a> Sec. : M.C. HAVGOUDOUKIAN <a href="mailto:ecole-doctorale.eea@ec-lyon.fr">ecole-doctorale.eea@ec-lyon.fr</a>	<b>M. Gérard SCORLETTI</b> École Centrale de Lyon 36 Avenue Guy DE COLLONGUE 69 134 Écully Tél : 04.72.18.60.97 Fax 04.78.43.37.17 <a href="mailto:gerard.scorletti@ec-lyon.fr">gerard.scorletti@ec-lyon.fr</a>
<b>E2M2</b>	<b>ÉVOLUTION, ÉCOSYSTÈME, MICROBIOLOGIE, MODÉLISATION</b> <a href="http://e2m2.universite-lyon.fr">http://e2m2.universite-lyon.fr</a> Sec. : Sylvie ROBERJOT Bât. Atrium, UCB Lyon 1 Tél : 04.72.44.83.62 INSA : H. CHARLES <a href="mailto:secretariat.e2m2@univ-lyon1.fr">secretariat.e2m2@univ-lyon1.fr</a>	<b>M. Philippe NORMAND</b> UMR 5557 Lab. d'Ecologie Microbienne Université Claude Bernard Lyon 1 Bâtiment Mendel 43, boulevard du 11 Novembre 1918 69 622 Villeurbanne CEDEX <a href="mailto:philippe.normand@univ-lyon1.fr">philippe.normand@univ-lyon1.fr</a>
<b>EDISS</b>	<b>INTERDISCIPLINAIRE SCIENCES-SANTÉ</b> <a href="http://www.ediss-lyon.fr">http://www.ediss-lyon.fr</a> Sec. : Sylvie ROBERJOT Bât. Atrium, UCB Lyon 1 Tél : 04.72.44.83.62 INSA : M. LAGARDE <a href="mailto:secretariat.ediss@univ-lyon1.fr">secretariat.ediss@univ-lyon1.fr</a>	<b>Mme Emmanuelle CANET-SOULAS</b> INSERM U1060, CarMeN lab, Univ. Lyon 1 Bâtiment IMBL 11 Avenue Jean CAPELLE INSA de Lyon 69 621 Villeurbanne Tél : 04.72.68.49.09 Fax : 04.72.68.49.16 <a href="mailto:emmanuelle.canet@univ-lyon1.fr">emmanuelle.canet@univ-lyon1.fr</a>
<b>INFOMATHS</b>	<b>INFORMATIQUE ET MATHÉMATIQUES</b> <a href="http://edinfomaths.universite-lyon.fr">http://edinfomaths.universite-lyon.fr</a> Sec. : Renée EL MELHEM Bât. Blaise PASCAL, 3e étage Tél : 04.72.43.80.46 Fax : 04.72.43.16.87 <a href="mailto:infomaths@univ-lyon1.fr">infomaths@univ-lyon1.fr</a>	<b>M. Luca ZAMBONI</b> Bât. Braconnier 43 Boulevard du 11 novembre 1918 69 622 Villeurbanne CEDEX Tél : 04.26.23.45.52 <a href="mailto:zamboni@maths.univ-lyon1.fr">zamboni@maths.univ-lyon1.fr</a>
<b>Matériaux</b>	<b>MATÉRIAUX DE LYON</b> <a href="http://ed34.universite-lyon.fr">http://ed34.universite-lyon.fr</a> Sec. : Marion COMBE Tél : 04.72.43.71.70 Fax : 04.72.43.87.12 Bât. Direction <a href="mailto:ed.materiaux@insa-lyon.fr">ed.materiaux@insa-lyon.fr</a>	<b>M. Jean-Yves BUFFIÈRE</b> INSA de Lyon MATEIS - Bât. Saint-Exupéry 7 Avenue Jean CAPELLE 69 621 Villeurbanne CEDEX Tél : 04.72.43.71.70 Fax : 04.72.43.85.28 <a href="mailto:jean-yves.buffiere@insa-lyon.fr">jean-yves.buffiere@insa-lyon.fr</a>
<b>MEGA</b>	<b>MÉCANIQUE, ÉNERGÉTIQUE, GÉNIE CIVIL, ACOUSTIQUE</b> <a href="http://edmega.universite-lyon.fr">http://edmega.universite-lyon.fr</a> Sec. : Marion COMBE Tél : 04.72.43.71.70 Fax : 04.72.43.87.12 Bât. Direction <a href="mailto:mega@insa-lyon.fr">mega@insa-lyon.fr</a>	<b>M. Jocelyn BONJOUR</b> INSA de Lyon Laboratoire CETHIL Bâtiment Sadi-Carnot 9, rue de la Physique 69 621 Villeurbanne CEDEX <a href="mailto:jocelyn.bonjour@insa-lyon.fr">jocelyn.bonjour@insa-lyon.fr</a>
<b>ScSo</b>	<b>ScSo*</b> <a href="http://ed483.univ-lyon2.fr">http://ed483.univ-lyon2.fr</a> Sec. : Viviane POLSINELLI Brigitte DUBOIS INSA : J.Y. TOUSSAINT Tél : 04.78.69.72.76 <a href="mailto:viviane.polsinelli@univ-lyon2.fr">viviane.polsinelli@univ-lyon2.fr</a>	<b>M. Christian MONTES</b> Université Lyon 2 86 Rue Pasteur 69 365 Lyon CEDEX 07 <a href="mailto:christian.montes@univ-lyon2.fr">christian.montes@univ-lyon2.fr</a>

\*ScSo : Histoire, Géographie, Aménagement, Urbanisme, Archéologie, Science politique, Sociologie, Anthropologie

# Résumé

Les vis à rouleaux convertissent la rotation en translation de manière très efficace et sont utilisées dans des nombreuses industries. Mais même s'il présente beaucoup d'avantages, le mécanisme reste complexe et relativement difficile à comprendre. Le principal but de cette thèse est de quantifier la puissance dissipée par les vis à rouleaux standard et inversées, qui est un résultat important pour toute étude liée à l'efficacité ou la distribution de température. De plus, il s'agit d'un critère de conception dans le choix de paramètres optimaux pour une certaine application.

À cause des travaux peu nombreux en termes de recherche et des hypothèses restrictives faites dans la littérature courante, ce mémoire commence avec une analyse géométrique de base du mécanisme et envisage de généraliser les équations des surfaces filetées pour les différents types de profils et conditions de jeu. La position des points de contact peut ensuite être déduite avec un algorithme de type Newton-Raphson très rapide. Cette information est cruciale pour toute étude ultérieure de force. Après, les équations classiques de Hertz sont adaptées à des contacts peu conformes pour déterminer la forme, les dimensions et l'orientation des ellipses de contact rouleau-vis et rouleau-douille. Il est prouvé que les directions principales de courbure obtenues ici par géométrie différentielle sont différentes de celles supposées dans les précédents travaux de recherche.

Ensuite, la cinématique du mécanisme est étudiée avec un modèle stationnaire, qui établit des liens entre les mouvements uniformes de tous les composants et permet de calculer d'une manière simplifiée le champ de vitesse de glissement en tout point de l'aire de contact. Le mouvement local apparaît comme une combinaison de spin et de glissement uniforme. Le modèle est calibré sur un seul degré de liberté qui prend la forme d'un quotient de glissement, qui dépend de conditions de lubrification et équations d'équilibre dynamique. Un banc expérimental est conçu pour mesurer ce quotient et permettre donc la comparaison avec des valeurs numériques, ainsi que les quelques modèles analytiques disponibles dans la littérature. Les résultats montrent que les mesures sont très proches des conditions de fonctionnement idéales, ce qui fait que les propriétés du lubrifiant et les coefficients de frottement deviennent les paramètres les plus influents dans le peu de marge disponible pour l'amélioration cinématique.

Finalement, un modèle numérique en forces est développé et permet de calculer la puissance dissipée pendant l'équilibre stationnaire. L'algorithme itératif détermine d'abord le quotient de glissement atteint à l'équilibre et utilise ensuite le résultat pour déduire les autres variables cinématiques et dynamiques liées au calcul. Une étude paramétrique est réalisée dans le but d'identifier les facteurs importants pour l'efficacité et la puissance dissipée, ainsi que leur contribution relative.

## Mots-clés:

contact filet  
quotient de glissement  
couple de spin  
puissance dissipée  
vis à rouleaux



# Abstract

Roller screws are highly efficient rotation-translation converters used in a variety of industries. Despite its numerous advantages, the mechanism remains complex and rather difficult to understand. The main goal of this thesis is to quantify the amount of power dissipated by standard and inverted roller screws, which is an important result for any study related to efficiency or temperature distribution. Furthermore, it is used as a design criterion in choosing optimal parameters for a given application.

Due to the limited amount of available research and the restrictive assumptions made in current literature, this memoir starts with a basic geometric analysis of the mechanism and attempts to generalize threaded surface equations for different types of profiles and backlash conditions. The contact point locations can then be deduced using a very fast Newton-Raphson algorithm. This information is crucial for any subsequent force analysis. Classic Hertzian equations are then adapted to slightly conforming contacts in order to calculate the shape, size and orientation of the roller-screw and roller-nut contact ellipses. It is shown that the principal directions of curvature obtained here by differential geometry are different from the ones assumed by previous research.

Next, the mechanism kinematics is investigated using a stationary model, which relates the steady-state movement of all the different components and allows a simplified calculation of the sliding velocity field at any point within the contact areas. The local motion proves to be a combination of spin and uniform sliding. The model is set to have only one degree of freedom in the form of a slip ratio, which depends on lubrication conditions and force balance equations. An experimental setup is designed to measure this ratio and thus allow comparison to numerical values, as well as the few analytical models available in the literature. Results show that measurements are very close to ideal operating conditions, which makes lubricant properties and friction coefficients the most influential parameters in the little room available for kinematic improvement.

Finally, a numerical force model is developed, which calculates the power dissipated during the steady-state regime. The iterative algorithm first determines the value of the slip ratio reached during stationary equilibrium and then uses the result to deduce the other kinematic and dynamic unknowns involved. A parametric study is conducted to identify the important factors in efficiency and power dissipation, as well as their relative influence.

**Keywords:**

thread contact  
slip ratio  
spin torque  
dissipated power  
roller screw

# Contents

Notation	viii
General introduction	1
<b>1 Roller screw geometry</b>	<b>4</b>
1.1 Introduction	4
1.2 Threaded surface equations	5
1.2.1 Convex profile	7
1.2.2 Concave profile	8
1.2.3 Straight profile	9
1.2.4 External unit normal	10
1.3 Surface assembly	12
1.3.1 Backlash conditions	13
1.3.2 Number of rollers	15
1.3.3 Design and Simulation	16
1.4 Hertzian contact ellipse	18
1.4.1 Orientation	19
1.4.2 Shape	22
1.4.3 Size	23
1.5 Application examples	24
1.5.1 Example 1: Simulation of a standard PRS	24
1.5.2 Example 2: Design of an inverted PRS	25
1.5.3 Example 3: Influence of pitch	26
1.5.4 Example 4: Influence of profile curvatures	27
1.6 Conclusion	28
<b>2 Stationary regime kinematics</b>	<b>30</b>
2.1 Introduction	30
2.2 Global slip model	30
2.2.1 Sliding velocity at contact points	33
2.2.2 Kinematic constraints	34
2.2.3 Experimental results	36
2.2.4 Comparison with literature	39
2.3 Local contact model	39
2.3.1 Friction coefficient	41
2.3.2 Numerical results	43
2.4 HFRR measurements	45
2.5 Conclusion	47
<b>3 Dynamics and dissipated power</b>	<b>48</b>
3.1 Introduction	48
3.2 Stationary equilibrium model	48
3.2.1 Sliding friction	51
3.2.2 Spin torques	51

3.2.3	Normal loads . . . . .	52
3.2.4	Static equilibrium . . . . .	52
3.2.5	Auxiliary contributions . . . . .	54
3.2.6	Dynamic equilibrium . . . . .	56
3.2.7	Algorithm convergence . . . . .	59
3.2.8	Power dissipation . . . . .	61
3.2.9	Efficiency . . . . .	63
3.3	Parametric study . . . . .	63
3.4	Conclusion . . . . .	65
	<b>Main conclusions</b>	<b>67</b>
	<b>A Contact points location algorithm</b>	<b>69</b>
	<b>B Principal curvatures and directions</b>	<b>73</b>
	B.1 Numerical application . . . . .	75
	<b>C Parametric study figures</b>	<b>77</b>
	<b>Bibliography</b>	<b>81</b>

# Notation

$a$	[m]	(> 0) major Hertz contact ellipse half-diameter
$b$	[m]	(> 0) minor Hertz contact ellipse half-diameter
$c$	[m]	(> 0) radial distance between screw/nut/carrier and roller axes
$C_{I,J}$	[Nm]	contact spin torque at $I$ or $J$
$C_{S,N}$	[Nm]	external torque on the Screw or Nut
$D_z$	[m]	total backlash, $D_z = D_{zS} + D_{zN}$
$D_{zS}, D_{zN}$	[m]	Screw-roller or Nut-roller axial play
$E'$	[Pa]	relative Young modulus of elasticity, see Eq. 1.79
$F_{S,N}$	[N]	external force on the Screw or Nut
$h(r_m)$	[m]	shape function, depending on the thread profile
$h', h''$	[, 1/m]	first and second derivatives of $h(r_m)$
$h_c$	[m]	(> 0) central lubrication film thickness
$H$	[ ]	( $0 \leq H \leq 1$ ) mechanism efficiency, see Eq. 3.52
$k$	[ ]	( $\geq 1$ ) ellipticity ratio, $k = a/b$
$K$	[m]	(> 0) geometrical constant $K = p \cos \beta/4$
$l$	[m]	lead; if right-handed: $l > 0$ , left-handed: $l < 0$ ; in general: $ l  = np$
$\vec{m}$	[, , ]	modified normal at $I$ or $J$ due to friction, $\vec{m} = \vec{n} - \mu_{I,J} \vec{t}_{I,J}$
$n$	[ ]	( $\geq 1$ ) number of thread starts
$\vec{n}$	[, , ]	surface/contact unit normal vector at point $M$
$N_{I,J}$	[N]	( $\geq 0$ ) contact normal load at $I$ or $J$
$N_C$	[ ]	number of $I$ or $J$ contacts per roller
$N_R$	[ ]	number of rollers
$p$	[m]	(> 0) axial pitch of the threaded profile
$P_h$	[Pa]	maximum Hertzian contact pressure, see Eq. 1.83
$P_D$	[Pa]	discretized contact pressure, see Eq. 2.28
$r_B$	[m]	(> 0) profile curvature radius
$r_m, \theta_m, z_m$	[m,rad,m]	cylindrical coordinates for a point on the threaded surface
$r_{min,max}$	[m]	(> 0) minimal/maximal values for $r_m$
$r_{IS}, \theta_{IS}$	[m,rad]	polar coordinates of $I$ from the Screw axis
$r_{IR}, \theta_{IR}$	[m,rad]	polar coordinates of $I$ from the Roller axis
$r_{JN}, \theta_{JN}$	[m,rad]	polar coordinates of $J$ from the Nut axis
$r_{JR}, \theta_{JR}$	[m,rad]	polar coordinates of $J$ from the Roller axis
$r_T$	[m]	nominal (pitch) radius of the thread $T$
$s$	[m <sup>2</sup> ]	surface of the Hertz contact ellipse, $s = \pi ab$
$T_{I,J}$	[N]	( $\geq 0$ ) total friction force for contact $I$ or $J$
$\vec{t}_{I,J}$	[, , ]	total friction force direction at point $I$ or $J$
$\vec{t}_{1,2}$	[, , ]	principal directions of curvature at point $M$
$\vec{u}_{t/p}(M)$	[m/s,m/s,m/s]	sum (rolling) velocity of ( $t$ ) with respect to ( $p$ ) at point $M$
$\vec{v}_{t/p}(M)$	[m/s,m/s,m/s]	relative (sliding) velocity of ( $t$ ) with respect to ( $p$ ) at point $M$
$W_t$	[W]	( $\leq 0$ ) total power dissipated by the PRS mechanism
$x, y, z$	[m,m,m]	Cartesian coordinates
$\dot{z}_{n/s}$	[m/s]	lead speed (along $z$ ) of the nut ( $n$ ) with respect to the screw ( $s$ )

$\alpha$	[1/Pa]	(> 0) pressure-viscosity coefficient
$\alpha_g$	[rad]	gear pressure angle, usually $\pi/9$
$\alpha_n$	[rad]	normal pressure angle, usually around $\pi/4$
$\alpha_x$	[rad]	axial pressure angle, $\tan \alpha_x = \tan \alpha_n / \cos \beta$
$\beta$	[rad]	thread helix angle; if right-handed: $\beta > 0$ , left-handed: $\beta < 0$
$\gamma$	[ ]	indicator for the top face of the thread (-1) or the bottom face (+1)
$\Gamma$	[ ]	(> 0) gear (overdrive) ratio, see Eq. 2.1
$\epsilon$	[ ]	( $0 \leq \epsilon \leq 1$ ) non-dimensional slip ratio, $\epsilon = \omega_{p/n} / \omega_{s/n}$
$\epsilon^*$	[ ]	theoretically ideal value of $\epsilon$ , see Eqs. 2.16 and 2.17
$\eta$	[Pa·s]	dynamic viscosity of the lubricant
$\lambda$	[ ]	non-dimensional ratio related to $\epsilon$ by Eq. 2.4
$\mu$	[ ]	friction coefficient
$\rho_{1,2}$	[1/m]	principal curvatures, $ \rho_1  \leq  \rho_2 $
$\tau_0$	[Pa]	(> 0) Eyring stress
$\chi$	[ ]	boolean indicator of the PRS type: 1 for standard and 0 for inverted
$\omega_{s/n}$	[rad/s]	angular speed along $z$ of the screw ( $s$ ) with respect to the nut ( $n$ )

I	roller-screw contact point
J	roller-nut contact point
PRS	abbreviation for Planetary Roller Screw



# General introduction

Screws are powerful rotation-translation converters which profoundly changed the way people lived throughout history. In antiquity, they were used to raise water and produce wine and olive oil. Today, we use them to adjust the mirrors in space telescopes. But even though the screw has undergone many changes and optimization, its basic principle remains the same. Many types of screws exist nowadays, with the classic friction screw primarily used as a fastener being the most widely-spread. Also known as a bolt, it consists of an externally threaded shaft in direct contact with an internally threaded nut.

In order to reduce the relatively high amount of friction, rolling elements (balls or threaded cylinders) can be introduced between the screw shaft and the nut. We would then obtain ball screws or roller screws, respectively. Roller screws, in particular, have very high efficiencies (around 80% [1]) and are well suited for applications that require heavy-duty, high precision and high loads [2]. They were invented in the 1950s by Carl Bruno Strandgren, who filed a series of patents [3–9] and their remarkable qualities have persuaded engineers to consider them as a replacement for hydraulic cylinders [10]. Their relatively low weight and compactness make them useful in a variety of fields, including aeronautics, cars, robotics, the medical and space industries.

Although several types of roller screws exist today, the most common ones, shown in Fig. 2, are:

1. planetary or satellite roller screws (PRS)
  - (a) standard
  - (b) inverted
2. recirculating roller screws (RRS)

The three main components of a roller screw (screw shaft, rollers and nut) are all threaded, but their number of starts can be different. Several geometric and kinematic conditions must be maintained if the mechanism is to function correctly. While these conditions have been extensively studied [2, 12–14], reality shows that it is virtually impossible to satisfy all of them simultaneously. This is mainly due to elastic deformations, wear and manufacturing imperfections. For these reasons, a planet carrier and a system of gears are added, such that the mechanism works similarly to an epicyclic gear train, with the addition of axial movement and a small amount of circumferential slip [14]. The gears were already present in the initial patent [4].

In a standard PRS, for example, there is no axial movement between the nut and the rollers i.e. these components are part of an assembly that translates on the screw. This condition requires the roller thread helix angle to be the same for the nut, such that the peaks of the rollers fit perfectly inside the gaps of the nut. Furthermore, the two components must roll with no sliding with respect to each other. The introduction of gears between the parts that are not supposed to exhibit relative axial movement (in this case, rollers and nut) forces the rollers to move to their correct positions.

Inverted PRS work in a similar way, but helix angles are matched and gears placed between the screw and the rollers instead of the nut and the rollers. The recirculating RS, however, is fundamentally different, since all the roller helix angles are nil. Hence, roller axial movement is allowed with respect to both the screw shaft and the nut, which eliminates the need for gears. A

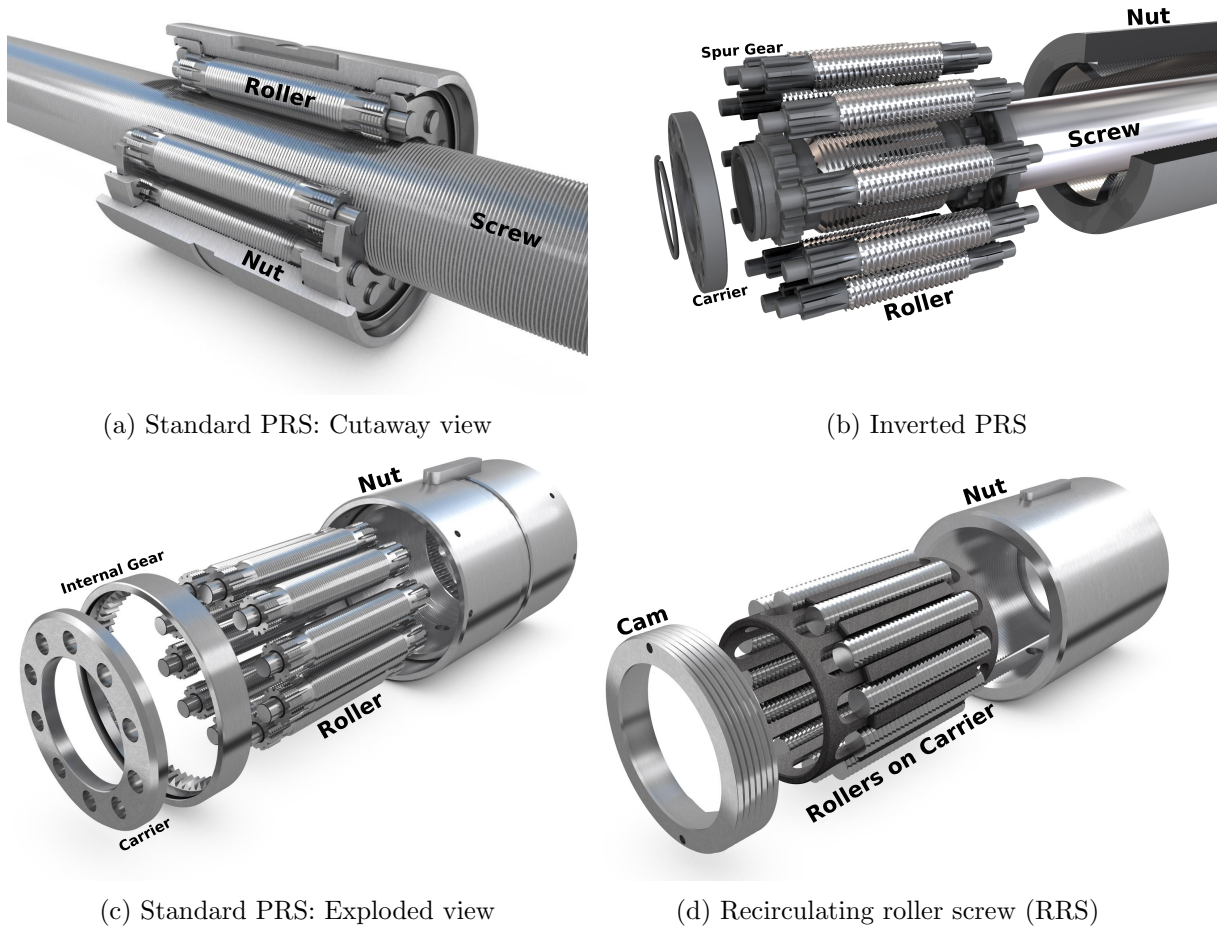


Figure 2: Different types of roller screws [11]

system of cams (see Fig. 2d) is added instead, preventing rollers from escaping the mechanism after a few rotations.

The introduction of gears to constantly correct the position of the rollers only works if the pitch diameter of the gear and thread are identical, otherwise a phenomenon known as roller migration occurs [15]. As shown by Zhang and Zhao [16, 17], it is possible to machine the two features at the same time and thus ensure a good synchronization. This reduces the axial displacement error to a very small percentage ( $< 0.01\%$  in [1]), making the roller screw one of the most precise rotation-translation converters there is. Further studies on the transmission accuracy have been performed by Ma et al. [18] under MSC Adams and by Mamaev et al. [19, 20] on an experimental apparatus for the PRS used in a radio telescope.

Depending on the way the load is distributed through the mechanism, some thread contacts can deform more than others [21, 22]. This effect was investigated in the static case by Abevi et al. [10, 23, 24], who developed finite elements models on an inverted PRS. For standard roller screws, the axial stiffness has been studied by Ma et al. [25], Jones and Velinsky [26] and Zhang et al. [27]. Finally, for the transient, dynamic case, Fu et al. [28] proposed a semi-analytical model which uses a linear distribution for the normal contact forces on the different roller threads. The model assumes all solids to be infinitely rigid. Moreover, roller backlash is considered along all three possible directions (radial, transversal and axial).

Other researchers focused on specific aspects of the mechanism, like Aurégan et al. [29, 30] who studied the stick/slip distribution within the contact areas and the damage modes related to a specific coating. Sokolov et al. [31] developed principles for evaluating wear resistance. The thermal aspect was analyzed using a 2D finite elements model in ANSYS [32]. The model uses the frictional moment deduced in reference [25].

While much effort was put into this research, in many cases no experimental data was used

to verify the results. We believe that measurements on a real mechanism are the best way to validate any proposed theory. Furthermore, some of the endurance tests undertaken by our industrial partner have revealed a significant increase in the mechanism's temperature at high speeds and loads. A more complete understanding of the roller screw geometry and kinematics was required before any attempt to provide a reliable explanation for the temperature increase. Eventually, a dynamic model which takes lubrication into account was necessary for identifying the most influential parameters related to power dissipation and the generated heat.

The current manuscript is the result of three years of research on the roller screw mechanism. The developed equations are designed to work for both standard and inverted PRS, although measurements and examples are mainly focused on the standard type, which is more common.

The first chapter deals with the global geometry, thread profile definitions and location of the contact points. All solids are assumed to be infinitely rigid, although a model for investigating contact areas is also developed. The local contact geometry is treated as a consequence of loading, with no influence on the shape of the different components. Only axial backlash is allowed, such that rollers always stay parallel with the screw and nut axes.

Roller screw kinematics and lubrication are investigated in the second chapter. We propose a stationary model based on the amount of circumferential slip in the mechanism, which is measured through experiments. The model also defines sliding velocities inside the contact areas to show the difference between roller-screw and roller-nut interfaces. Results are used in a lubrication model to calculate local friction coefficients.

Finally, the third chapter presents a stationary force equilibrium model which calculates the amount of slip numerically and thus eliminates the need to perform experiments for each particular case. The mechanism efficiency and dissipated power are also computed and used as performance criteria in a parametric study. This study identifies the most important variables involved in the roller screw design process, as well as their relative influence.

The main hypotheses made throughout the current work are summarized below:

1. The global geometry is composed of infinitely rigid solids
2. Local contact deformations have no effect on the global geometry
3. All rollers are identical
4. All roller-screw thread contacts are identical
5. All roller-nut thread contacts are identical
6. The screw and nut axis are identical at all times
7. The rollers and screw axis are parallel at all times
8. Gears are machined such that there is no roller migration

# Chapter 1

## Roller screw geometry

### 1.1 Introduction

The thread geometry and location of the contact points are the first steps in any study involving forces in the roller screw, yet most of the current literature proposes verified models only for some particular mechanisms. A few general methods exist, but their complexity makes them hard to apply from an engineering point of view. Moreover, a unifying geometrical background that works for both standard and inverted PRS was needed. Finally, some authors have published overly simplifying and/or inaccurate results which can lead to confusion. A simple, yet effective solution to these issues was recently proposed by the authors of this work [11]. In this chapter, elements from references [11, 14] are combined in a more legible fashion with regard to the structure of the present memoir. A few novelties are included as well.

Roller screw geometry has been studied by many authors. One of the earliest studies on the location of contact points was proposed by Jones and Velinsky [33]. Their analytical model can be applied to both planetary and recirculating roller screws, but does not take backlash into account and profile shapes cannot be modified. Moreover, we found some of the geometrical assumptions to be inaccurate, as detailed in appendix A of this thesis.

Another analysis was later proposed by Liu et al. [13] for standard roller screws where all the thread profiles are assumed to be straight. The paper shows that any contact between screw and rollers occurs along a curve when all solids are infinitely rigid. In our view, only a line could be obtained in such a case; the line would then shrink to a point as the roller curvature increases. The influence of the roller profile shape was investigated by the authors in a later article [34], and it was found that among the three studied profiles (circular, elliptical and parabolic), the elliptical one gives the best results. However, we found that the proposed analytical solution is inaccurate, as detailed in the third example in the current chapter. Furthermore, reference [34] does not consider backlash at all.

Backlash along all three directions (radial, transversal and axial) was eventually considered in a numerical model proposed recently by Fu et al. [35]. Even though only standard roller screws are studied, manufacturing errors can also be included by modifying the pitch radius by a small amount. This confirms a requirement mentioned by Fedosovsky et al. [36] in earlier work, which states that backlash cannot be guaranteed unless one of the components is rectified during the design process. On the other hand, reference [34] assumes the thread profiles to be straight for the screw and nut, and the influence of other profile shapes is not studied. Furthermore, the location of the contact points is only given as a general expression with matrices and no details regarding computer implementation or algorithm performance are given.

Another important subject in terms of roller screw geometry concerns the shape, size and orientation of the contact areas between threads. This topic has received little attention from the research community, yet is of significant importance in choosing the optimal mechanism dimensions for a given application. Fu et al. [28] used the Hertzian theory to model contact areas, but without explaining how to obtain information about the ellipses. Principal surface curvatures and directions of curvature are important model inputs, yet current literature [12, 33]

provides results without a clear justification. In this work, differential geometry is used to obtain values which prove to be different.

Based on the advantages and shortcomings of current literature, the present chapter investigates the thread geometry for both standard and inverted PRS. The shapes of our profiles are different from existing models and they are defined in the normal plane perpendicular to the thread helix. This plane is more representative from the perspective of the tool tip machining the surfaces. We also present the implementation details of a very fast Newton-Raphson algorithm which computes the location of the contact points in 3D space for any combination of profile curvatures.

The algorithm assumes all roller-screw contacts to be identical and the same for all the roller-nut contacts. This hypothesis is not strictly true in reality, but allows much simpler equations to be developed. All solids are treated as being infinitely rigid and local deformations are neglected with respect to the global geometry and location of the contact points. Only axial backlash is taken into account. This leads to a simple, yet effective method in designing and simulating the roller screw geometry.

## 1.2 Threaded surface equations

First of all, we consider the external surface of a threaded shaft presented in Fig. 1.1. Any point  $M$  on this surface is entirely defined by the cylindrical coordinates  $(r_m, \theta_m, z_m)$ . The axial thread profile is defined as the section view obtained by cutting the shaft along the  $zx$  plane. In the general case when the thread's helix angle  $\beta$  is non-nil, this plane will not be perpendicular to the thread's direction. As shown in the figure, it is necessary to rotate the  $zx$  plane by an angle  $\beta$  around the  $x$  axis in order to obtain the normal thread profile. During this process distances measured along  $x$  remain constant, while distances along  $z$  are distorted by a factor  $\cos \beta$  such that:

$$z' = z \cos \beta \quad (1.1)$$

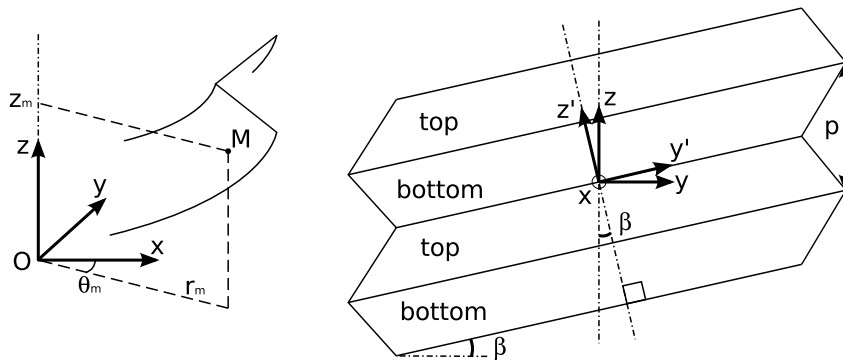


Figure 1.1: Axial frame  $(xyz)$ , cylindrical coordinates  $(r_m, \theta_m, z_m)$  and normal frame  $(xy'z')$

The axial  $z$  distance between two thread peaks is called the pitch  $p$  and is always positive. However, this is not necessarily equal to the axial distance traveled by the thread in one complete turn, which is called the lead  $l$ . Pitch and lead have the same value for common friction screws, but roller screws usually contain threaded parts with multiple starts, such that in the general case:

$$|l| = np \quad (1.2)$$

where  $n$  is a positive integer representing the number of thread starts. For the rollers in recirculating roller screws where the helix angle  $\beta$  is nil,  $n$  and  $l$  will also be nil. In the general case, however, the lead is positive for right-handed threads (like the ones represented in Figs. 1.1-1.2) and negative for left-handed threads.

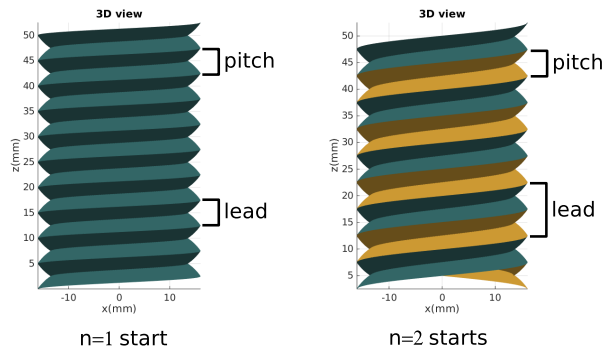


Figure 1.2: Lead and pitch

The helix angle  $\beta$  follows the same sign rules as the lead and is defined as:

$$\tan \beta = \frac{l}{2\pi r_T} \quad (1.3)$$

where  $r_T$  is the nominal or pitch radius of the threaded shaft  $T$ . It represents the half-diameter where, from an axial point of view, there is as much solid matter as empty space. As it will be shown in the following sections, this radius is neither the inner nor the outer half-diameter. Instead, it is located between the two radii, at a point where contact with another thread would likely occur.

Let us now focus on writing the corresponding threaded surface equations. In order to manipulate continuous and differentiable functions, it is convenient to separate the surface in two parts, here called *top* and *bottom*. For determining which is which, imagine the following scenario: if the threaded component is placed vertically in the rain, water falls on the *top* face. For an externally threaded shaft, the two sides are represented in Fig. 1.1.

One way to write the surface equation is to express the axial  $z_m$  coordinate of any point  $M$  on the surface as a function of its radial and circumferential coordinates ( $r_m$  and  $\theta_m$ , respectively). Since the thread is constructed by revolution along a helical path, variations of  $z_m$  along  $\theta_m$  will be linear. It is thus sufficient to study the geometry of the threaded profile in order to obtain the desired function.

We decided to study three types of profiles, named straight, convex and concave. Straight profiles represent the classic V-shape of friction screws, often encountered in practice. Since they are cheap to make, these profiles are usually used in the context of roller screws for machining the screw and nut parts. Rollers, on the other hand, usually have a curvy, bumped profile for minimizing the contact area, reducing wear and prolonging the working lifetime of the mechanism [10]. If the roller profile were straight as well, we would obtain a line contact instead of a point, even with infinitely rigid geometry. This scenario was investigated by Liu et al. [13] and is not considered in this memoir.

In order to model the bump, we define convex profiles using circular arcs in the normal plane. When transported in the axial plane, these arcs stretch and become elliptical. We were inspired in this choice by the original roller screw design proposed by Strandgren [4]. Moreover, Liu et al. [34] recently published a comparison between axially circular, parabolic and elliptical roller profiles and it was found that elliptical threads provide the best performance among the three. However, other ways to represent the bump also exist (see Morozov et al. [37] for involute profiles, for example).

Our goal was to make equations general enough, so that the screw and the nut could also take convex profiles like the rollers. Later on in this work, we study the influence of profile shapes on the mechanism's performance, which justifies some of the choices which are made during the design process. Therefore, threaded surface equations had to be made independent of the component they are attached to. Furthermore, since the nut is an internal thread, this means that a convex nut profile actually appears concave when seen from the inside. For this reason, specific equations were developed for a new profile shape, called concave.

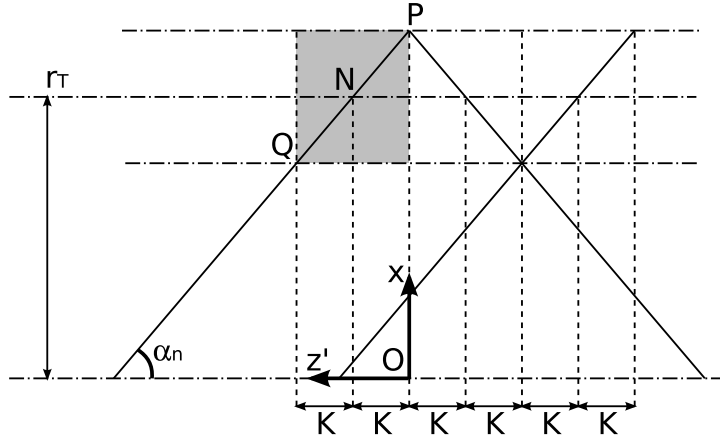


Figure 1.3: Common profile sketch in the normal plane for thread  $T$

All of our profiles are constructed on a common sketch represented in Fig. 1.3, which was obtained in the following way:

1. First of all, we considered that the nominal radius  $r_T$  of thread  $T$  (screw, roller or nut) is a known geometrical parameter. This allowed us to place point  $N$  at a distance  $r_T$  from the  $z'$  axis.
2. Secondly, we assumed that the normal pressure angle  $\alpha_n$  is also known. By definition, this angle is formed by the  $z'$  axis and a line passing through  $N$ . In practice, it is often close to  $\pi/4$ .
3. Next, if the lead and the number of starts of the thread are known, it is possible to calculate the pitch and the helix angle. We define a constant  $K$  for the thread  $T$  such that:

$$K = \frac{p \cos \beta}{4} \quad (1.4)$$

In the normal plane, length  $K$  represents one quarter of the distance between two consecutive thread peaks. We placed points  $P$  and  $Q$  on the pressure line on either side of  $N$  such that the  $z'$  projection of segments  $NP$  and  $NQ$  is of length  $K$ . Since the nominal radius  $r_T$  was defined as the half-diameter where there is as much empty space as solid matter, all profile shapes must include point  $N$  and be situated inside the rectangle of diagonal  $PQ$  (i.e. grey area in Fig. 1.3).

4. Finally, the surface origin  $O$  was taken to be the projection of point  $P$  on the axis. This allows to switch between the  $z'$  coordinates of the *top* and *bottom* faces simply by changing their sign.

### 1.2.1 Convex profile

The first roller screw designs proposed by Strandgren [4] suggest that slightly convex thread profiles are better. Today, most manufacturers still machine the rollers according to his drawings, i.e. considering that the thread profile is composed of circle parts centred on the axis and of radius

$$r_B = \frac{r_T}{\sin \alpha_n} \quad (1.5)$$

where  $\alpha_n$  is the normal pressure angle.

Such a profile is represented in red in Fig. 1.4. It was constructed using circle parts of radius  $r_B$  and center  $C$  such that  $C$  is placed at the intersection of the  $z'$  axis with the  $PQ$  line. Some authors suggested that normal contact forces are transmitted along this line [38], but that is not necessarily true.

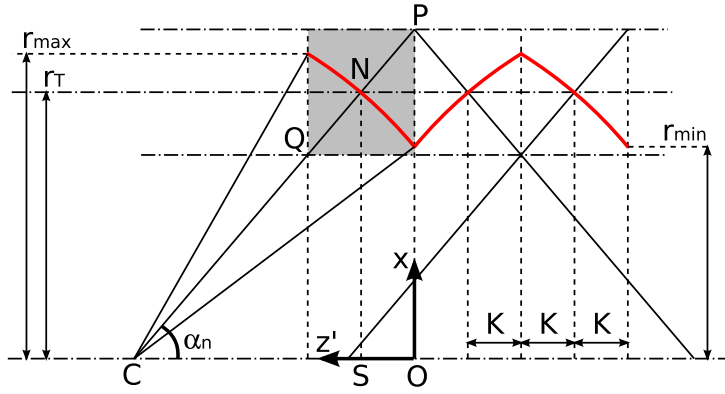


Figure 1.4: Normal convex profile (red) on the common profile sketch (black)

For any point  $M(r_m, z'_m)$  on the profile, the circle equation allows to write:

$$(r_m - x_C)^2 + (z'_m - z'_C)^2 = r_B^2 \quad (1.6)$$

where the coordinates of point  $C$  are:

$$x_C = 0 \quad (1.7)$$

$$z'_C = K + r_B \cos \alpha_n \quad (1.8)$$

This translates into:

$$z'_m = K + r_B \cos \alpha_n - \sqrt{r_B^2 - r_m^2} \quad (1.9)$$

which is true for the *bottom* face of an external thread and  $\theta_m = 0$ . In the general case, we can deduce that:

$$z_m = \frac{\gamma}{\cos \beta} \left( K + r_B \cos \alpha_n - \sqrt{r_B^2 - r_m^2} \right) + \frac{\theta_m l}{2\pi} \quad (1.10)$$

Equation 1.10 expresses the surface equation of an external thread with a convex profile. In order to draw multiple-threaded parts like the screw in a PRS,  $n$  individual threads would need to be drawn with a  $z$  shift of  $p$  between them. Unless the total length of the threaded part is specified, the angle  $\theta_m$  can take any real value, while  $r_m$  must be situated in the interval  $[r_{min}, r_{max}]$ , as shown in Fig. 1.4. These limit values can be calculated using the circle equation:

$$\begin{cases} (r_{min} - x_C)^2 + (-z'_C)^2 & = r_B^2 \\ (r_{max} - x_C)^2 + (2K - z'_C)^2 & = r_B^2 \end{cases} \quad (1.11)$$

yielding:

$$\begin{cases} r_{min} = \sqrt{r_B^2 - (r_B \cos \alpha_n + K)^2} \\ r_{max} = \sqrt{r_B^2 - (r_B \cos \alpha_n - K)^2} \end{cases} \quad (1.12)$$

### 1.2.2 Concave profile

As with the convex profile, it is possible to imagine a concave one as shown in red in Fig. 1.5. Like in the previous section, the center  $C$  is on the  $PQ$  line. Writing the corresponding thread surface equation is useful for modeling a convex nut, since the thread is internal and the profile actually appears concave. The coordinates of point  $C$  can be deduced from triangle  $CSN$ :

$$\sin \alpha_n = \frac{x_C - r_T}{r_B} \Rightarrow x_C = r_T + r_B \sin \alpha_n \quad (1.13)$$

$$\cos \alpha_n = \frac{K - z'_C}{r_B} \Rightarrow z'_C = K - r_B \cos \alpha_n \quad (1.14)$$

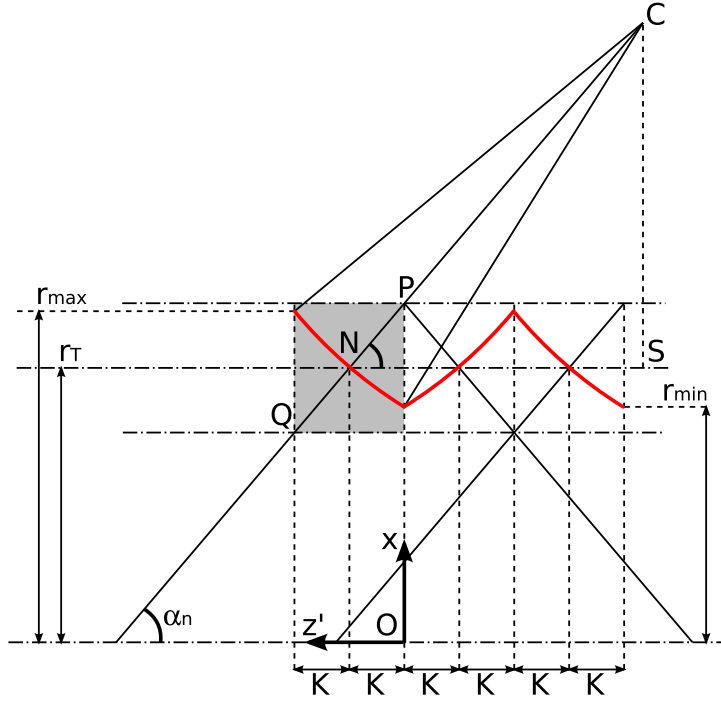


Figure 1.5: Normal concave profile (red) on the common profile sketch (black)

For any point  $M(r_m, z'_m)$  on the profile, it can be deduced from the circle equation that:

$$z'_m = K - r_B \cos \alpha_n + \sqrt{r_B^2 - (r_m - r_T - r_B \sin \alpha_n)^2} \quad (1.15)$$

which under the general form is written:

$$z_m = \frac{\gamma}{\cos \beta} \left( K - r_B \cos \alpha_n + \sqrt{r_B^2 - (r_m - r_T - r_B \sin \alpha_n)^2} \right) + \frac{\theta_m l}{2\pi} \quad (1.16)$$

Equation 1.16 expresses the surface equation of a thread with a concave profile. In this form, it is valid for external threads, but internal ones can be deduced simply by changing the sign  $\gamma$ . The limit values  $[r_{min}, r_{max}]$  can be deduced in the same way as before:

$$\begin{cases} r_{min} = r_T + r_B \sin \alpha_n - \sqrt{r_B^2 - (K - r_B \cos \alpha_n)^2} \\ r_{max} = r_T + r_B \sin \alpha_n - \sqrt{r_B^2 - (K + r_B \cos \alpha_n)^2} \end{cases} \quad (1.17)$$

### 1.2.3 Straight profile

In practice, mainly due to cost issues, it is often interesting to produce threads with straight profiles like the one shown in red in Fig. 1.6. These profiles are also commonly used in the literature [2, 33, 38] for their simplicity and consist of segments perpendicular to the pressure line  $PQ$ .

It is possible to find several other angles equal to  $\alpha_n$  and write that:

$$\tan \alpha_n = \frac{2K}{r_{max} - r_{min}} = \frac{K}{r_T - r_{min}} \quad (1.18)$$

which yields:

$$\begin{cases} r_{min} = r_T - \frac{K}{\tan \alpha_n} \\ r_{max} = r_T + \frac{K}{\tan \alpha_n} \end{cases} \quad (1.19)$$

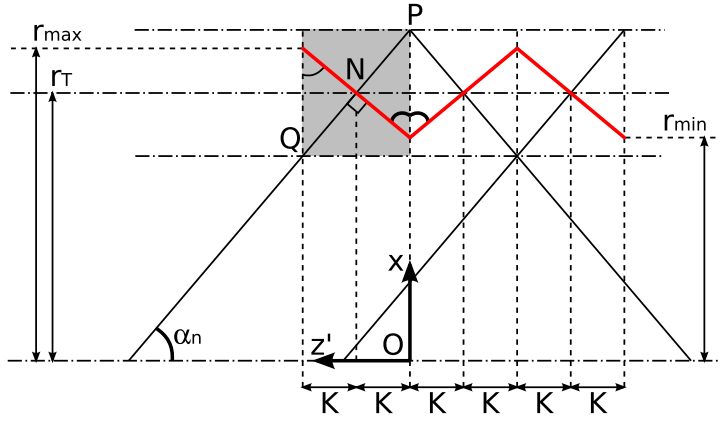


Figure 1.6: Normal straight profile (red) on the common profile sketch (black)

For any point  $M(r_m, z'_m)$  on the profile, we can write that:

$$z'_m = (r_m - r_{min}) \tan \alpha_n \quad (1.20)$$

and generalize it into:

$$z_m = \frac{\gamma}{\cos \beta} (K + (r_m - r_T) \tan \alpha_n) + \frac{\theta_m l}{2\pi} \quad (1.21)$$

Equation 1.21 expresses the surface equation of an external thread with a straight profile. It is completely defined using the same parameters as before, with the exception of  $r_B$ . Furthermore, it is possible to calculate the limit for  $r_B \rightarrow \infty$  in Eq. 1.16 and we would obtain Eq. 1.21. This is the expected behaviour since the profile tends to flatten as the radius of curvature increases.

In conclusion, all the profile shapes used in the current work can be defined using a limited number of independent parameters, which are summarized in table 1.1.

$\gamma$	boolean indicating either the <i>top</i> face (-1) or <i>bottom</i> face (+1)
$r_T$	nominal or pitch radius of the thread $T$
$r_B$	curvature radius of the thread profile
$\alpha_n$	normal pressure angle
$l$	lead of the thread
$n$	number of starts on the threaded surface

Table 1.1: Minimal list of parameters used to define any threaded surface

#### 1.2.4 External unit normal

In the previous sections we showed that all the threaded surface equations based on convex, straight or concave profile shapes can be expressed under the form:

$$z_m(r_m, \theta_m) = \frac{\gamma}{\cos \beta} h(r_m) + \frac{\theta_m l}{2\pi} \quad (1.22)$$

where  $h(r_m)$  is the  $z'_m$  coordinate, a function which depends on the profile shape. One of the main advantages of this form is that it allows an easy calculation of the external unit normal vector at any point. For any 3D surface defined by an equation  $f(r, \theta, z) = 0$ , the normal

direction is given by the gradient  $\overrightarrow{\nabla f}$  which can be written as:

$$\overrightarrow{\nabla f}(r, \theta, z) = \begin{bmatrix} \frac{\partial f}{\partial r} \\ \frac{1}{r} \frac{\partial f}{\partial \theta} \\ \frac{\partial f}{\partial z} \end{bmatrix}_{\vec{e}_r, \vec{e}_\theta, \vec{e}_z} = \begin{bmatrix} \frac{\partial f}{\partial r} \cos \theta - \frac{1}{r} \frac{\partial f}{\partial \theta} \sin \theta \\ \frac{\partial f}{\partial r} \sin \theta + \frac{1}{r} \frac{\partial f}{\partial \theta} \cos \theta \\ \frac{\partial f}{\partial z} \end{bmatrix}_{\vec{x}, \vec{y}, \vec{z}} \quad (1.23)$$

In this particular case,  $f$  can be chosen such that:

$$f(r_m, \theta_m, z_m) = \frac{\gamma}{\cos \beta} h(r_m) + \frac{\theta_m l}{2\pi} - z_m \quad (1.24)$$

which means that its derivatives are:

$$\frac{\partial f}{\partial r_m} = \frac{\gamma}{\cos \beta} h'; \quad \frac{\partial f}{\partial \theta_m} = \frac{l}{2\pi}; \quad \frac{\partial f}{\partial z_m} = -1; \quad \text{where } h' = \frac{dh}{dr_m} \quad (1.25)$$

Hence, the vector  $\overrightarrow{\nabla f}$  always points in the negative  $z$  direction, but this is not always the case for the threaded surface's outwards normal vector. It only works for the *bottom* face. In general, an extra factor  $\gamma$  is thus needed such that:

$$\vec{n} = \gamma \frac{\overrightarrow{\nabla f}}{\|\overrightarrow{\nabla f}\|} \quad (1.26)$$

This translates into the following expression for the external unit normal in Cartesian coordinates:

$$\vec{n}(r_m, \theta_m) = \frac{1}{\sqrt{\left(\frac{h'}{\cos \beta}\right)^2 + \left(\frac{l}{2\pi r_m}\right)^2 + 1}} \begin{bmatrix} \frac{h'}{\cos \beta} \cos \theta_m - \frac{\gamma l}{2\pi r_m} \sin \theta_m \\ \frac{h'}{\cos \beta} \sin \theta_m + \frac{\gamma l}{2\pi r_m} \cos \theta_m \\ -\gamma \end{bmatrix} = \frac{-1}{\sqrt{n_x^2 + n_y^2 + 1}} \begin{bmatrix} n_x \\ n_y \\ \gamma \end{bmatrix} \quad (1.27)$$

As mentioned earlier, the function  $h(r_m)$  depends on the shape of the threaded profile. Table 1.2 summarizes the first and second derivatives of  $h$  for the convex, straight and concave profiles studied in this work.

The above considerations are true for externally threaded shafts, but can also be used for internal threads (like the nut in a PRS) if we describe the shape of the air volume contained within. This work does not provide any supplementary formulas for internally threaded parts. Instead, we describe the geometry of the space which is exactly complementary to the one occupied by the internally threaded component.

The general Eq. 1.27 for the external unit normal vector at any point can be used to deduce the contact location between two threaded surfaces. If we assume that at least one of the infinitely rigid surfaces has a curved profile, the contact will be a collection of single points; lines would be obtained only if both surfaces were straight [13]. Some very particular curvature combinations that involve concave profiles might even lead to multiple contact points or no contact, but as they are unlikely to be found on usual roller screw designs, are not considered in this memoir. The resulting system of equations is non-linear and has to be solved numerically, but the details of a very efficient algorithm which computes the solution are given in appendix A.

profile	convex	straight	concave
$h'$	$\frac{1}{\sqrt{m^2 - 1}}$	$\tan \alpha_n$	$\frac{1}{\sqrt{m^2 - 1}}$
$h''$	$\frac{m^3}{r_B(m^2 - 1)^{3/2}}$	0	$\frac{m^3}{r_B(m^2 - 1)^{3/2}}$
$m$	$\frac{r_T}{r_m \sin \alpha_n}$		$\frac{1}{\frac{r_m - r_T}{r_B} - \sin \alpha_n}$

Table 1.2: Derivatives of  $h(r_m)$

### 1.3 Surface assembly

Let us now focus on assembling the different roller screw surfaces together. We use S,R,N to denote the surface of the screw, roller or nut, respectively. To ensure that the mechanism works as intended, the pitch  $p$  must be the same for all three of them. For the purposes of the current work, the pressure angle  $\alpha_n$  is also considered to be a constant.

Figure 1.7 depicts the typical PRS design, such that the screw and the nut are coaxial, while the roller axis is placed at a distance  $c$  from the other two components. Roller-screw contacts will be referred to as  $I$  and roller-nut contacts as  $J$ . The figure also provides a zoom on the roller, with some dimensions exaggerated for clarity.

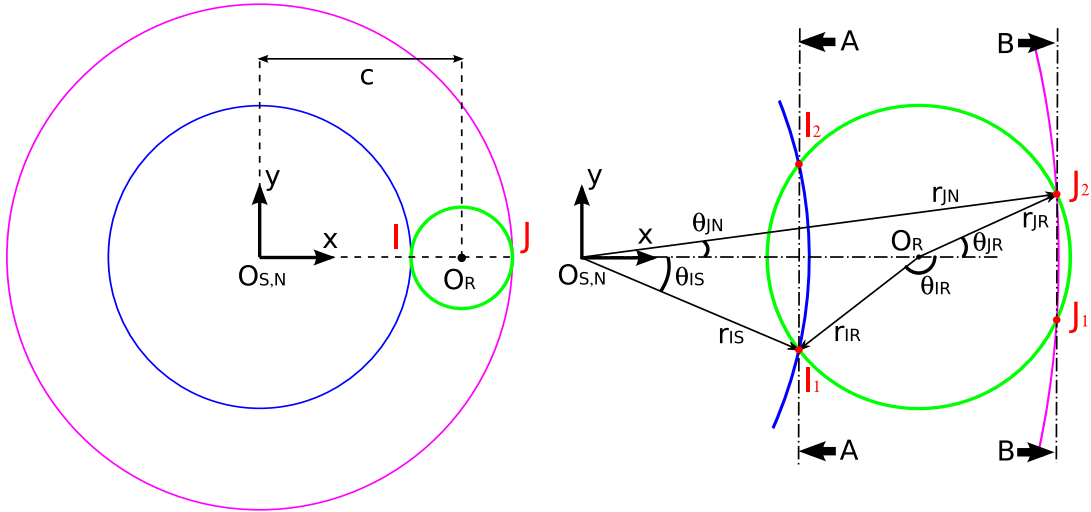
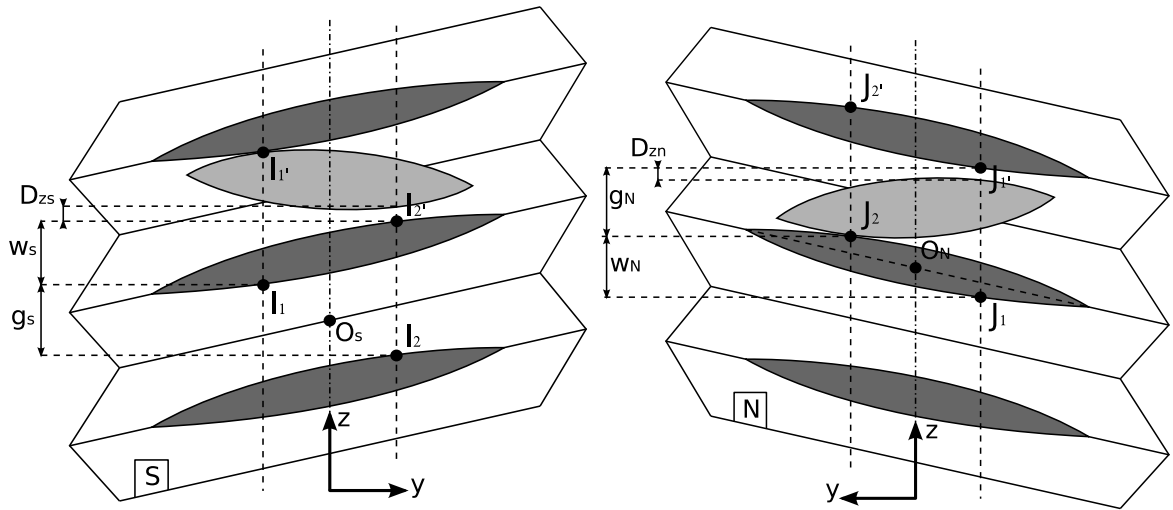


Figure 1.7: Surface assembly and zoom: screw(blue), roller(green), nut(magenta)

A rough approximation assumes that points  $I$  and  $J$  are placed on the  $O_S O_R$  line. Several authors [2,12] use this assumption due to its simplicity. In reality, however, the locations of  $I$  and  $J$  are shifted and have to be calculated using an algorithm like the one presented in appendix A. Reference [33] used solid modeling to show that  $I$  is not collinear to the two origins. A section view similar to Fig. 1.8a was obtained.

In general, the PRS mechanism allows for axial play i.e. even if no components are turning, it is possible to move the parts axially with respect to each other for a small distance. This distance is called backlash and is denoted  $D_z$ . It can be suppressed by introducing a custom amount of preload during machining or assembly [1], but in the general case it can be present. Throughout this work, we will consider that it is composed of two possible displacements, one between the roller and the nut and the other between the screw and the roller such that:

$$D_z = D_{zS} + D_{zN} \quad (1.28)$$



(a) Screw surface: section AA (for a standard PRS) (b) Nut surface: section BB (for an inverted PRS)

Figure 1.8: Section views for the  $I_1J_2$  configuration

The presence of backlash means there are actually two possible locations for the  $I$  and  $J$  contacts, depending on the direction in which the mechanism is operated. They will be identified with subscripts 1 and 2. Figure 1.8a was drawn for the first configuration, where the screw threads (dark grey) touch the roller threads (light grey) at points  $I_1, I_1', etc.$  which correspond to the screw's *bottom* face and the roller's *top* face. As shown in appendix A, switching the  $\gamma$  orientation of the surfaces does not change the corresponding radii of contact, only the sign of the contact angles. This means that the second configuration can easily be deduced by symmetry.

Even if it may seem like any of the four combinations of  $I$  and  $J$  contacts is possible, the load transfer in the mechanism imposes only two global functioning modes, which were also mentioned in [33]:

$I_1J_2$ : screw *bottom*  $\rightarrow$  roller *top*  $\rightarrow$  roller *bottom*  $\rightarrow$  nut *top*

$I_2J_1$ : screw *top*  $\rightarrow$  roller *bottom*  $\rightarrow$  roller *top*  $\rightarrow$  nut *bottom*

Note that Figs. 1.8a – 1.8b were drawn for the  $I_1J_2$  configuration in the general case and do not represent the same roller screw.

While the radial and circumferential coordinates of the contact points  $I$  and  $J$  can be determined using the algorithm in appendix A, the  $z$  (axial) coordinates cannot be calculated by simply applying the threaded surface Eqs. 1.10, 1.16 or 1.21. These equations refer to individual surface origins, which may be shifted axially due to backlash conditions.

### 1.3.1 Backlash conditions

We will now explain how to calculate the backlash and relative  $z$  position of the origins of the different surfaces in a PRS, when the radial and circumferential coordinates of the contact points are known. First of all, we consider the screw surface represented in Fig. 1.8a. For simplicity, the surface is right-threaded, although equations are true for both orientations.

Based on the convex, straight or concave profile definitions, the origin  $O_S$  is always situated on the axis such that its projection on the surface corresponds to the minimal radius. Let's assume it is placed as shown in Fig. 1.8a. The  $z$  coordinates of  $I_1$  and  $I_2$  can then be calculated with Eq. 1.22:

$$z_{I_1S} = \frac{1}{\cos \beta_S} h(r_{IS}) + \frac{\theta_{IS} l_S}{2\pi} \quad (1.29)$$

$$z_{I_2S} = \frac{-1}{\cos \beta_S} h(r_{IS}) - \frac{\theta_{IS} l_S}{2\pi} \quad (1.30)$$

which means that:

$$z_{I_2S} = -z_{I_1S} \quad (1.31)$$

The axial coordinates of the two contact points are thus opposite. Due to the form of equation 1.22, we can see that this holds true for all the surfaces studied in this work.

We define the gap  $g_S$  as the empty-space axial distance between two consecutive contact points and the axial thread width  $w_S$  such that:

$$w_S = p - g_S \quad (1.32)$$

It can be seen from the figure that:

$$g_S = -\overrightarrow{I_1I_2} \cdot \vec{z} = z_{I_1S} - z_{I_2S} = 2z_{I_1S} \quad (1.33)$$

Let's now consider the surface of the nut. As shown in Fig. 1.8b, since the thread is internal we have:

$$w_N = \overrightarrow{J_1J_2} \cdot \vec{z} = z_{J_2N} - z_{J_1N} = 2z_{J_2N} \quad (1.34)$$

$$g_N = p - w_N \quad (1.35)$$

On the nut side, the roller surface is similar to the screw presented before and we have:

$$w_{RN} = p - g_{RN} \quad (1.36)$$

$$g_{RN} = \overrightarrow{J_1J_2} \cdot \vec{z} = z_{J_2R} - z_{J_1R} = 2z_{J_2R} \quad (1.37)$$

On the screw side, however, things are slightly more complicated for the roller, as shown in Fig. 1.9. Since the contact angle  $\theta_{IR}$  is large (close to  $-\pi$ ),  $I_1$  and  $I_2$  will be rather far from each other. Let  $I_{1''}$  be the position of point  $I_1$  after one complete turn. The figure was drawn for a right-handed thread, but the same can be done with a left thread to prove that:

$$w_{RS} = p - g_{RS} \quad (1.38)$$

$$g_{RS} = z_{I_2R} - z_{I_{1''}R} = z_{I_2R} - (z_{I_1R} + l_R) = -l_R - 2z_{I_1R} \quad (1.39)$$

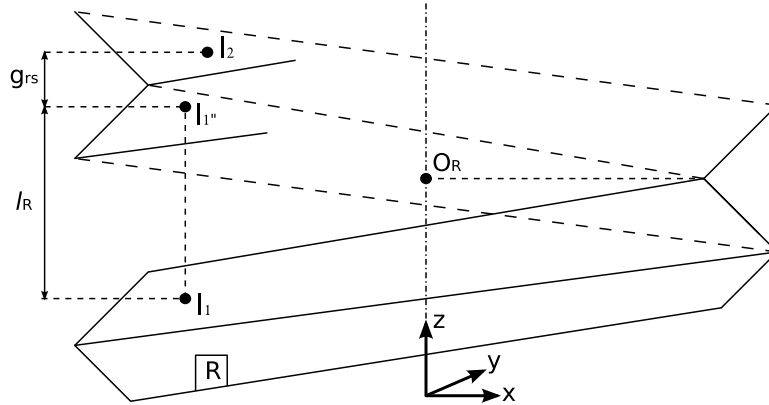


Figure 1.9: 3D representation of the roller surface

We can now define the backlash as the difference between the gap of the screw or nut and the width of the roller threads:

$$\begin{aligned} D_{zS} &= g_S - w_{RS} = 2(z_{I_1S} - z_{I_1R}) - l_R - p \\ D_{zN} &= g_N - w_{RN} = 2(z_{J_2R} - z_{J_2N}) \end{aligned} \quad (1.40)$$

where  $l_R$  is the lead of the roller and  $p$  the pitch. In this formula, the  $z$  coordinates are obtained simply by applying equation 1.22 to the different surfaces.

Once the backlash is known, we can easily calculate the relative  $z$  position of the surface origins. For the  $I_1J_2$  configuration we have:

$$\overrightarrow{O_R O_N}(J_2) \cdot \vec{z} = \left( \overrightarrow{O_R J_2} - \overrightarrow{O_N J_2} \right) \cdot \vec{z} = z_{J_2 R} - z_{J_2 N} = \frac{D_{zN}}{2} \quad (1.41)$$

$$\overrightarrow{O_R O_S}(I_1) \cdot \vec{z} = \left( \overrightarrow{O_R I_1} - \overrightarrow{O_S I_1} \right) \cdot \vec{z} = z_{I_1 R} - z_{I_1 S} = -\frac{l_R + p}{2} - \frac{D_{zS}}{2} \quad (1.42)$$

and for the  $I_2J_1$  configuration:

$$\overrightarrow{O_R O_N}(J_1) \cdot \vec{z} = \overrightarrow{O_R O_N}(J_2) \cdot \vec{z} - D_{zN} = -\frac{D_{zN}}{2} \quad (1.43)$$

$$\overrightarrow{O_R O_S}(I_2) \cdot \vec{z} = \overrightarrow{O_R O_S}(I_1) \cdot \vec{z} + D_{zS} = -\frac{l_R + p}{2} + \frac{D_{zS}}{2} \quad (1.44)$$

### 1.3.2 Number of rollers

Figure 1.7 only sketches one roller. In reality, however, there are at least three of them, equally spaced. Furthermore, there is also a maximum number of rollers that can fit into any given screw-nut geometry.

As illustrated in Fig. 1.10, two adjacent rollers will interfere on their outer radii unless the corresponding separation angle is greater than a minimal value such that:

$$\sin \frac{\theta_{min}}{2} = \frac{r_{maxR}}{c} \quad (1.45)$$

where  $c$  is the distance between the screw/nut and roller axis and  $r_{maxR}$  the maximum radius of the roller profile.

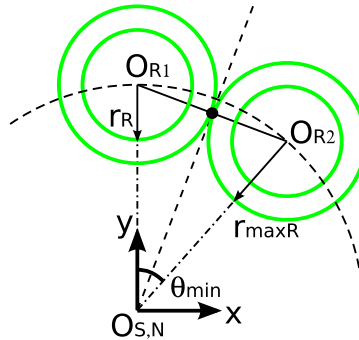


Figure 1.10: Adjacent rollers in interference

On the other hand, the number of rollers is related to the separation angle  $\theta$  such that:

$$\theta = \frac{2\pi}{N_R} \quad (1.46)$$

which means that the maximum number of rollers for a given mechanism can be expressed as:

$$N_{Rmax} = \left\lfloor \frac{\pi}{\sin^{-1} \left( \frac{r_{maxR}}{c} \right)} \right\rfloor \quad (1.47)$$

where  $\lfloor \cdot \rfloor$  represents the floor function defined as:

$$\lfloor x \rfloor = \max\{m \in \mathbb{Z} \mid m \leq x\} \quad (1.48)$$

Equation 1.47 is similar to the one obtained by Ma et al. [12]. It means that the number of rollers must be chosen such that:

$$3 \leq N_R \leq N_{Rmax} \quad (1.49)$$

### 1.3.3 Design and Simulation

Finally, this section investigates how to fully define the geometry of a roller screw mechanism, based on the user's intent and a minimum number of input parameters. We have identified two methods, depending whether the user's goal is to simulate an existing mechanism or to create one theoretically based on given specifications. These two methods will be called *simulation* and *design*, respectively, and consist in establishing a list of variables that allows all the other geometrical unknowns to be calculated. Here we only focus on the threaded components and assume that the geometry of secondary parts (gears, planet carrier, retaining rings) could easily be deduced. The two methods are presented in table 1.3 and were implemented in a program for both standard and inverted PRS.

<b>Input</b>	<b>Simulation</b>	<b>Design</b>
-	product type: standard or inverted PRS	
$r_S > 0$	measured pitch radius for the screw	target pitch radius for the screw
$r_R > 0$	measured pitch radius for the roller	-
$r_N > 0$	measured pitch radius for the nut	-
$l_S > 0$	lead of the screw	
$n_S > 0$	number of starts on the screw	
$n_R > 0$	number of starts on the roller	
$\alpha_n \simeq \pi/4$	normal pressure angle	
$\pm 1/r_{BS}$	screw curvature: straight (0), convex (+) or concave (-)	
$\pm 1/r_{BR}$	roller curvature: straight (0), convex (+) or concave (-)	
$\pm 1/r_{BN}$	nut curvature: straight (0), convex (-) or concave (+)	
$c > 0$	distance between screw/nut and roller axis	-
$D_{zS}$	-	desired roller-screw backlash
$D_{zN}$	-	desired roller-nut backlash
$N_R \geq 3$	number of rollers	

Table 1.3: Simulation and design input parameters

Firstly, let us assume we wish to create a new PRS mechanism. In that case, we would select the *design* list of parameters. As it was summarized in table 1.1, all threaded surfaces (roller, screw, nut) can be entirely determined using their corresponding pitch radius, profile curvature radius, normal pressure angle, lead and number of thread starts. We will now explain how to find these five parameters for each component based on the input information provided in table 1.3.

For all three components, the normal pressure angle is considered to be constant and is directly given in table 1.3. For the screw, the lead and the number of starts are also given. We can thus use Eq. 1.2 and calculate the pitch  $p$  of the mechanism. For the roller, only the number of starts is given, but the lead can be determined using:

$$l_R = \begin{cases} \text{sgn}(l_S)pn_R & \text{standard PRS} \\ -\text{sgn}(l_S)pn_R & \text{inverted PRS} \end{cases} \quad (1.50)$$

where  $sgn$  is the sign function. Due to kinematic constraints detailed in section 2.2.2, the leads of the screw and the nut should be equal for both standard and inverted PRS, which means that:

$$l_N = l_S \Rightarrow n_N = n_S \quad (1.51)$$

The profile types (convex, straight, concave) and curvature radii for the three components are given in table 1.3 under the form of a signed curvature. Note that since the nut is an internal thread, we describe it using the geometry of the empty space contained within (complementary volume). This means that the sign convention is switched, since a convex nut contains a concave volume with a negative profile curvature.

The last parameters that we need for defining the three individual surfaces are the pitch radii, which have to be chosen such that the backlash conditions specified in table 1.3 are verified. This is because in practice, roller screws are often designed with a predefined backlash which is either nil or slightly negative, depending on preload. In all cases, however, we have at least a rough idea of the screw nominal diameter, which ultimately determines the size of the whole mechanism [1].

Assume we wish to design a standard PRS. In that case,  $r_S$  in table 1.3 would represent a rough approximation of the actual pitch radius of the screw we want to obtain. For this type of roller screw, we have to make sure that helix angles are matched between the nut and rollers<sup>1</sup>. Using equation 1.3 and previous considerations, this requirement can be rewritten as:

$$\tan \beta_R = \tan \beta_N \Rightarrow r_N = r_R \frac{n_N}{n_R} \Rightarrow r_R = \frac{r_S}{\frac{n_S}{n_R} - 2} \quad (1.52)$$

Hence, the pitch radii of the nut and roller are calculated using the approximate screw radius  $r_S$ . Note that since all radii are positive, the above formula requires that  $n_S > 2n_R$ . In other words, for single-start rollers in a standard PRS, the screw must have at least three starts.

Since the roller and nut surfaces are now entirely defined, it is possible to calculate the distance  $c$  between their axes in order to satisfy the  $D_{zN}$  condition. We achieve this using a dichotomy (bisection) algorithm centered on  $c = r_S + r_R$  with a  $\pm 2\%$  variation. At each iteration, a more precise value of  $c$  is given, the location of the  $J$  contact points is calculated and the resulting backlash is computed using Eq. 1.40. We tested the algorithm in several cases and noticed that for an absolute error below  $10^{-10}$ m on backlash, convergence is achieved in a negligible amount of time on a desktop computer.

Once  $c$  is known, the exact nominal radius for the screw can be calculated using a similar approach, i.e. dichotomy centered on  $r_S$  with a  $\pm 2\%$  variation. Every iteration tries a more precise value, calculates the location of the  $I$  contact points and compares the resulting backlash to the value specified in table 1.3. After convergence, the screw surface and also the mechanism as a whole are finally completely defined.

If we design an inverted PRS, on the other hand, we would like to determine the roller and screw surfaces first and then adjust the pitch radius of the nut. In this case,  $r_S$  represents the exact nominal radius of the screw and we want helix angles to be opposite for the screw and the rollers. Using a similar approach, we obtain:

$$\tan \beta_R = -\tan \beta_S \Rightarrow r_S = r_R \frac{n_S}{n_R} \Rightarrow r_R = r_S \frac{n_R}{n_S} \quad (1.53)$$

Note that equation 1.53 does not impose a condition on the number of starts like in the case of a standard PRS. This is one of the two main reasons inverted roller screws are still produced despite their higher manufacturing cost. The other reason is that it is easier to make the mechanism waterproof.

Since  $r_S$  and  $r_R$  are now defined, the distance  $c$  can be calculated so that the  $D_{zS}$  condition is respected. Next,  $r_N$  is computed such that  $D_{zN}$  is verified. In both cases, we use dichotomy algorithms very similar to the previous ones.

Let us now assume that the design phase is over and our mechanism has been machined. Due to manufacturing errors, wear, deformations, etc., geometrical measurements on the real

---

<sup>1</sup>As with equation 1.51, this is a well-known condition which can be deduced from permanent contact kinematics.

PRS will usually be slightly different from theoretical design values. Nevertheless, we might want to visualize the obtained geometry on a computer in order to define better tolerances and adjust the design. Hence, a set of parameters for completely defining the mechanism geometry based on a limited number of measurements could prove to be very useful. One possibility is to use the *simulation* list proposed in table 1.3.

As it can be seen, we assume that the geometry of the three individual surfaces is fully known. Nominal radii, profile curvatures, the distance  $c$  and the normal pressure angle are supposed to be measured accurately. The pitch  $p$  is considered to be exactly the same for all components, which means that leads and number of starts are linked by the same relationships as before. The only two unknowns are the backlash values, which can be calculated using equation 1.40.

In conclusion, both standard and inverted roller screws can be designed with predefined backlash, but in that case the distance  $c$  cannot be chosen. Moreover, it is necessary to adjust the nominal diameter of the screw (for standard PRS) or nut (for inverted PRS) if we want these backlash conditions to be satisfied. This requirement was also explained by Fedosovsky et al. [36]. The *simulation* list of parameters is somewhat complementary to the *design* list since it allows more adjustments, particularly in the distance  $c$  and the nominal radii.

## 1.4 Hertzian contact ellipse

The current work assumes that all solids are infinitely rigid such that the contact between two threaded components is always a set of single points. This approximation allows simpler dynamic models to be developed without using finite elements. However, single points lead to very crude approximations of the local sliding velocity field and friction forces. In chapter 3 (see Fig. 3.8), we show that this hypothesis alone can seriously alter the results in terms of power dissipation.

An interesting compromise can be reached by analyzing the different scales involved in the mechanism. We will prove in chapter 3 that single points can still be used accurately for the global stationary model, as long as local contact wrenches are calculated using the shape, size and orientation of the small areas which are expected to develop around the contact points.

The simplest way this information could be obtained is by applying the Hertzian theory of elasticity, well-summarized by Johnson [39]. As shown in Fig. 1.11, it involves approximating the two surfaces in contact with paraboloids around the contact point  $M$ . The contact must be non-conforming, i.e. surfaces 1 and 2 should both be convex, as drawn. If the surface normal vector at  $M$  is noted  $n$ , the resulting contact area is an ellipse located in the plane  $\pi$  perpendicular to  $n$ , which includes point  $M$ .

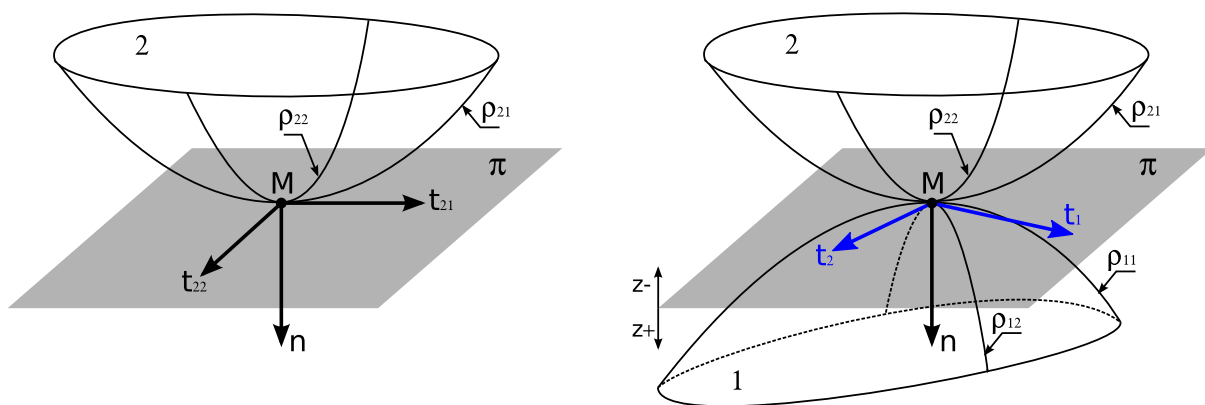


Figure 1.11: Non-conforming Hertzian contact at point  $M$

Depending on the normal load, surfaces 1 and 2 will approach for a small distance  $\delta$  when compared to the infinitely rigid case. However, the model developed in this work neglects the influence of local deformations such as these on the global geometry, such that the location of point  $M$  on the threads remains unchanged.

Secondly, the threaded profile shapes commonly used in roller screw design might lead to slightly conforming contacts. Although conforming contacts have been extensively studied before for cases such as journal or roller bearings, less and/or more difficult to use support is provided for saddle surfaces. Furthermore, the numerical results we obtain show that the differences to the non-conforming case are usually small. Therefore, we decided to privilege simplicity and generalize the Hertzian non-conforming theory in order to obtain coherent results for the slightly conforming case. These details are presented in the following section.

### 1.4.1 Orientation

First of all, let us focus on determining the orientation of the theoretical Hertzian contact ellipse centered at point  $M$ . As shown in Fig. 1.11 and explained by Johnson [39], we know that the ellipse is contained in the plane  $\pi$ , which can easily be determined when the surface normal vector  $\vec{n}$  and the location of point  $M$  are known. If  $(\vec{t}_1, \vec{t}_2)$  is a given basis of this plane, the two surfaces can locally be approximated to paraboloids such that:

$$z_1 = A_1 t_1^2 + B_1 t_2^2 + C_1 t_1 t_2 \quad (1.54)$$

$$z_2 = -(A_2 t_1^2 + B_2 t_2^2 + C_2 t_1 t_2) \quad (1.55)$$

where higher order terms in the Taylor expansion have been neglected. It is possible to choose the  $(\vec{t}_1, \vec{t}_2)$  basis such that  $C_1 = 0$  or  $C_2 = 0$ . Those particular directions are called principal directions of curvature for the corresponding surface. Let us note them  $(\vec{t}_{11}, \vec{t}_{12})$  for surface 1 and  $(\vec{t}_{21}, \vec{t}_{22})$  for surface 2. We can then write:

$$z_1 = \frac{\rho_{11}}{2} t_{11}^2 + \frac{\rho_{12}}{2} t_{12}^2 \quad (1.56)$$

$$z_2 = -\left(\frac{\rho_{21}}{2} t_{21}^2 + \frac{\rho_{22}}{2} t_{22}^2\right) \quad (1.57)$$

where  $(\rho_{11}, \rho_{12})$  and  $(\rho_{21}, \rho_{22})$  denote the principal curvatures of surfaces 1 and 2, respectively. As mentioned by Johnson [39], they represent the minimum and maximum values of all possible cross-section curvatures of the corresponding surface and are assimilated to the signed inverse of a radius. A way of calculating both the principal curvatures and the principal directions of curvature using differential geometry is detailed in appendix B.

In this thesis, we use a convention which states that for all convexities, the first curvature is always the minimum of the two in absolute value:

$$\begin{cases} \rho > 0 & \text{convex surface} \\ \rho = 0 & \text{plane surface} \\ \rho < 0 & \text{concave surface} \end{cases} \quad \begin{cases} |\rho_{11}| \leq |\rho_{12}| \\ |\rho_{21}| \leq |\rho_{22}| \end{cases} \quad (1.58)$$

On the other hand, the gap  $g$  between the two surfaces is defined as:

$$g = z_1 - z_2 = (A_1 + A_2)t_1^2 + (B_1 + B_2)t_2^2 + (C_1 + C_2)t_1 t_2 = At_1^2 + Bt_2^2 + Ct_1 t_2 \quad (1.59)$$

Like previously in the case of individual surfaces, it is possible to choose a particular basis  $(\vec{t}_1, \vec{t}_2)$  such that  $C = 0$ . The corresponding vectors are called principal *relative* directions of curvature. From now on,  $(\vec{t}_1, \vec{t}_2)$  will represent these particular directions, which are aligned with the major and minor ellipse diameters, respectively. Furthermore, since the ellipse is contained in the contact plane  $\pi$ , we can use the fact that:

$$\vec{t}_1 \times \vec{t}_2 = \vec{n} \quad \Rightarrow \quad \vec{t}_2 = \vec{n} \times \vec{t}_1 \quad (1.60)$$

which means that, in the end, the orientation of the Hertzian ellipse is entirely defined by the direction  $\vec{t}_1$ .

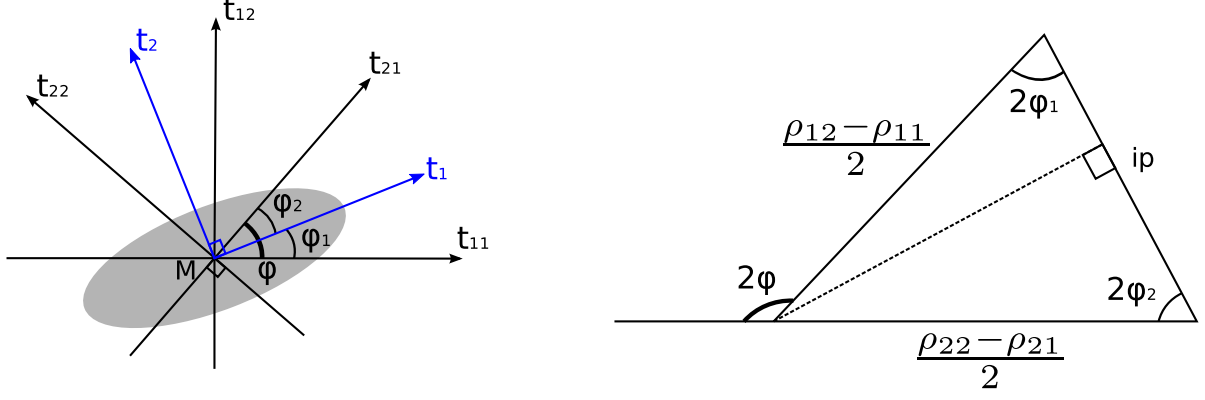


Figure 1.12: Principal directions of curvature and  $C = 0$  condition when  $\varphi \in (0, \frac{\pi}{2})$

As shown in Fig. 1.12, the first principal directions  $\vec{t}_{11}$  and  $\vec{t}_{21}$  for the two surfaces are generally not aligned and an angle  $\varphi$  exists between them, which we define as:

$$\varphi = \min \left( \cos^{-1}(\vec{t}_{11} \cdot \vec{t}_{21}), \pi - \cos^{-1}(\vec{t}_{11} \cdot \vec{t}_{21}) \right) \quad (1.61)$$

Taking the *min* in this expression ensures that  $\varphi \in [0, \frac{\pi}{2}]$  for all possible orientations of the  $\vec{t}_{11}$  and  $\vec{t}_{21}$  vectors.

According to our convention, the first principal direction for each surface corresponds to the minimum curvature in absolute value. If the first surface was a cylinder, for example,  $\vec{t}_{11}$  would be aligned with the cylinder's axis, pointing towards the direction of minimal curvature in absolute value, which in this case would be 0 (infinite radius). The same would apply to the second surface. Therefore, we expect the major diameter of the contact ellipse to be situated somewhere between  $\vec{t}_{11}$  and  $\vec{t}_{21}$ , as shown in Fig. 1.12. This means that we can define two non-oriented angles  $\varphi_1, \varphi_2 \in [0, \pi/2]$  such that:

$$\varphi = \varphi_1 + \varphi_2 \quad (1.62)$$

The direction  $\vec{t}_1$  can then be determined if  $\varphi_1$  is known.

For calculating  $\varphi_1$ , we turned once again to the work of Johnson [39]. He realized that the condition  $C = 0$  in Eq. 1.59 is equivalent to the existence of the triangle drawn in Fig. 1.12. The length  $ip$  can then be calculated with the cosine theorem:

$$ip^2 = \frac{(\rho_{12} - \rho_{11})^2}{4} + \frac{(\rho_{22} - \rho_{21})^2}{4} + \frac{(\rho_{12} - \rho_{11})(\rho_{22} - \rho_{21})}{2} \cos 2\varphi \quad (1.63)$$

The sine theorem, on the other hand, gives:

$$\frac{\rho_{22} - \rho_{21}}{2 \sin 2\varphi_1} = \frac{ip}{\sin 2\varphi} \quad (1.64)$$

which allows to calculate the angle  $\varphi_1$ :

$$\varphi_1 = \frac{1}{2} \sin^{-1} \left( \frac{(\rho_{22} - \rho_{21}) \sin 2\varphi}{\sqrt{(\rho_{12} - \rho_{11})^2 + (\rho_{22} - \rho_{21})^2 + 2(\rho_{12} - \rho_{11})(\rho_{22} - \rho_{21}) \cos 2\varphi}} \right) \quad (1.65)$$

In his work, Johnson [39] considers two non-conforming surfaces in contact. This is not necessarily the case for planetary roller screws, where conforming contacts are possible. However, we can assume as a first approximation that surfaces can still be locally approximated to paraboloids such that higher order terms in Eqs. 1.54-1.55 are negligible, even if one of the curvatures is slightly negative. The calculations we performed showed that contacts in roller

screws are still far from the case of a shaft in a bore, for example, where the conformity becomes significant.

In order to detect whether the contact is conforming or not, it is possible to introduce a variable  $s$  such that:

$$s = (\rho_{22} - \rho_{21})(\rho_{12} - \rho_{11}) \quad (1.66)$$

Then whenever  $s < 0$  the contact will be conforming, since the first curvature is always the minimum in absolute value. Depending on the values of  $s$ ,  $\varphi$  and the curvatures, Eq. 1.65 is not always valid and some particular cases have to be considered as well. The final solution for angle  $\varphi_1$  is given in table 1.4, with explanations provided below. Once  $\varphi_1$  is known, the orientation of the Hertzian contact ellipse can be calculated as:

$$\vec{t}_1 = \cos \varphi_1 (\vec{t}_{11}) + \sin \varphi_1 (\vec{n} \times \vec{t}_{11}) \cdot \text{sgn} \left( (\vec{t}_{11} \times \vec{t}_{21}) \cdot \vec{n} \right) \cdot \text{sgn} (\vec{t}_{11} \cdot \vec{t}_{21}) \quad (1.67)$$

where the  $\text{sgn}$  functions are either -1,0 or 1. They were introduced to make sure the result is robust and works well for all possible directions of curvature.

Condition		Solution		
$s = 0$	$\rho_{22} = \rho_{21}$ and $\rho_{12} \neq \rho_{11}$	$\varphi_1 = 0$		
	$\rho_{22} \neq \rho_{21}$ and $\rho_{12} = \rho_{11}$	$\varphi_1 = \varphi$		
	$\rho_{22} = \rho_{21}$ and $\rho_{12} = \rho_{11}$	$\varphi_1 \in \mathbb{R}$		
$s \neq 0$	$\varphi = 0$	$\varphi_1 = 0$		
		$\rho_{12} > \rho_{22}$	$\varphi_1 = 0$	
		$\rho_{12} < \rho_{22}$	$\varphi_1 = \varphi$	
	$\varphi = \frac{\pi}{2}$	$\rho_{12} = \rho_{22}$	$\rho_{11} < \rho_{21}$	$\varphi_1 = 0$
			$\rho_{11} > \rho_{21}$	$\varphi_1 = \varphi$
			$\rho_{11} = \rho_{21}$	$\varphi_1 \in \mathbb{R}$
	$\varphi \in \left(0, \frac{\pi}{2}\right)$	$\varphi_1 = \frac{1}{2} \sin^{-1} \left( \frac{ \rho_{22} - \rho_{21}  \sin 2\varphi}{\sqrt{(\rho_{12} - \rho_{11})^2 + (\rho_{22} - \rho_{21})^2 + 2 (\rho_{12} - \rho_{11})(\rho_{22} - \rho_{21})  \cos 2\varphi}} \right)$		

Table 1.4: General solution for angle  $\varphi_1$  and the Hertzian ellipse orientation

If  $s$  is nil, it means that at least one of the two surfaces is either a plane or a sphere, such that its curvatures are locally equal at the contact point. If this is true for both surfaces, the contact area will be planar or circular and  $\vec{t}_1$  could point in any direction ( $\varphi_1 \in \mathbb{R}$ ). On the other hand, if only one surface satisfies the condition, then the ellipse will align itself with the first (minimal) curvature of the other surface, such that  $\varphi_1$  is either 0 or  $\varphi$ .

In the general case, when  $s \neq 0$  and  $\varphi \neq \pi/2$ , we have to calculate  $\varphi_1$  using Eq. 1.65. A more robust formula can be obtained by adding absolute values, as shown in table 1.4. This ensures that the contact ellipse is oriented as expected, even if the surfaces are slightly conforming.

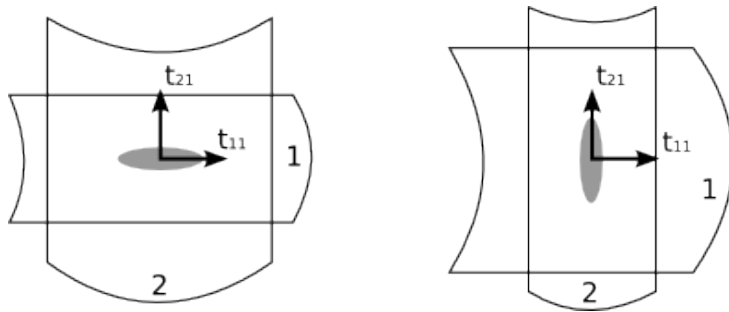


Figure 1.13: Example of first principal directions of curvature when  $\varphi = \frac{\pi}{2}$

If  $\varphi = \pi/2$ , the first principal directions of curvature are perpendicular and a separate analysis is required. Let's consider the example of two cylinders of different radii, as shown in Fig. 1.13. In absolute value, the minimal curvatures are nil for both surfaces due to their shape.

We can see in Fig. 1.13 that the ellipse aligns itself with the surface that has the maximum curvature, such that:

$$\vec{t}_1 = \begin{cases} \vec{t}_{11} & \text{if } \rho_{12} > \rho_{22} \\ \vec{t}_{21} & \text{if } \rho_{12} < \rho_{22} \end{cases} \quad (1.68)$$

However, the result is more complicated if the two surfaces have the same maximum curvature, i.e.  $\rho_{12} = \rho_{22}$ . That case can be imagined as the contact between two identical and perpendicular tori. The contact area will be a circle and  $\vec{t}_1$  could take any value in the plane  $\pi$  ( $\varphi_1 \in \mathbb{R}$ ). But if we cut one of the tori and attempt to straighten it as a tube, the circle becomes an ellipse along the tube. This direction corresponds to the surface with the minimal curvature, such that:

$$\text{if } \rho_{12} = \rho_{22}, \quad \vec{t}_1 = \begin{cases} \vec{t}_{11} & \text{if } \rho_{11} < \rho_{21} \\ \vec{t}_{21} & \text{if } \rho_{11} > \rho_{21} \\ \in \pi & \text{if } \rho_{11} = \rho_{21} \end{cases} \quad (1.69)$$

All in all, the solution proposed in table 1.4 allows to determine the orientation of the Hertzian contact ellipse between *any* two surfaces (including slightly conforming), provided that we can locally approximate them to paraboloids. Our approach ensures that  $\vec{t}_1$  and  $\vec{t}_2$  are aligned with the major and minor diameters, respectively, for all possible curvatures and orientations of the principal directions for the two surfaces.

## 1.4.2 Shape

The shape of the Hertzian contact ellipse can be characterized by a unique parameter  $k$  called ellipticity ratio. If  $a$  and  $b$  are the major and minor half-diameters of the ellipse, respectively,  $k$  is defined as:

$$k = \frac{a}{b} \quad (1.70)$$

which means that  $k \geq 1$ .

In order to calculate  $k$ , we can start by replacing  $z_1$  and  $z_2$  from Eqs. 1.56-1.57 in the gap Eq. 1.59. We would then obtain the values of  $A$  and  $B$ :

$$2A = \rho_{11} \cos^2 \varphi_1 + \rho_{12} \sin^2 \varphi_1 + \rho_{21} \cos^2(\varphi - \varphi_1) + \rho_{22} \sin^2(\varphi - \varphi_1) \quad (1.71)$$

$$2B = \rho_{11} \sin^2 \varphi_1 + \rho_{12} \cos^2 \varphi_1 + \rho_{21} \sin^2(\varphi - \varphi_1) + \rho_{22} \cos^2(\varphi - \varphi_1) \quad (1.72)$$

Following the example for individual surfaces, it is possible to define two *relative* principal curvatures  $\rho_1$  and  $\rho_2$ , corresponding to the  $\vec{t}_1$  and  $\vec{t}_2$  directions, respectively, such that:

$$\begin{cases} \rho_1 & = 2A \\ \rho_2 & = 2B \end{cases} \quad (1.73)$$

Since  $\vec{t}_1$  is calculated as a combination of directions of minimal curvature in absolute value, we would expect it to transmit the property: in practice, we should always obtain  $|\rho_1| \leq |\rho_2|$ . However, this is not always the case and sometimes the pairs  $(\rho_1, \vec{t}_1)$  and  $(\rho_2, \vec{t}_2)$  have to be interchanged in the algorithm to ensure that the property is verified.

If the two relative curvatures  $\rho_1$  and  $\rho_2$  have opposite signs, it usually means that the contact area does not exist. Also, when one of the curvatures is nil, we cannot calculate the shape of the ellipse because the contact is either a stripe or a plane. Therefore, only if the condition  $\rho_1 \rho_2 > 0$  is satisfied, we can determine the ratio  $q$  defined by:

$$q = \frac{\rho_2}{\rho_1} \quad (1.74)$$

The link between  $q$  and  $k$  has been studied by many authors, some of which are mentioned in table 1.5.

Hamrock & Dowson [40]	$k = 1.03q^{0.64}$
Hamrock & Brewe [41]	$k = q^{2/\pi}$
Johnson [39]	$k = q^{2/3}$
Antoine et al. [42]	$k = q^{\gamma(q)}$

Table 1.5: Expression of  $k$  as a function of  $q$  in current literature, in chronological order

Antoine [42] tested his model for a wide range of  $q$  ratios to obtain:

$$\gamma(q) = \frac{2}{3} \left( \frac{1 + \mu_1 X^2 + \mu_2 X^4 + \mu_3 X^6 + \mu_4 X^8}{1 + \mu_5 X^2 + \mu_6 X^4 + \mu_7 X^6 + \mu_8 X^8} \right); \quad X = \log_{10} q \quad (1.75)$$

$$\begin{aligned} \mu_1 &= 0.40227436 & \mu_2 &= 3.7491752e - 2 \\ \mu_3 &= 7.4855761e - 4 & \mu_4 &= 2.1667028e - 6 \\ \mu_5 &= 0.42678878 & \mu_6 &= 4.2605401e - 2 \\ \mu_7 &= 9.0786922e - 4 & \mu_8 &= 2.7868927e - 6 \end{aligned} \quad (1.76)$$

and we found that his results are relatively close to the expression  $k = q^{2/\pi}$  provided in [41], which is the one we preferred in the current work.

In conclusion, it is possible to find the shape of the contact ellipse by using the ellipticity ratio  $k$ , which can be calculated as a function of surface curvatures and the ellipse orientation. By adding information about the normal load and materials, the actual size of the ellipse can also be determined.

### 1.4.3 Size

From Eqs. 1.71-1.72, the curvature sum  $S_\rho$  can be obtained as:

$$S_\rho = 2(A + B) = \rho_{11} + \rho_{12} + \rho_{21} + \rho_{22} = \rho_1 + \rho_2 \quad (1.77)$$

Let us now assume that the two solids in Fig. 1.11 are made of homogeneous and isotropic materials. The relative modulus of elasticity  $E'$  is defined as:

$$\frac{2}{E'} = \frac{1 - \nu_1^2}{E_1} + \frac{1 - \nu_2^2}{E_2} \quad (1.78)$$

where  $\nu_1, \nu_2$  and  $E_1, E_2$  are the Poisson ratios and Young's moduli for the two bodies, respectively. In the current work, we will typically consider steel materials, such that  $\nu_1 = \nu_2 = 0.3$  and  $E_1 = E_2 = 210$  GPa, which leads to:

$$E' = 230.77 \text{ GPa} \quad (1.79)$$

When  $E'$  and the contact normal load  $N$  are known, half-diameters  $a$  and  $b$  and the surface approach  $\delta$  are given by Harris and Kotzalas [43]:

$$a = \left( \frac{6k^2 \varepsilon_k N}{\pi S_\rho E'} \right)^{1/3} \quad b = \frac{a}{k} = \left( \frac{6\varepsilon_k N}{\pi k S_\rho E'} \right)^{1/3} \quad (1.80)$$

$$\delta = \mathcal{F}_k \left( \frac{S_\rho}{2\varepsilon_k} \left( \frac{3N}{\pi k E'} \right)^2 \right)^{1/3} \quad (1.81)$$

In the above formulas,  $\mathcal{F}_k$  and  $\varepsilon_k$  denote complete elliptic integrals of the first and second kind, respectively. For the purposes of the current work, we have computed them numerically in the Matlab environment using:

$$[\mathcal{F}_k, \varepsilon_k] = \text{ellipke} \left( 1 - \frac{1}{k^2} \right) \quad (1.82)$$

where the value  $1 - 1/k^2$  has been deduced in order to match the programmed formulas with reference [43].

Finally, once the dimensions of the contact ellipse are known, the maximum Hertzian and average pressures can also be calculated:

$$P_h = \frac{3N}{2\pi ab} \quad P_m = \frac{N}{\pi ab} \quad (1.83)$$

## 1.5 Application examples

### 1.5.1 Example 1: Simulation of a standard PRS

In this first example, we show how the method developed in this chapter can be used to simulate a particular standard roller screw. We compare our results for the geometry of individual components, the assembly and the location of the contact points to those obtained by Jones and Velinsky [33], as summarized in table 1.6. Reference [33] was chosen because it provides direct numerical values for this specific roller screw. Moreover, it was also used by Fu et al. [35] to validate a contact analysis method where backlash is a 3-dimensional vector. The results obtained in [35] show that the two papers lead to almost identical solutions. However, reference [35] mainly presents figures and the contact location unknowns are only expressed as a system of non-linear equations, without specific numbers. This is why we were unable to reliably compare our results with [35], even though the study is more recent and general.

Variable	[Unit] []	Example 1 Current work	Example 1 Jones and Velinsky [33]	Example 2 Current work	Example 3 Current work	Example 4 Current work
$r_S$	[mm]	15	15	15	9.75	9.8787
$l_S$	[mm]	10	10	10	10	9
$n_S$	[]	5	5	2	5	6
$\beta_S$	[deg]	6.0566	6.06	6.0566	9.2710	8.2503
$\pm 1/r_{BS}$	[1/mm]	0	0	0	0	0
$r_{minS}$	[mm]	14.5028	-	13.7570	9.5527	9.4665
$r_{maxS}$	[mm]	15.4972	-	16.2430	9.9473	10.2909
$r_R$	[mm]	5	5	7.5	3.25	10
$l_R$	[mm]	2	2	-5	2	3
$n_R$	[]	1	1	1	1	2
$\beta_R$	[deg]	3.6426	3.64	-6.0566	5.5938	2.7336
$\pm 1/r_{BR}$	[1/mm]	+1/7.07	+1/7.07	+0.0471	+0.2857	+0.0669
$r_{minR}$	[mm]	4.4453	4.5	6.1443	3.0036	9.5676
$r_{maxR}$	[mm]	5.4535	5.5	8.6477	3.4070	10.4010
$r_N$	[mm]	25	25	30.1265	16.25	30
$l_N$	[mm]	10	10	10	10	9
$n_N$	[]	5	5	2	5	6
$\beta_N$	[deg]	3.6426	3.64	3.0241	5.5938	2.7336
$\pm 1/r_{BN}$	[1/mm]	0	0	0	0	0
$r_{minN}$	[mm]	24.5010	-	28.8783	16.0511	29.5840
$r_{maxN}$	[mm]	25.4990	-	31.3748	16.4489	30.4160
$p$	[mm]	2	2	5	2	1.5
$\alpha_n$	[deg]	45	45	45	68.21	42
$c$	[mm]	20	20	22.5	13	19.9945
$D_{zS}$	[mm]	-0.1071	-	0	-0.0656	+0.01
$D_{zN}$	[mm]	0	-	0	0	+0.01
$r_{IS}$	[mm]	15.0351	15.005	15	9.7586	9.9914
$r_{IR}$	[mm]	5.0177	5.05	7.5	3.2543	10.1112
$r_{JR}$	[mm]	5	5.03	7.4360	3.25	10
$r_{JN}$	[mm]	25	25.0301	29.8095	16.25	29.9945
$\theta_{IS}$	[deg]	2.3994	2.42	0	-1.4717	-5.9823
$\theta_{IR}$	[deg]	172.7935	172.78	-180	-175.5829	-174.0889
$\theta_{JR}$	[deg]	0	0	12.1996	0	8.4e-4
$\theta_{JN}$	[deg]	0	0	3.0217	0	2.8e-4

Table 1.6: Examples of PRS geometry results in the  $I_1J_2$  configuration

We consider the same geometry for individual components as reference [33]. In terms of the location of the contact points  $I$  and  $J$  we obtain close, but not identical results. Due to the equality of helix angles between the roller and the nut and the value imposed for the distance  $c$ , the position of points  $J$  is not shifted and in both cases it is located in the  $zx$  plane, such that  $\theta_{JR} = \theta_{JN} = 0$ .

As opposed to the referenced paper, we offer the possibility to calculate axial backlash for the screw-roller contact ( $D_{zS}$ ) and the nut-roller contact ( $D_{zN}$ ). In this particular example, the roller fits perfectly inside the nut ( $D_{zN} = 0$ ), while the screw/roller threads appear to interpenetrate for a small distance ( $D_{zS} < 0$ ). This does not necessarily mean that the mechanism fails, since we deal with infinitely rigid solids and single point contacts.

Finally, we also define the minimal and maximal profile radii for each component, while the cited article only provides these results for the roller. The pressure angle is taken to be constant and equal to 45 degrees, although Jones and Velinsky calculate a different value for the roller at the contact with the screw (45.2 degrees).

### 1.5.2 Example 2: Design of an inverted PRS

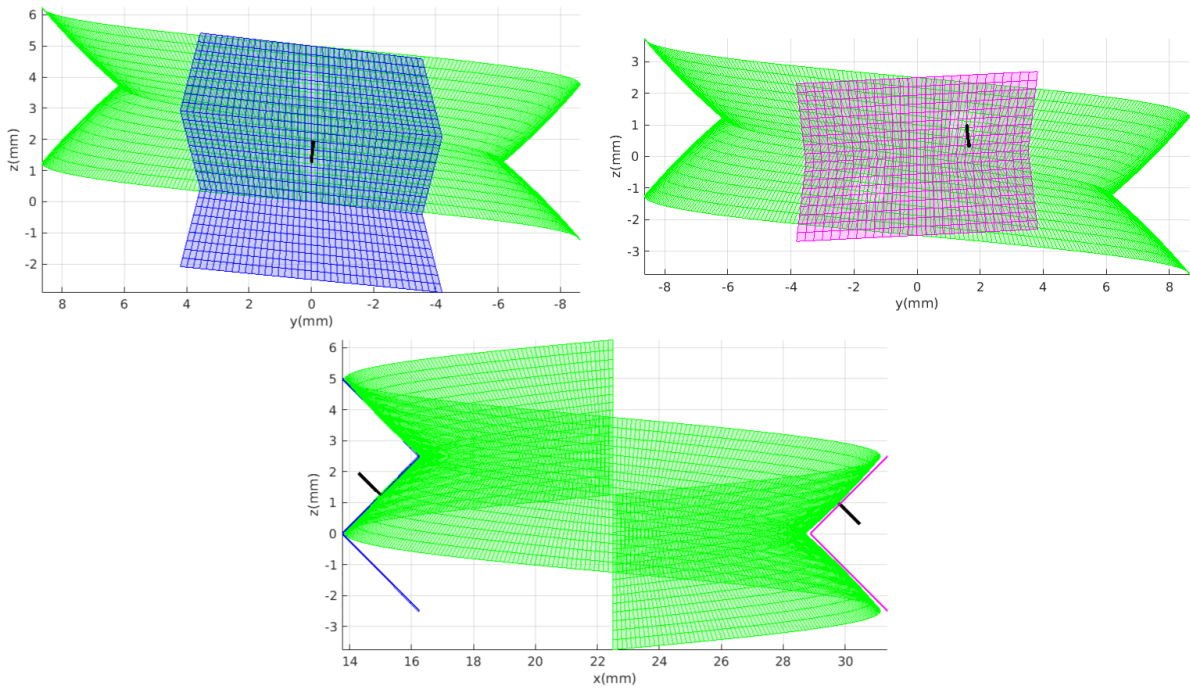


Figure 1.14: Threaded surfaces for an inverted PRS. Screw (blue), Roller (green) and Nut (magenta) with normal vectors at the contact points.  $I_1J_2$  configuration.

In this second example, we use the developed method to design an inverted PRS with the dimensions shown in table 1.6. As opposed to the previous example, where the *simulation* list of parameters was used, this time we employ the *design* list, as detailed in table 1.3. Only those inputs need to be specified; the program calculates the rest of the geometrical unknowns.

We want to design a mechanism with no backlash, therefore the imposed values for  $D_{zS}$  and  $D_{zN}$  are nil. The distance  $c$  and the nut nominal diameter  $r_N$  are adjusted in order to satisfy these conditions. We can see that the  $I$  contact points between the screw and the roller are situated in the  $zx$  plane, at the intersection of the two nominal radii. This is expected for this inverted PRS, due to the fact that  $\beta_S = -\beta_R$  and  $D_{zS} = 0$ .

Regarding the location of the  $J$  contacts (roller-nut), we decided to compare our results with those obtained by Fedosovsky et al. [36], who used a different numerical method involving a grid on the same global geometry. Since the referenced paper expresses results in terms of  $(x, y)$

coordinates from the center of the screw, we had to perform a small calculation:

$$\begin{cases} x_J = r_{JN} \cos \theta_{JN} = r_{JR} \cos \theta_{JR} + c \\ y_J = r_{JN} \sin \theta_{JN} = r_{JR} \sin \theta_{JR} \end{cases} \quad (1.84)$$

in order to obtain the results summarized in table 1.7.

	$x_J$	$y_J$	$2r_N$	$c$
Current memoir	29.768	1.571	60.25	22.5
Fedosovsky et al. [36]	29.899	1.579	60.25	-

Table 1.7: Global location of  $J$  for an inverted PRS

It can be seen that the two methods yield close results in terms of the location of point  $J$ . There seems to be a noticeable difference for the  $x_J$  coordinate, perhaps due to a difference in  $c$  (interaxle distance in [36]) between the two papers. Although reference [36] does not provide the value of  $c$  directly, it appears from the figures in the article that it is exactly equal to the sum of the screw and roller nominal radii, which is also the case in the current work. Furthermore, the adjusted pitch diameter of the nut is the same, validating the fact that during the design process, at least one component in the roller screw needs to be rectified in order to guarantee backlash.

The equations presented in the current work can also be used to write a program for drawing the threads and therefore verify results visually. Figure 1.14, in this example, shows small parts of the computed screw, roller and nut surfaces, as well as contact normal vectors drawn at the location of the contact points.

### 1.5.3 Example 3: Influence of pitch

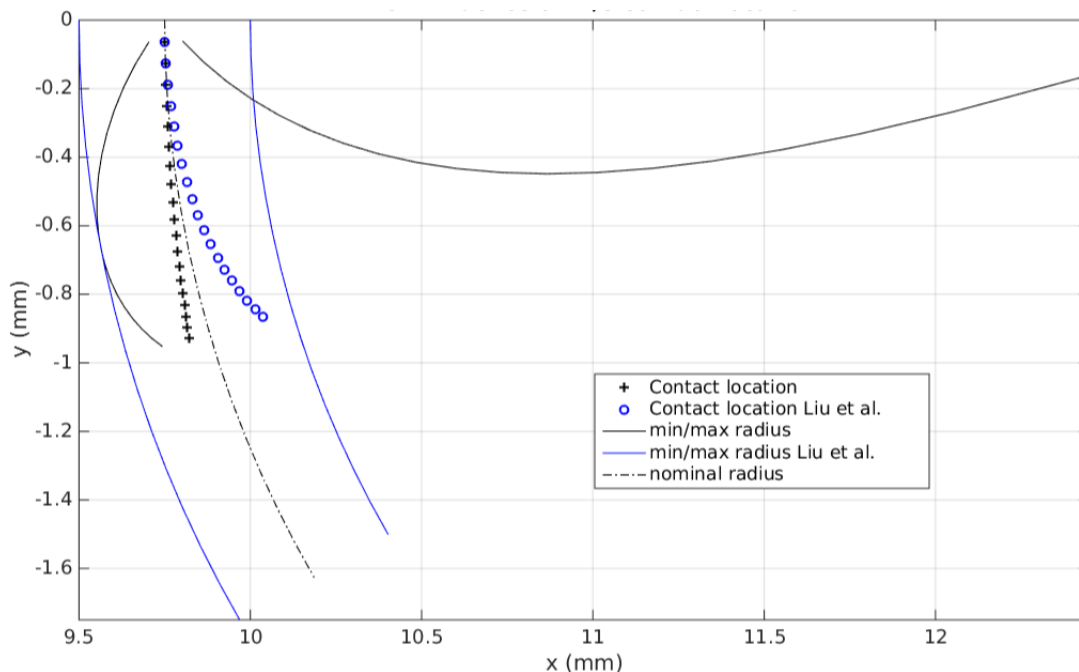


Figure 1.15: Contact point  $I$  location on the roller for different pitch values  $\in [0.5; 9.5]$ mm (constant increase of 0.5mm). Roller center is at  $x = 13$ mm,  $y = 0$ mm. Comparison with [34].

This third example aims to investigate the influence of pitch on the location of the  $I$  contact points between the screw and the roller. In order to allow the comparison of our results with current literature, we used the same surface geometry as reference [34]. The dimensions in table 1.6 were obtained by simulating a standard roller screw with the nominal radii values specified in [34], along with a few other adjustments which are detailed below.

The convex profiles defined in this thesis are circular in the normal  $z'x$  plane, but when projected in the axial  $zx$  plane they appear elliptical. Hence, we can apply the theory proposed in [34] with the following parameters:

$$r_a = r_{BR} = 3.5\text{mm} \quad (1.85)$$

$$r_b = \frac{r_{BR}}{\cos \beta_R} \quad (1.86)$$

where  $r_a$  and  $r_b$  are the two radii for the elliptical profile. As for the pressure angle, we used:

$$r_{BR} = \frac{r_R}{\sin \alpha_n} \Rightarrow \alpha_n = \sin^{-1} \frac{r_R}{r_{BR}} = 68.21^\circ \quad (1.87)$$

For values of  $p$  between 0.5 and 9.5mm, the locations of contact point  $I$  on the roller computed according to this work are shown in black in Fig. 1.15. We can see that  $I$  is situated on the nominal diameter for small pitches, then moves towards the outer radius as  $p$  increases. This is the expected behavior and was mentioned by other authors as well [35]. The explanation is that since the backlash is nonpositive, screw and roller helix angles will increase with the pitch, leading to a more pronounced intersection that pushes the contact point towards the edge of the thread. Reference [34] claims to obtain a similar tendency, although we were unable to retrace their results based on the provided formulas. Furthermore, if the measurement units in Fig. 10 in the cited reference are to be trusted, it would mean that for a pitch value of 10mm, the contact angle is around  $60^\circ$ , which does not make sense.

Therefore, in Fig. 1.15, only the contact point radius  $r_{IR}$  deduced in [34] by an analytical method is used to trace the blue dots; the contact angle is calculated by us and is taken to be the same as for the corresponding black dots. Nevertheless, the mentioned reference fails to display the expected behavior, since the contact radius moves towards the inner radius when  $p$  increases.

Another difference can be observed for the minimum and maximum profile radii, which vary with pitch according to our model, while the authors of article [34] assume them to be constant and equal to 3mm and 3.5mm, respectively. In our view, this variation is required for obtaining *top* and *bottom* surfaces that match perfectly at  $r_{min}$  and  $r_{max}$  for all pitch values, as shown in Fig. 1.14. Note that throughout this work, we considered the entire triangular profile with sharp edges. In practice, edges are usually truncated depending on the machine tool; therefore, the measured outer/inner diameters might *appear* to be independent of pitch.

#### 1.5.4 Example 4: Influence of profile curvatures

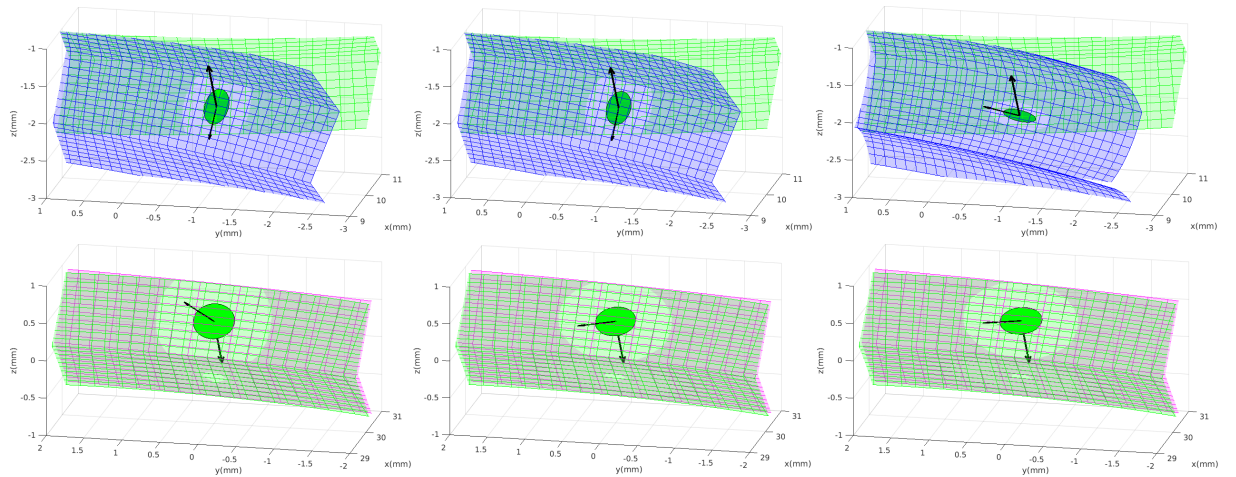


Figure 1.16: Hertzian ellipse for  $I$  and  $J$ . Screw in blue, roller in green and nut in magenta.  $I_1J_2$  configuration. Normal contact vector at the  $I$  or  $J$  centers and principal *relative* direction of curvature  $t_1$ . Normal load  $N_I \approx N_J \in 121 \pm 1\text{N}$ . Hertzian pressures  $P_{hI} = 1.4\text{ GPa}$ ,  $P_{hJ} = 1\text{ GPa}$ .

In this final example, we analyze the influence of profile curvatures on the shape and orientation of the Hertzian contact ellipse at  $I$  and  $J$ . In order to prove the capabilities of the geometrical model presented in this memoir, we chose more exotic parameters in comparison with previous examples. As detailed in table 1.6, the reference case consists in designing a standard PRS with a positive, imposed backlash of 0.02 mm. The desired pressure angle is  $42^\circ$  and rollers have 2 starts instead of 1.

Table 1.6 presents the contact location results obtained for straight screw and nut profiles, and a convex roller profile such that  $r_{BR} = r_R / \sin 42^\circ$ , according to Eq. 1.5. We can see that the values for  $\theta_{JR}$  and  $\theta_{JN}$  are very small, but not zero. This is due to the imposed value for  $D_{zN}$ , which modifies the distance  $c$  slightly, such that the contact point  $J$  is no longer on the nut nominal diameter. The value deduced for  $c$ , as well as the  $D_{zS}$  axial play, impose a rectification on the nominal screw diameter  $r_S$ , which should otherwise have been 10 mm.

The computed contact areas for  $I$  and  $J$  are shown in the center of Fig. 1.16. In both cases, the ellipticity ratio  $k$  is less than 2. The figure also shows the  $\vec{t}_1$  direction, aligned with the major diameter of the ellipse. The roller-nut ellipse appears to be more or less along the helical thread direction, while the roller-screw ellipse is close to being perpendicular. Numerical results issued from the model can be verified visually by analyzing the way Matlab manipulates light through semi-transparent meshes. Areas which are very close to one another are automatically displayed in a lighter shade than the basic color, as can be seen in Figs. 1.14-1.16. However, this trick can only be used to verify shape and orientation results: the actual size of the contact area depends on the normal load and can only be calculated.

curvature	left	center	right
$\pm 1/r_{BS}$	- 0.007	0	+0.6
$\pm 1/r_{BR}$	+0.0669	+0.0669	+0.0669
$\pm 1/r_{BN}$	+0.03	0	- 0.01

Table 1.8: Profile curvature values used in Fig. 1.16

In order to study the influence of profile curvatures, we have changed the  $r_{BS}$  and  $r_{BN}$  values according to table 1.8. The left side of Fig. 1.16 corresponds to a concave screw and nut, while the right side was drawn for convex surfaces. Curvature values in table 1.8 were not randomly chosen: they are a rough approximation of the minimum and maximum values allowed for this particular geometry, such that the contact location algorithm described in appendix A works without returning any errors. Curvatures outside this interval lead to contacts placed on impossible locations or on the edges of the threads.

Results show that there is a larger range in the choice of the screw profile curvature, when compared to the nut. Increasing the screw convexity leads to a thinner Hertzian ellipse, which eventually aligns itself with the helix direction. The fact that we can rotate the roller-screw contact ellipse by roughly  $90^\circ$  becomes important when considering lubrication, since the sliding velocity vector will generally not be aligned with the major diameter of the ellipse.

## 1.6 Conclusion

This chapter provides a detailed method for analyzing the thread geometry of both standard and inverted roller screws. After a careful analysis of current literature, three different profile shapes are defined, which can effectively model common surfaces used in designing the mechanism. The corresponding surface equations are deduced, as well as a general formula for the external unit normal vector.

Roller, screw and nut surfaces are then assembled into a model which computes the location of contact points between threads by taking axial backlash into consideration. The model proposes two ways of completely defining the roller screw geometry that minimize the number of input parameters. The first possibility is intended for designing new mechanisms based on the screw diameter and backlash, while the second is useful for simulating measured or imposed

geometry. In contrast with existing literature, the choice of the most appropriate approach for an application is left to the user in order to avoid over-defined or under-defined geometries and confusion.

Differential geometry equations are then applied for calculating principal curvatures and directions of curvature at any point on the studied surfaces. In terms of curvature values, our results are found to be in agreement with literature. However, the directions of curvature we obtain are different and possibly less intuitive. Nevertheless, we believe that the results presented here are more systematic and general, since they come from the direct application of the theory, instead of pre-made assumptions.

We were then able to model the shape, size and orientation of the contact areas between the threaded surfaces using the Hertzian theory. The theory was extended for slightly conforming contacts, which can be encountered in common roller screw designs. This required an in-depth analysis of the involved equations, which were made more robust to ensure that all possible cases were covered. The influence of local deformations on the global geometry and location of the contact points was neglected.

Both the design and simulation sets of input parameters were employed in the examples which compare the results of our model with those of other authors. We were able to confirm the fact that at least one component in the mechanism needs to be rectified in order to guarantee backlash and that the roller/screw contact point in standard PRS moves towards the outer radius as the pitch increases. We have also studied the influence of profile curvatures on the shape and orientation of contact areas, and it was shown that the Hertzian ellipse can turn up to  $90^\circ$  as the screw profile becomes more bumped or convex. This has an important effect on lubrication conditions.

## Chapter 2

# Stationary regime kinematics

### 2.1 Introduction

In this chapter, we investigate roller screw kinematics in order to identify the major friction phenomena which dissipate power in the threaded contacts. The subject has received little attention in current literature, since only the global movement of different components is usually studied. This work also puts significant attention into the local sliding speed to show the difference between roller-screw and roller-nut contacts. Some of the results presented here have already been published by the authors in another paper [14].

First of all, the global mechanism kinematics is analyzed in the stationary regime. The model proposed here is centered on the amount of slip in the PRS, which has two components: axial slip, inherent to the translation of the nut with respect to the screw, and circumferential slip, which can exist because the PRS is not a planetary gear train. Both of these components depend on geometry, lubrication conditions, loading, etc. Circumferential slip, however, is particularly difficult to control and usually has to be determined.

One of the earliest references in current literature [2] attempted to tackle the problem by dividing the screw rotation angle in two parts: one without slip and the other characterized by pure sliding. The relative velocity at contact points is then calculated. This research was followed by a more elaborate dynamic analysis [44] which showed that the planet carrier turns slightly slower when friction forces are considered, with respect to the purely kinematic, no-slip behavior.

Other authors quantify circumferential slip through numerical simulations [18] or complex dynamic models [28]. Experiments have been performed in some cases [19, 38], but they focus on the axial positioning error. In any case, these solutions are not very flexible since they can only be applied to some particular PRS.

The analytical kinematic model developed in the current chapter was specifically designed to work for both standard and inverted roller screws. We study circumferential slip through a non-dimensional variable called the slip ratio, which is left undetermined. Instead of predicting the steady-state value numerically (this is done in chapter 3), we calculate the theoretical ideal and then measure the ratio through experiments.

The global model is then taken a step further and we also determine the sliding velocity field at all points within the contact areas. Results are used to deduce local friction coefficients which are consistent with classic grease lubrication tests. These coefficients have a direct impact on the power dissipated within the mechanism.

### 2.2 Global slip model

From a kinematic point of view, roller screws work similarly to planetary gear trains, with the addition of axial movement and some inherent slip. Here, we study the stationary regime of an idealized mechanism, i.e. all speeds are assumed constant and there is no geometrical error due to machining, wear or deformation that would prevent roller-nut or roller-screw thread contacts

from being identical between themselves. Rollers are assumed to be identical, such that their rotation axis and geometrical axis coincide at all times.

In these conditions, we can draw the kinematic diagram of a roller screw as shown in Fig. 2.1. Let us assume that  $(O, x, y, z)$  is a Galilean frame fixed to the test bench on which the mechanism operates. The screw  $S$  pivots with respect to this frame, such that only a rotation around  $z$  is permitted. The nut  $N$ , on the other hand, can only translate in this direction. Although in reality there are actually two planet carriers, it is assumed that the rollers pivot in between with axes parallel to the  $z$  direction, such that the two sides of the carrier  $P$  exhibit an identical movement at all times. Furthermore, this movement is assumed to be a pure rotation around the same  $z$  axis as the screw and nut. Note that the figure was drawn for a standard PRS and therefore there is no contact between the carrier and the screw. For an inverted PRS,  $P$  would pivot around  $S$  instead of  $N$ .

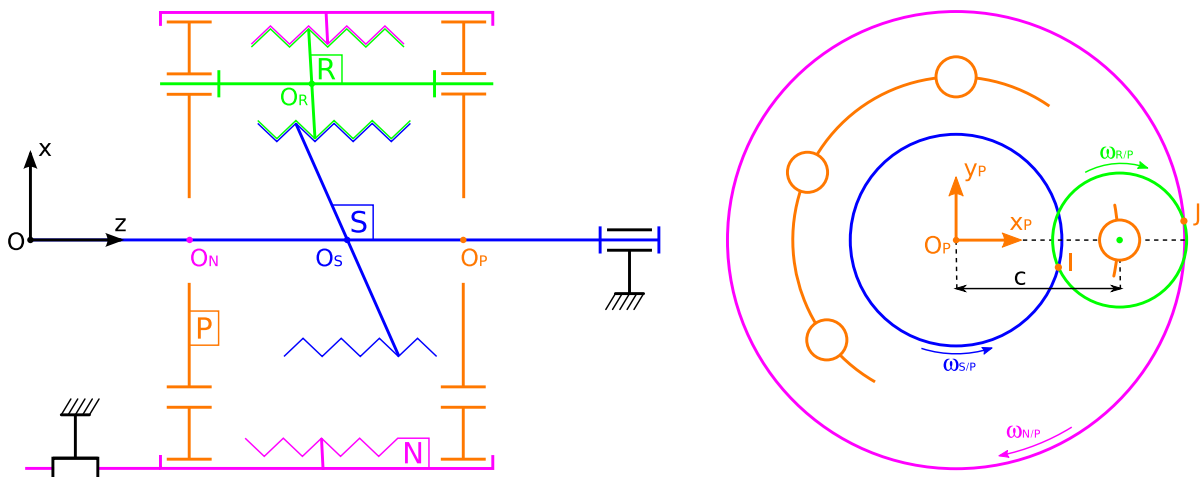


Figure 2.1: Kinematic diagram of a standard PRS with respect to the test bench (left) and the planet carrier (right)

Let  $c$  be the radial distance between the screw/nut/carrier and roller axes during the stationary regime. As shown on the right side of Fig. 2.1 and mentioned in [34] and [33], as well as detailed in the first chapter of this thesis, the contact points  $I$  between the screw and a given roller are usually not included in the plane formed by the axes of the two objects for a standard PRS. This is due to the difference in helix angles. The same is true for the contact points  $J$  between the nut and a roller in the case of an inverted PRS.

Let us now consider a reference frame  $(O_p, x_p, y_p, z)$  attached to  $P$  such that  $x_p$  points towards the center of one of the rollers. If the carrier is fixed as a reference, the relative motion of the other 3 components in the  $x_p y_p$  plane corresponds to pure rotations around  $z$ , which means that the geometrical  $x_p$  and  $y_p$  coordinates of the contact points remain constant in this frame. This simplifies equations a lot, because instead of deducing the contact points location during motion, we can use purely geometrical formulas like the ones deduced in appendix A and previously published in reference [11].

In the stationary regime, the mechanism's kinematics can be entirely defined by four variables, one for each component ( $S, R, N$  and  $P$ ). This is because all links on the left side of Fig. 2.1 only have one degree of freedom. Three of these variables are chosen to represent relative rotation speeds around  $z$  with respect to the planet carrier ( $\omega_{s/p}, \omega_{r/p}, \omega_{n/p}$ ), while the fourth variable quantifies the axial translation speed along  $z$  of the nut assembly with respect to the screw ( $\dot{z}_{n/s}$ ).

In the following paragraphs, we show how it is possible to reduce the number of kinematic variables from four to one, for both standard and inverted PRS. We thus obtain a kinematic model of the roller screw with only one degree of freedom in the form of a non-dimensional slip ratio  $\epsilon$ , which could afterwards be adjusted according to the forces, materials and lubricants present in the mechanism. The advantage of the proposed model is that it remains simple,

without making rough approximations on the location of the contact points and by allowing the lubricant and/or surface finish to have an influence on kinematics, as one would expect in reality.

The reduction of the number of variables becomes possible if we find three equations to link them. The first equation comes from assigning a numerical value to one of the speeds. For example, let us assume that the mechanism is powered by an external motor which imposes a constant rotation speed around  $z$   $\omega_{s/n} = \omega_0$  on the screw with respect to the Galilean frame (or the nut, since it can only translate along  $z$ ).

The second equation is obtained by expressing the fact that gears are present between some of the components and therefore two of the three rotation speeds are always linked. When the gear pitch diameters are equal to the thread nominal diameters, we say that gears are perfect. This feature is required when machining the rollers and it was investigated by Zhang et al. [16]-[17]. If the condition is not satisfied, roller migration might appear [15]. However, for perfect gears we have:

$$\begin{cases} \frac{\omega_{n/p}}{\omega_{r/p}} = \Gamma = \frac{r_R}{r_N} & \text{if standard PRS} \\ -\frac{\omega_{s/p}}{\omega_{r/p}} = \Gamma = \frac{r_R}{r_S} & \text{if inverted PRS} \end{cases} \quad (2.1)$$

where  $\Gamma$  represents the gear (overdrive) ratio, obtainable from pitch radii of PRS components.

Since the screw input speed  $\omega_{s/n}$  is imposed, we prefer replacing the  $\omega_{n/p}$  and  $\omega_{r/p}$  variables with the following non-dimensional ratios:

$$\epsilon = -\frac{\omega_{n/p}}{\omega_{s/n}} = \frac{\omega_{p/n}}{\omega_{s/n}} \quad \lambda = \frac{\omega_{r/p}}{\omega_{s/n}} \quad (2.2)$$

The first of these two ratios expresses how fast the planet carrier turns inside the nut, compared to the screw. It would be illogical for  $P$  to turn faster than  $S$ , therefore  $\epsilon \in [0, 1]$  in all cases. For a standard PRS, the value  $\epsilon = 0$  means that the carrier does not turn at all with respect to the nut. Due to the presence of gears, rollers will also have their rotation blocked, which means that the only component which turns is the screw. The mechanism is equivalent to a friction screw, where no rolling occurs. As  $\epsilon$  increases, the planet carrier starts to move and most of the pure sliding friction gets gradually transformed into rolling. This is why roller screws are interesting over friction screws in the first place. Therefore,  $\epsilon$  has a strong physical meaning and is an indicator of the mechanism performance. From now on,  $\epsilon$  will be called *slip ratio* and we will make it the only degree of freedom left in the kinematic model, as mentioned earlier.

With these considerations, the perfect gear Eq. 2.1 transforms into:

$$\begin{cases} -\frac{\epsilon}{\lambda} = \Gamma & \text{if standard PRS} \\ -\frac{1-\epsilon}{\lambda} = \Gamma & \text{if inverted PRS} \end{cases} \quad (2.3)$$

which can further be simplified by introducing a boolean variable  $\chi$  equal to 1 for standard roller screws and 0 for the inverted type. This leads to:

$$\lambda = -\frac{\epsilon\chi + (1-\epsilon)(1-\chi)}{\Gamma} \quad (2.4)$$

Finally, the third equation in our model is obtained by expressing the link between the axial  $z$  displacement of the nut assembly and the angle for which the screw turns in order to produce this displacement. From this point of view, roller screws must function exactly like friction screws in order to guarantee precision: no matter how well the rollers turn and what lubricant is used, one full turn of the screw must correspond to an axial displacement of the nut exactly

equal to its lead. The condition can be easily verified in practice and was also deduced by Velinsky et al. [2] using a different approach. If  $\theta_{s/n}$  is the signed angle for which the screw rotates with respect to the nut, we can express the equation as:

$$z_{n/s} = -\frac{l_s}{2\pi}\theta_{s/n} \Rightarrow \dot{z}_{n/s} = -\frac{l_s}{2\pi}\omega_{s/n} \quad (2.5)$$

Unknowns	Equations
$\omega_{s/p}$	$\omega_{s/n} = \omega_0$ imposed input speed
$\omega_{r/p} \rightarrow \lambda$	Eq. 2.4 perfect gear condition
$\omega_{n/p} \rightarrow \epsilon$	
$\dot{z}_{n/s}$	Eq. 2.5 stable displacement

Table 2.1: Kinematic model summary

A summary of the 4 unknowns and 3 equations used in our kinematic model is presented in table 2.1. The non-dimensional slip ratio  $\epsilon$  is left undetermined. For standard PRS, higher  $\epsilon$  values mean more rolling and less sliding, which is desirable. On the other hand, note that inverted PRS work the other way around. The full sliding case corresponds to  $\epsilon = 1$ , when  $\lambda = 0$  and the rollers don't turn with respect to the planet carrier. Due to gears between the screw and rollers, it is as if  $P$  and  $S$  were connected, both moving at the same speed within the nut. Rolling is added with decreasing values of  $\epsilon$ , although the value  $\epsilon = 0$  cannot be reached.

Hence, there exists a minimal value  $\epsilon^*$  which should be calculated. The same is true for standard PRS, where  $\epsilon = 1$  is impossible and a maximal value for  $\epsilon$  can be determined. In both cases, this extreme value of  $\epsilon$  called  $\epsilon^*$  would represent ideal functioning conditions for the mechanism, where sliding is reduced to a minimum. A method for calculating  $\epsilon^*$  is proposed in the following sections.

### 2.2.1 Sliding velocity at contact points

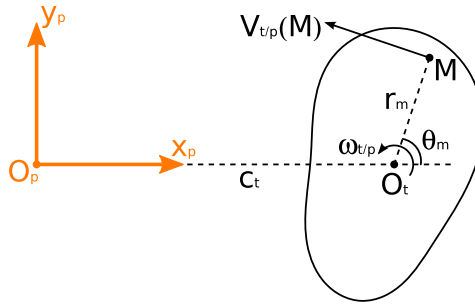


Figure 2.2: Velocity at a point  $M$  belonging to object  $T$ . Drawn in the  $x_p y_p$  plane of the planet carrier.

Let's consider an object  $T$  that turns around its center of rotation  $O_t$ , which translates along  $z$  in the frame of the planet carrier, as shown in Fig. 2.2. The only non-zero component of its rotation is along the  $z$  axis and its magnitude is noted  $\omega_{t/p}$ . We are interested in calculating the relative velocity vector at a point  $M$  of cylindrical coordinates  $(r_m, \theta_m)$ . Since the point belongs to the solid object  $T$ , we can write:

$$\vec{v}_{t/p}(M) = \vec{v}_{t/p}(O_t) + \vec{\Omega}_{t/p} \times \vec{O_t M} = \begin{bmatrix} 0 \\ 0 \\ \dot{z}_{t/p} \end{bmatrix} + \begin{bmatrix} 0 \\ 0 \\ \omega_{t/p} \end{bmatrix} \times \begin{bmatrix} r_m \cos \theta_m \\ r_m \sin \theta_m \\ 0 \end{bmatrix} = \begin{bmatrix} -\omega_{t/p} r_m \sin \theta_m \\ \omega_{t/p} r_m \cos \theta_m \\ \dot{z}_{t/p} \end{bmatrix} \quad (2.6)$$

where all vectors are expressed in the frame of the planet carrier. From now on, this will always be the case unless otherwise specified. This frame is preferred because the  $xy$  location of points  $I$  and  $J$  is fixed with respect to it, which allows us to use some useful equations in terms of geometry.

Equation 2.6 can then be applied to an object  $T$  which is either the screw, roller or nut in a PRS mechanism. When  $M$  corresponds to the location of the contact points  $I$  or  $J$ , we obtain:

$$\overrightarrow{v_{s/p}}(I) = \begin{bmatrix} -(\omega_{s/n} - \omega_{p/n})r_{IS} \sin \theta_{IS} \\ (\omega_{s/n} - \omega_{p/n})r_{IS} \cos \theta_{IS} \\ -\chi \dot{z}_{n/s} \end{bmatrix} \quad \overrightarrow{v_{r/p}}(I) = \begin{bmatrix} -\omega_{r/p}r_{IR} \sin \theta_{IR} \\ \omega_{r/p}r_{IR} \cos \theta_{IR} \\ 0 \end{bmatrix} \quad (2.7)$$

$$\overrightarrow{v_{n/p}}(J) = \begin{bmatrix} \omega_{p/n}r_{JN} \sin \theta_{JN} \\ -\omega_{p/n}r_{JN} \cos \theta_{JN} \\ (1 - \chi)\dot{z}_{n/s} \end{bmatrix} \quad \overrightarrow{v_{r/p}}(J) = \begin{bmatrix} -\omega_{r/p}r_{JR} \sin \theta_{JR} \\ \omega_{r/p}r_{JR} \cos \theta_{JR} \\ 0 \end{bmatrix} \quad (2.8)$$

The polar coordinates which define the radial and circumferential locations of  $I$  and  $J$  can be calculated using the numerical model proposed in appendix A or reference [11]. They are geometrically linked by Eq. A.1 such that:

$$\begin{cases} r_{IS} \sin \theta_{IS} - r_{IR} \sin \theta_{IR} = 0 \\ r_{IS} \cos \theta_{IS} - r_{IR} \cos \theta_{IR} = c \end{cases} \quad \begin{cases} r_{JN} \sin \theta_{JN} - r_{JR} \sin \theta_{JR} = 0 \\ r_{JN} \cos \theta_{JN} - r_{JR} \cos \theta_{JR} = c \end{cases} \quad (2.9)$$

Finally, if we also take into account Eqs. 2.2 and 2.5, we obtain the relative (sliding) velocity vectors at the  $I$  and  $J$  contact points:

$$\overrightarrow{v_I} = \overrightarrow{v_{s/r}}(I) = \overrightarrow{v_{s/p}}(I) - \overrightarrow{v_{r/p}}(I) = \begin{bmatrix} (\epsilon + \lambda - 1)r_{IS} \sin \theta_{IS} \\ c\lambda - (\epsilon + \lambda - 1)r_{IS} \cos \theta_{IS} \\ \chi \frac{l_s}{2\pi} \end{bmatrix} \omega_{s/n} \quad (2.10)$$

$$\overrightarrow{v_J} = \overrightarrow{v_{n/r}}(J) = \overrightarrow{v_{n/p}}(J) - \overrightarrow{v_{r/p}}(J) = \begin{bmatrix} (\epsilon + \lambda)r_{JN} \sin \theta_{JN} \\ c\lambda - (\epsilon + \lambda)r_{JN} \cos \theta_{JN} \\ (\chi - 1)\frac{l_n}{2\pi} \end{bmatrix} \omega_{s/n} \quad (2.11)$$

### 2.2.2 Kinematic constraints

To ensure that the roller screw mechanism functions correctly, the leads of the screw and the nut must be equal. However, this condition is often implicit and literature fails to provide a clear reasoning as to why it must be true. Some authors [2] have suggested basic geometry to be the cause, without giving any more details. Ma et al. [12] correctly identified kinematics as the real reason behind the condition, although the proof proposed by the authors uses simplifying assumptions.

In this section, we show how Eqs. 2.10 and 2.11 are used to deduce the  $l_n = l_s$  condition. One of the main hypotheses made in the current work is that solids are infinitely rigid at the macroscopic scale, such that local deformations have no effect on the global geometry. Therefore, in order to maintain permanent contact, the relative velocity at the contact points must be nil when projected in the normal directions at those points. We call these the *non-penetration conditions*:

$$\begin{cases} \overrightarrow{v_I} \cdot \overrightarrow{n_I} = 0 \\ \overrightarrow{v_J} \cdot \overrightarrow{n_J} = 0 \end{cases} \Leftrightarrow \begin{cases} v_{Ix}n_{Ix} + v_{Iy}n_{Iy} + v_{Iz}\gamma_I = 0 \\ v_{Jx}n_{Jx} + v_{Jy}n_{Jy} + v_{Jz}\gamma_J = 0 \end{cases} \quad (2.12)$$

where  $\overrightarrow{n_I}$  and  $\overrightarrow{n_J}$  are unit normal vectors, external to the *roller* surface at  $I$  and  $J$ . The corresponding  $\gamma_I$  and  $\gamma_J$  orientations are functions equal to -1 if the *top* face of the roller is used and 1 if the *bottom* face is in contact instead. For both the  $I_1J_2$  and the  $I_2J_1$  configurations, current literature [11, 33] shows that the mechanism is always loaded such that  $\gamma_I = -\gamma_J$ .

The  $n_{Ix}, n_{Iy}$  and  $n_{Jx}, n_{Jy}$  components are projections of the corresponding contact normal vectors in the  $x, y$  directions, multiplied by a negative constant such that the  $z$  projection equals  $\gamma$ . It is interesting to proceed this way due to the analytical form of  $\overrightarrow{n}$  provided by Eq. 1.27.

That equation can also be used to deduce the following geometric properties:

$$\begin{cases} 2\pi r_{IS}(n_{Ix} \sin \theta_{IS} - n_{Iy} \cos \theta_{IS}) & = \gamma_I l_s \\ 2\pi r_{IR}(n_{Ix} \sin \theta_{IR} - n_{Iy} \cos \theta_{IR}) & = \gamma_I l_r \\ 2\pi r_{JN}(n_{Jx} \sin \theta_{JN} - n_{Jy} \cos \theta_{JN}) & = \gamma_J l_n \\ 2\pi r_{JR}(n_{Jx} \sin \theta_{JR} - n_{Jy} \cos \theta_{JR}) & = \gamma_J l_r \end{cases} \quad (2.13)$$

When combined with Eq. 2.9, these properties transform the two *non-penetration conditions* into:

$$\begin{cases} (\epsilon + \chi - 1)l_s + \lambda l_r & = 0 \\ (\epsilon + \chi - 1)l_n + \lambda l_r & = 0 \end{cases} \quad (2.14)$$

which means that  $l_s = l_n$  in all cases, unless the mechanism is equivalent to a friction screw, when pure sliding occurs. This result supports the claim that the condition is required by the mechanism's kinematics and not only by its geometry.

Another interesting kinematic constraint can be deduced in the particular case when machining is perfect. For a standard PRS, this corresponds to an exact equality between the helix angles of the roller and the nut, such that the roller-nut contact  $J$  is centered and placed on the nominal radius, i.e.  $r_{JN} = r_N$  and  $\theta_{JN} = 0$ . Contact point velocity vectors in Eqs. 2.10-2.11 were written without taking into account the perfect gear Eq. 2.4, but if the relation is used we can deduce that  $\vec{v}_J = \vec{0}$ , which means that there is *no sliding* between the nut and the rollers. A similar analysis can be performed for inverted PRS, where *no sliding* can occur between the screw and the rollers if  $r_{IS} = r_S$  and  $\theta_{IS} = 0$ . In the general case, however, sliding can occur in all three directions and it is impossible to remove it completely. As mentioned by Velinsky et al. [2], a fixed amount of axial sliding will always be present. This corresponds to the  $z$  component of  $\vec{v}_I$  for standard PRS or  $\vec{v}_J$  for the inverted type.

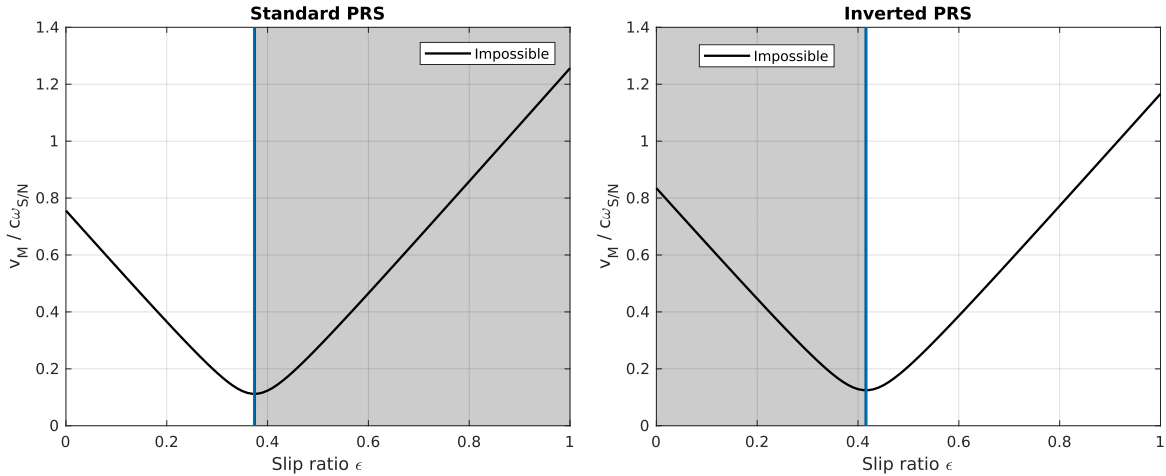


Figure 2.3: Non-dimensional sliding velocity at  $M$  ( $I$  for standard and  $J$  for inverted) for different  $\epsilon$  values.

On the other hand, it might be possible to significantly reduce sliding by modifying the value of the slip ratio  $\epsilon$ . Figure 2.3 shows qualitatively how the non-dimensional modulus of the sliding velocity at  $M$  (where  $M$  is either point  $I$  for a standard PRS or point  $J$  for the inverted type) varies according to  $\epsilon$ . Note that the y-axis corresponds to  $\frac{|\vec{v}_M|}{c \omega_{s/n}}$ , where  $\vec{v}_M$  was computed using Eqs. 2.10-2.11. The two sides of Fig. 2.3 use different mechanism geometries, although in both cases, the screw diameter is roughly 30 mm and its lead equals 10 mm.

The figure shows that for both standard and inverted PRS, there exists an ideal value of  $\epsilon$  for which sliding gets minimized. This value, called  $\epsilon^*$ , also limits the range of possible slip ratios. We can calculate  $\epsilon^*$  according to the following equation:

$$\frac{d|\vec{v}_M|}{d\epsilon} = 0 \quad (2.15)$$

which eventually leads to:

$$\text{standard PRS: } \epsilon^* = \frac{-\Gamma \left(1 - \Gamma - \frac{c}{r_{IS}} \cos \theta_{IS}\right)}{(1 - \Gamma) \left(1 - \Gamma - 2 \frac{c}{r_{IS}} \cos \theta_{IS}\right) + \left(\frac{c}{r_{IS}}\right)^2} \quad (2.16)$$

$$\text{inverted PRS: } \epsilon^* = \frac{1 + \Gamma - (2 + \Gamma) \frac{c}{r_{JN}} \cos \theta_{JN} + \left(\frac{c}{r_{JN}}\right)^2}{(1 + \Gamma) \left(1 + \Gamma - 2 \frac{c}{r_{JN}} \cos \theta_{JN}\right) + \left(\frac{c}{r_{JN}}\right)^2} \quad (2.17)$$

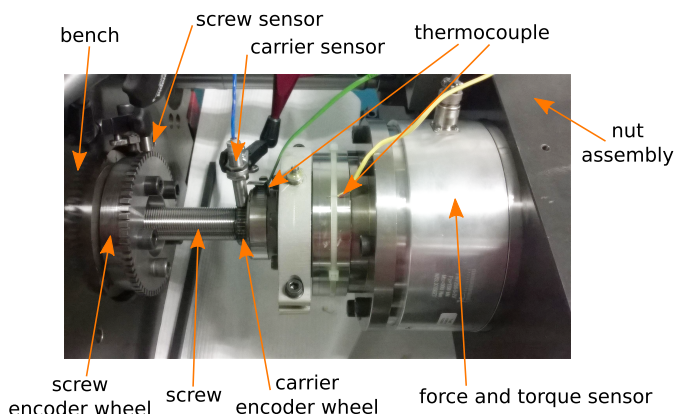
Hence, the ideal slip ratio  $\epsilon^*$  can be obtained from Eqs. 2.16 – 2.17, which only depend on geometrical quantities. These formulas were used to draw the vertical lines in Fig. 2.3.

In conclusion, it is possible to express all the stationary regime kinematics in the PRS mechanism as a function of the screw input speed  $\omega_s/n$  and one degree of freedom, in the form of the non-dimensional slip ratio  $\epsilon$ . However, the speed can easily be specified, while  $\epsilon$  is much more difficult to control. It is possible to calculate the value numerically using a dynamic model like the one published by Fu et al. [28] or in the stationary case, the model described in the third chapter of the current work. But the program needs to take into account all the different friction sources, lubrication conditions, thermal effects, etc. which makes it a complex and potentially expensive task.

In the next section, we explore a different option. Instead of calculating the stationary value of  $\epsilon$ , we attempt to measure it experimentally to see if there is significant room left for improvement. In all cases, the kinematic model developed earlier predicts a certain allowed interval for this slip ratio, as well as an ideal value  $\epsilon^*$ , which should be approached to reduce the amount of sliding in the mechanism. These conditions are summarized below:

$$\begin{aligned} \text{standard PRS: } \epsilon &\in [0, \epsilon^*] && \text{where } \epsilon^* \text{ defined by Eq. 2.16} \\ \text{inverted PRS: } \epsilon &\in [\epsilon^*, 1] && \text{where } \epsilon^* \text{ defined by Eq. 2.17} \end{aligned}$$

### 2.2.3 Experimental results



screw pitch radius	$r_s$	14.95 mm
screw lead	$l_s$	10 mm
screw thread	$n_s$	5 starts
roller thread	$n_r$	1 start
pressure angle	$\alpha_n$	45°
number of rollers	$N_R$	9
number of contacts	$N_C$	28
grease		SKF LGWA 2
length of track		250 mm
motor acceleration		500 mm/s <sup>2</sup>

Figure 2.4: Experimental apparatus for measuring  $\epsilon$

As shown in the previous sections, the amount of sliding which occurs in a given roller screw can be characterized by the slip ratio  $\epsilon$ . For the purposes of the current work,  $\epsilon$  was measured using the setup presented in Fig. 2.4. The experimental device uses a standard PRS and follows the same kinematic diagram as the one shown in Fig. 2.1, where the screw is powered by a motor to rotate with respect to the test bench, while the nut assembly can only translate. When the screw turns clockwise, it pushes the nut assembly towards the right. The motor is placed on the left side and is not shown in Fig. 2.4. Two thermocouples used to monitor temperature are

also present on the apparatus, although we don't discuss thermal effects on  $\epsilon$  in this memoir. All the experiments were conducted at a room temperature of 20°C.

The motor can be controlled such that we are able to specify a target speed for the screw. As the screw starts turning, the nut assembly translates along its track with increasing speed. The stationary regime, which corresponds to approximately constant velocities, begins when the target screw speed is attained. It lasts long enough for us to gather sufficient data points, then ends when the end of the track is reached and the mechanism stops.

The roller screw is loaded using a system of two parallel hydraulic cylinders, not shown in Fig. 2.4. These cylinders apply a constant resistive force on the nut assembly, directed towards the left. Its magnitude is adjustable and can be measured with a sensor based on deformable elements. This sensor can also measure the torque applied on the nut, which allows the measurement of mechanism efficiency.

A more precise value of the screw speed can be obtained from a Hall effect sensor, placed close to an encoder wheel fixed to the shaft. The wheel has grooves machined into it, which can be counted to determine the angle traveled by the screw in a certain amount of time. A similar setup is used to measure the angular speed of the planet carrier. If the two values are known, their ratio is equal to  $\epsilon$ , according to Eq. 2.2.

We have investigated two methods for determining  $\epsilon$  from the speed signals. The first method consisted in plotting  $\epsilon$  as the point-by-point ratio of the carrier and screw speeds, then calculating the average of the obtained signal when the mechanism was in a steady state. This method proved to be very inaccurate with regard to the expected behavior and was discarded. In the second method, we calculated the averages of the two speed signals first, then computed  $\epsilon$  as the ratio of the obtained averages. Better tendencies were observed and the method was retained.

A total of 15 experiments have been performed using a standard PRS with dimensions and lubricant mentioned in the table in Fig. 2.4. The rectified screw diameter was approximately 30 mm. Each experiment was conducted for different values of the external force on the nut  $F_N$  and input speed on the screw  $\omega_{s/n}$ , in order to sweep the entire range available on the test bench. The tested domain with the obtained values for  $\epsilon$  and the measured torque on the nut  $C_N$  are presented in Fig. 2.5.

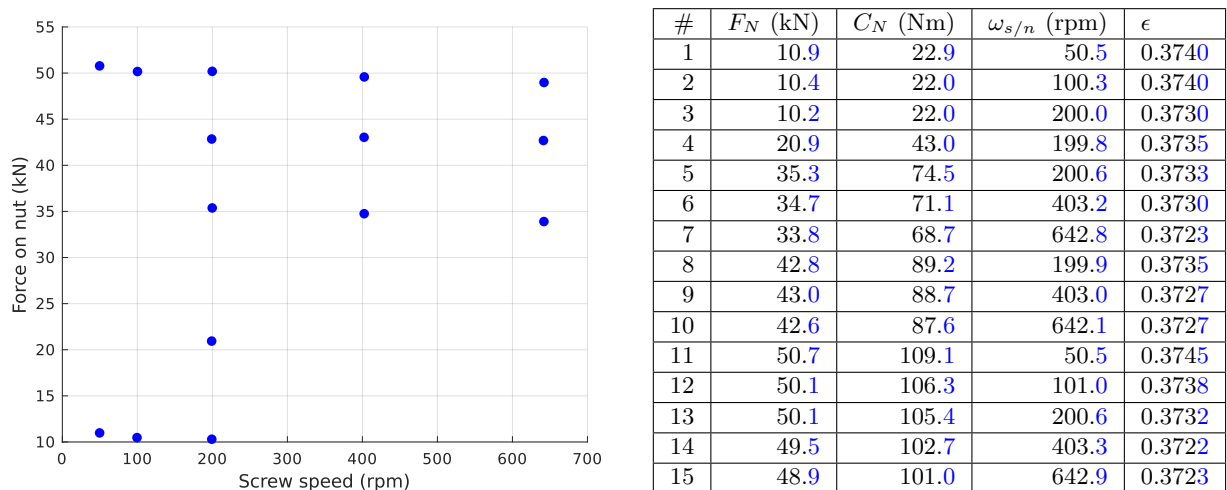


Figure 2.5: Test domain and results

For each experiment, the number of discrete points in the speed and force/torque signals was different. However, a minimum of 3000 points on the speeds and 600 points on the force and torque has been assured for calculating the averages shown in Fig. 2.5. In some of the experiments, we have recorded up to 25,000 points on the speeds and 11,000 points on the force. However, we found that in all cases the minimum number is large enough to guarantee a sufficient precision on the computed averages. Even if we took 3 times less points than the minimum, the results in Fig. 2.5 would only change their last digit (in blue). Hence, the order of

magnitude for the measurement error is  $10^{-1}$  on the force (kN), torque (Nm) and speeds (rpm) and  $10^{-4}$  on the slip ratio  $\epsilon$ .

Let us now compare these experimental results with the kinematic model described in the previous sections. For the particular dimensions of the tested roller screw, the theoretical value of  $\epsilon^*$  calculated using Eq. 2.16 yields:

$$\epsilon^* = 0.3741 \quad (2.18)$$

which is higher than most of the measured values presented in Fig. 2.5, as expected. Only experiment 11 yields a value higher than  $\epsilon^*$ , but the difference can be attributed to measurement error. These results confirm the fact that Eq. 2.16 is a good estimation for the maximum value of  $\epsilon$ . On the real PRS, there is always a small amount of circumferential slip which prevents  $\epsilon$  from reaching  $\epsilon^*$ . This slip is inherent to the PRS and is necessary for overcoming some of the internal power dissipation sources, like the spin motion described in the following sections. Highly dissipative mechanisms require more sliding; therefore, one should try to reduce the  $|\epsilon - \epsilon^*|$  difference by using better lubricants or optimized geometrical parameters such as profile curvatures.

Furthermore, we can define the optimality of the mechanism as a percentage:

$$\%_{\epsilon} = \frac{\epsilon + \chi - 1}{\epsilon^* + \chi - 1} \cdot 100 \quad (2.19)$$

in order to show how close we are to the ideal ratio  $\epsilon^*$ , for both standard and inverted PRS. Based on the results in Fig. 2.5, this percentage has been plotted in Fig. 2.6, where the black dots represent measured data and the mesh is a linear surface interpolation, computed using the `griddata` function in Matlab.

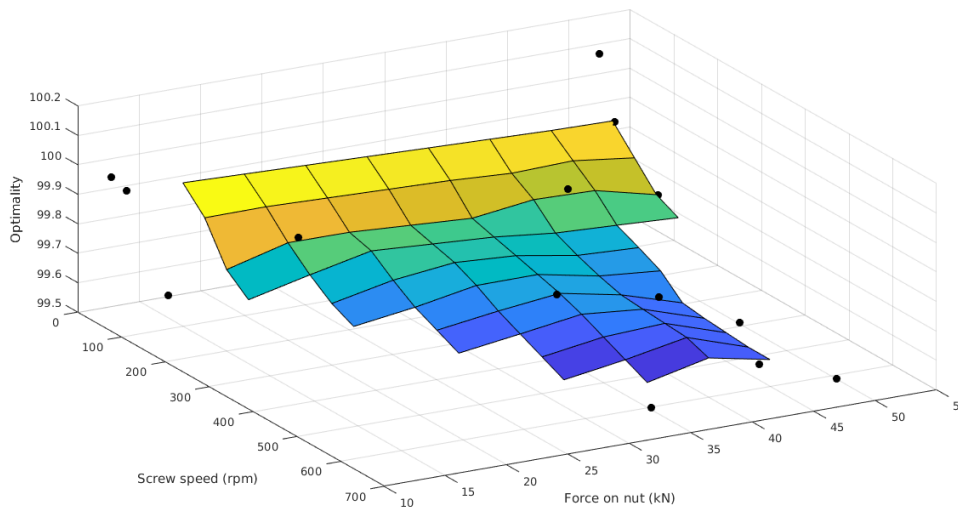


Figure 2.6: Measured optimality on the test domain, with linear interpolation

We can see that optimality takes slightly higher values at lower speeds, which is expected since sliding is less likely to occur in those regions and for a standard PRS, optimality (and  $\epsilon$ ) increases as the amount of sliding decreases. This is because at lower speeds the lubrication regime is less hydrodynamic and mixed contacts are more likely to occur, increasing the friction coefficients and leading to less sliding. Note that speed variations are obtained on a limited range, due to the current capabilities of the test bench.

In terms of the resistive force on the nut, optimality variations are not sufficiently clear and cannot be interpreted. We expected sliding to decrease with increasing force, as the surfaces are pushed together more, making dry contacts more likely to occur on the surface roughness. Therefore, optimality (and  $\epsilon$ ) values should increase with the force. From Fig. 2.6, however, we cannot confirm this prediction. The observed behavior as a function of load may be due to

more complex system deformations. In the current study, infinitely rigid solids are used for the global geometry and kinematics.

The overall optimality is higher than 99.5%, which leaves little room for improvement in terms of stationary regime kinematics. This particular roller screw performed very well in the test conditions. However, other greases or loading parameters might lead to a different scenario.

#### 2.2.4 Comparison with literature

The idea that on a standard roller screw,  $\epsilon$  should be slightly inferior to an ideal  $\epsilon^*$  is not new in current literature. Jones et al. [44], for example, mentions that the orbital angular velocity of the roller ( $\omega_{p/n}$  in the current work) is lower in the dynamic system, in comparison with the slip-free kinematic behavior. The authors do not measure  $\epsilon$  experimentally; instead, they propose a transient, dynamic model which calculates it as a function of time. If we rewrite their equations with the notations used here, we would obtain the following value for  $\epsilon$  at steady-state:

$$\epsilon = r_{IS} \frac{c \cos \theta_{IS} - r_{IR} \left( \frac{1}{\Gamma} - 1 \right) (\cos \theta_{IS} \cos \theta_{IR} + \sin \theta_{IS} \sin \theta_{IR})}{r_{IR}^2 \left( \frac{1}{\Gamma} - 1 \right)^2 + c^2 - 2cr_{IR} \left( \frac{1}{\Gamma} - 1 \right) \cos \theta_{IR}} \quad (2.20)$$

Hence, for the dimensions of the PRS which we tested, the model in reference [44] yields  $\epsilon = 0.3740$ , which is close to some of the measured values and also lower than  $\epsilon^*$ . Although this confirms that the cited paper provides a satisfying method to obtain the kinematic ratio  $\epsilon$  without performing any experiments or simulations, the result solely depends on geometry. In our view, the screw input speed, lubricant properties and/or dynamics should also have an effect on the value of  $\epsilon$ . A more complete numerical model is proposed in chapter 3 in the current memoir.

Reference [44] was recently used by Fu et al. [28] to validate an advanced transient dynamic model of the PRS, providing one way to take the additional variables into consideration. The authors performed numerical simulations on a standard roller screw with different dimensions than the one we used for our experiments, so comparing  $\epsilon$  values with the current work would be inaccurate. However, the model in reference [28] shows that at steady-state, a higher resistive force on the nut increases  $\epsilon$ , as expected. Higher friction coefficients are shown to have the same effect.

Finally, a quick and much simpler alternative to Eq. 2.20 has been proposed by Ma et al. [18] and Velinsky et al. [2]:

$$\epsilon = \frac{1 - 2\Gamma}{2(1 - \Gamma)} \quad (2.21)$$

which yields for  $\Gamma = 0.2$  a steady-state value of  $\epsilon = 0.3750$ . The same result can be obtained from Eq. 2.20 by taking  $\theta_{IS} = 0$  and  $\theta_{IR} = -\pi$  and would correspond to a roller screw which closely resembles planetary gear trains. The value is not influenced by the contact position, kinematics or dynamics, but does provide a fast, approximate estimation of the maximum value that  $\epsilon$  (or even  $\epsilon^*$ ) could take.

### 2.3 Local contact model

This section links the global kinematic model described earlier with the local geometry of the contact areas investigated in chapter 1. We provide a way of obtaining the relative velocity field at all points within the Hertzian ellipse. This is very useful for investigating local phenomena involved in the power dissipation of the PRS.

Let us assume that the shape, size and orientation of the Hertzian ellipse are known for both the roller-screw contact and the roller-nut contact in a given PRS. The rectangle bordering the contact area can be discretized by a grid made of  $N_1 \times N_2$  points, as shown in Fig. 2.7. The relative (sliding) velocity vector at the center of the ellipse has been calculated before for  $I$  and

$J$  as a function of geometry and the kinematic ratio  $\epsilon$  (see Eqs. 2.10-2.11) and it has been shown that  $\vec{v}_{1/2}(M) \cdot \vec{n} = 0$  (*non-penetration conditions*), where  $\vec{n} = \vec{t}_1 \times \vec{t}_2$  is a surface normal vector at  $M$  and the subscript 1/2 refers to surfaces 1 and 2 in contact (see Fig. 1.11). We are now interested in the sliding velocity at any given point  $D$  within the ellipse.

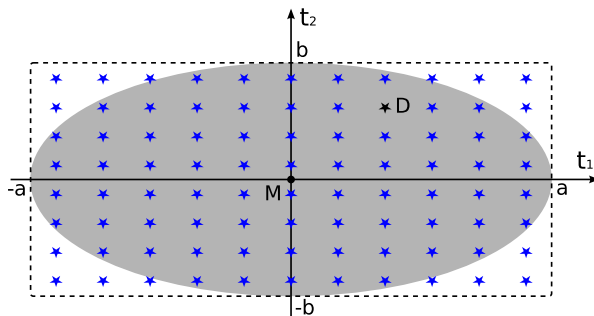


Figure 2.7: Contact area discretization for  $N_1 = 11$  and  $N_2 = 8$

If the coordinates of  $D$  in the  $(\vec{t}_1, \vec{t}_2)$  frame are  $(t_{1D}, t_{2D})$ , we can express  $\vec{v}_{1/2}(D)$  as:

$$\vec{v}_D = \vec{v}_{1/2}(D) = \vec{v}_{1/2}(M) + \vec{\Omega}_{1/2} \times \vec{MD} \Leftrightarrow \begin{cases} \vec{v}_D \cdot \vec{t}_1 &= \vec{v}_M \cdot \vec{t}_1 - \omega_{1/2} (\vec{n} \cdot \vec{z}) t_{2D} \\ \vec{v}_D \cdot \vec{t}_2 &= \vec{v}_M \cdot \vec{t}_2 + \omega_{1/2} (\vec{n} \cdot \vec{z}) t_{1D} \\ \vec{v}_D \cdot \vec{n} &= \omega_{1/2} (\vec{t}_1 \cdot \vec{z}) t_{2D} - \omega_{1/2} (\vec{t}_2 \cdot \vec{z}) t_{1D} \approx 0 \end{cases} \quad (2.22)$$

where point  $M$  can either be the screw-roller contact  $I$  or nut-roller contact  $J$ . We also assumed that the relative angular velocity vector can only have an axial component, i.e.  $\vec{\Omega}_{1/2} = \omega_{1/2} \cdot \vec{z}$ . This is true for the idealized PRS mechanism studied in this memoir, where roller axes remain parallel to the screw and nut axes at all times.

Equation 2.22 shows that  $\vec{v}_D \cdot \vec{n}$  is not nil, in general. It is only true if  $D$  coincides with the ellipse center  $M$ . In reality, however, we would expect the non-penetration condition to hold true for all points within the contact area. The model proposed here neglects the influence of local deformations on the global geometry and location of the contact points, which are deduced for infinitely rigid solids. Therefore, points on the calculated Hertz ellipse do not necessarily belong to actual surfaces. In the following,  $\vec{v}_D \cdot \vec{n}$  is considered to be negligible compared to the other two components, which are taken to be the only relevant ones for modeling local kinematics.

The relative angular speed  $\omega_{1/2}$  can be easily deduced for  $I$  and  $J$  using Eq. 2.2:

$$\omega_{s/r} = \omega_{s/n} - \omega_{p/n} - \omega_{r/p} = (1 - \epsilon - \lambda)\omega_{s/n} \quad (2.23)$$

$$\omega_{n/r} = -\omega_{p/n} - \omega_{r/p} = -(\epsilon + \lambda)\omega_{s/n} \quad (2.24)$$

where  $\lambda$  and  $\epsilon$  are linked by the gear Eq. 2.4.

According to these considerations, the sliding velocity vector at any point  $D$  inside the roller-screw or roller-nut contact areas can be calculated as a function of the rigid geometry,  $\epsilon$  and the input speed on the screw. The shape and orientation of the Hertzian ellipse can also be determined from rigid geometry and if the contact normal force is also known, we can deduce its actual size. As an example, the  $\vec{v}_D$  velocity field for both the  $I$  and  $J$  contacts is presented in Fig. 2.8 for the standard PRS used in the previous section to measure  $\epsilon$ .

We can see from the figure that the two contacts are quite different in terms of the local sliding velocity field. The movement at the roller-nut contact  $J$  is a pure spin, while the roller-screw contact  $I$  is characterized by a combination of spin and uniform sliding, where the latter is predominant. This is due to the geometrical position of points  $I$  and  $J$ , which imposes the *no sliding* condition to occur between the nut and the rollers ( $\vec{v}_J = \vec{0}$ ). Of course, this can only be true for a standard PRS and the two figures should be swapped for the inverted type. Also, note that the arrow amplitudes for contacts  $I$  and  $J$  were not plotted using the same scale. For the left side of Fig. 2.8, the maximum sliding speed is 107 mm/s, while on the right side, the maximum is only 9.3 mm/s.

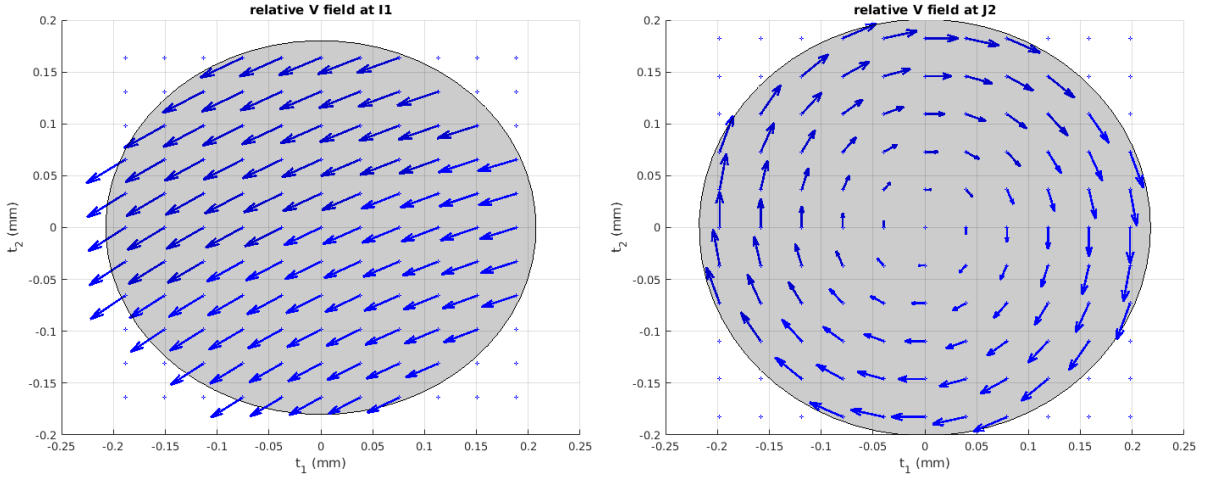


Figure 2.8: Sliding velocity field for the PRS in Fig. 2.4. Normal forces  $N_I = 223\text{N}$ ,  $N_J = 197\text{N}$ ,  $N_1 = N_2 = 11$  points,  $\epsilon = 0.3730$  and  $\omega_{s/n} = 400\text{rpm}$ .

### 2.3.1 Friction coefficient

Any quantitative analysis of the power dissipated through thread contacts in the PRS mechanism also involves identifying the ratio between tangential and normal contact forces. This ratio (known as the friction coefficient  $\mu$ ) can be imposed, measured or determined through a variety of models, some of which are investigated in the current section. Lubrication conditions should have a direct impact on  $\mu$ , global kinematics and roller screw performance, contrary to some of the models found in the current literature.

The simplest solution would be to use the Coulomb friction model and assume the friction coefficient to be constant. In view of the results detailed later in this section, this approach *could* be sufficiently accurate for estimating power dissipation through thread contacts. However, the convenience of its simplicity comes at a cost, since the model needs a carefully chosen value of  $\mu$  which corresponds to reality. For any lubricant, it is hard to correctly impose  $\mu$  without previously performing more advanced studies.

Another option would be to assume that the lubricant is an incompressible, Newtonian fluid, in which the shear stress is proportional to the sliding velocity gradient developed within the film thickness. For a steady, Couette flow, this relationship could be written as:

$$\frac{\mu N}{s} = \eta \frac{|\vec{v}_D|}{h_c} \quad (2.25)$$

where  $N$  is the contact normal load,  $s$  the surface of the Hertz ellipse and  $h_c$  the film thickness. The relative (sliding) velocity  $\vec{v}_D$  can be calculated using Eq. 2.22 and the proportionality coefficient  $\eta$  represents the dynamic viscosity of the lubricant.

This approach for calculating  $\mu$  has several problems. First of all, it would only work for one contact type (the roller-screw contact  $I$  for the standard PRS or the roller-nut contact  $J$  for the inverted PRS). This is because the sliding velocity field  $\vec{v}_D$  is roughly constant for those contacts only, as shown in Fig. 2.8. In order to account for friction losses through spin, a local model needs to be developed, such that the friction coefficient  $\mu$  is no longer a constant, but a scalar field over the discretized contact area.

The second problem is that the dry contact pressure can increase up to several GPa as we move closer to the center of the Hertz ellipse. On the one hand, we could assume that the viscosity of the lubrication fluid is an independent variable, equal to the one measured at ambient pressure ( $10^5\text{Pa}$ ). The most viscous of lubricants rarely reach  $1\text{Pa}\cdot\text{s}$ ; for a film thickness of 300 nm the example in Fig. 2.8 would yield a friction coefficient of the order  $10^{-4}$  for  $I$ , which is extremely low and does not make sense. On the other hand, if we suppose that viscosity is a function of pressure, such that it can be modeled by a Barus [45] or even Roelands [46] relation,  $\mu$  values would be much higher than 1, which again is inaccurate.

Given these considerations, we decided to develop a non-Newtonian lubricant model using the Eyring stress. This approach was studied for a wide range of operating conditions by Jacod et al. [47], who proposed a simple, general formula predicting the friction coefficient in smooth, isothermal, elliptic EHL contacts as a function of the characteristic shear stress:

$$\bar{\mu} = \sinh^{-1} \left( \frac{\bar{\tau}_c}{5} \right) \quad (2.26)$$

Equation 2.26 uses non-dimensional variables, which are detailed in reference [47]. The authors used three different types of lubricants and also compared their findings to some of the experimental data available in the literature at the time. However, the predicted coefficient of friction is a unique value for the whole contact. In the current work, we discretize the ellipse and use Eq. 2.26 to deduce the local, scalar  $\mu_D$  field. We do this mainly to account for friction losses in the case of pure spin, because considering the central sliding speed only would result in zero power losses for pure spin (see Fig. 3.8 in chapter 3). Therefore, the model is defined as:

$$\mu_D = \frac{\tau_0}{P_D} \sinh^{-1} \left( \frac{\bar{\eta}_D \cdot \bar{S}_D}{5H_c} \right) \quad (2.27)$$

where  $\tau_0$  is the Eyring stress,  $P_D$  the local pressure field,  $\bar{\eta}_D$  the non-dimensional local viscosity,  $H_c$  the non-dimensional central film thickness and  $\bar{S}_D$  a local parameter which depends on the slide to roll ratio.

According to the Hertzian dry contact model, the local pressure  $P_D$  depends on the distance from the center point  $M$  in Fig. 2.7 such that:

$$P_D = P_h \sqrt{1 - \left( \frac{t_{1D}}{a} \right)^2 - \left( \frac{t_{2D}}{b} \right)^2} \quad (2.28)$$

where  $(t_{1D}, t_{2D})$  are the coordinates of  $D$  in the  $(\vec{t}_1, \vec{t}_2)$  frame and  $P_h$  is the maximum Hertzian pressure given by Eq. 1.83. Hence, pressure is highest at the contact center, then decreases to negligible values near the edge of the ellipse.

The non-dimensional viscosity field  $\bar{\eta}_D$  is modeled by a Roelands [46] relation to local pressure:

$$\bar{\eta}_D = \exp \left( (\ln \eta_0 + 9.67) \cdot \left( \left( 1 + \frac{P_D}{P_0} \right)^{0.6} - 1 \right) \right) \quad (2.29)$$

where  $\eta_0$  is the ambient pressure viscosity and  $P_0$  a constant equal to 0.198 GPa.

Regarding the non-dimensional slide to roll ratio  $\bar{S}_D$ , reference [47] suggests that:

$$\bar{S}_D = \frac{2}{\tau_0} \frac{|\vec{v}_D|}{|\vec{u}_D|} \sqrt{|\vec{u}_D| \eta_0 E' \rho_x} \quad (2.30)$$

where  $E'$  is the relative Young modulus given by Eq. 1.79 and  $\rho_x$  a characteristic curvature in the sliding direction. The problem with PRS contacts is that the sliding velocity is usually not aligned with the ellipse axes. Moreover, it is impossible to identify a unique sliding direction for a field of pure spin, like the one showed for  $J$  in Fig. 2.8. Luckily, common ellipticity ratios are relatively close to 1, such that for this particular aspect we can safely assume the contact to be smaller, but circular without changing the results much. In the current work, we use:

$$\rho_x = \max(|\rho_1|, |\rho_2|) = |\rho_2| \quad (2.31)$$

where  $\rho_{1,2}$  are the two *relative* principal surface curvatures, calculated at the contact center using Eq. 1.73.

In order to compute the discretized slide to roll ratio  $\bar{S}_D$ , we need not only the relative (sliding) velocity field  $\vec{v}_D$ , but also the sum (rolling) velocity field  $\vec{u}_D$ . At points  $I$  and  $J$ , this field can be easily calculated by changing the sign of  $\lambda$  in Eqs. 2.10 – 2.11:

$$\vec{u}_I = \vec{v}_{s/p}(I) + \vec{v}_{r/p}(I) = \begin{bmatrix} (\epsilon - \lambda - 1)r_{IS} \sin \theta_{IS} \\ -c\lambda - (\epsilon - \lambda - 1)r_{IS} \cos \theta_{IS} \\ \chi \frac{l_s}{2\pi} \end{bmatrix} \omega_{s/n} \quad (2.32)$$

$$\vec{u}_J = \vec{v}_{n/p}(J) + \vec{v}_{r/p}(J) = \begin{bmatrix} (\epsilon - \lambda)r_{JN} \sin \theta_{JN} \\ -c\lambda - (\epsilon - \lambda)r_{JN} \cos \theta_{JN} \\ (\chi - 1)\frac{l_n}{2\pi} \end{bmatrix} \omega_{s/n} \quad (2.33)$$

We could then compute  $\vec{u}_D$  at any discretization point using something similar to Eq. 2.22:

$$\begin{cases} \vec{u}_D \cdot \vec{t}_1 &= \vec{u}_M \cdot \vec{t}_1 - (\omega_{1/p} + \omega_{2/p}) (\vec{n} \cdot \vec{z}) t_{2D} \\ \vec{u}_D \cdot \vec{t}_2 &= \vec{u}_M \cdot \vec{t}_2 + (\omega_{1/p} + \omega_{2/p}) (\vec{n} \cdot \vec{z}) t_{1D} \\ \vec{u}_D \cdot \vec{n} &= \vec{u}_M \cdot \vec{n} + (\omega_{1/p} + \omega_{2/p}) \left( (\vec{t}_1 \cdot \vec{z}) t_{2D} - (\vec{t}_2 \cdot \vec{z}) t_{1D} \right) \end{cases} \quad (2.34)$$

However, as the  $(t_{1D}, t_{2D})$  coordinates of  $D$  are small and the sum velocity is usually much higher than the relative velocity, we can safely neglect the second components due to transport, such that:

$$\vec{u}_D \approx \vec{u}_M \quad \forall D \quad (2.35)$$

where point  $M$  is either the screw-roller contact  $I$  or the nut-roller contact  $J$ . Furthermore, as we are only looking for the projection of rolling velocity in the contact plane, it leads to:

$$|\vec{u}_D| = \vec{u}_M \cdot \left( \vec{n} \times \left( \frac{\vec{u}_M}{|\vec{u}_M|} \times \vec{n} \right) \right) = |\vec{u}_M| - \frac{(\vec{u}_M \cdot \vec{n})^2}{|\vec{u}_M|} \quad \forall D \quad (2.36)$$

where  $\vec{u}_M$  can be determined with Eqs. 2.32 – 2.33.

Finally, the last parameter we need for computing the friction coefficient in Eq. 2.27 is the non-dimensional central film thickness  $H_c$ . In the current work, we preferred to use the same expression as reference [47], which is a simplification of the general Moes-Venner formula for circular contacts:

$$H_c = 1.7M^{-1/9}L^{3/4} \quad (2.37)$$

$$M = \frac{N\rho_x^2}{E'U^{3/4}} \quad L = \alpha E'U^{1/4} \quad U = \frac{\eta_0 |\vec{u}_D| \rho_x}{E'} \quad (2.38)$$

where  $N$  is the normal contact load and  $\alpha$  the pressure-viscosity coefficient of the lubricant. The dimensional central film thickness can then also be computed:

$$h_c = \frac{H_c \sqrt{U}}{\rho_x} \quad (2.39)$$

### 2.3.2 Numerical results

An example of the type of results which can be obtained with the Jacod [47] friction model described earlier is presented in Fig. 2.9. The figure plots the scalar  $\mu_D$  field computed with Eq. 2.27 for both the  $I$  and  $J$  contacts of the standard PRS described in Fig. 2.4 and used in the experiments to measure the slip ratio  $\epsilon$ . Normal contact forces,  $\epsilon$ , lubricant parameters and the screw speed  $\omega_{s/n}$  were imposed, in order to obtain a numerical simulation of experiment #6 from the list in Fig. 2.5.

These results show that friction coefficients are higher for the roller-screw  $I$  contact, when compared to  $J$ . This is expected, since sliding velocities are much higher, while the maximum Hertzian pressure and predicted film thickness is roughly the same ( $h_{cI} = 438 \text{ nm} / P_{hI} = 2.5 \text{ GPa}$  and  $h_{cJ} = 495 \text{ nm} / P_{hJ} = 2.1 \text{ GPa}$ ). The shape of the field is also different:  $\mu_D$  looks like a molten chocolate cake for  $I$  and more like a doughnut for  $J$ . This results from the combination

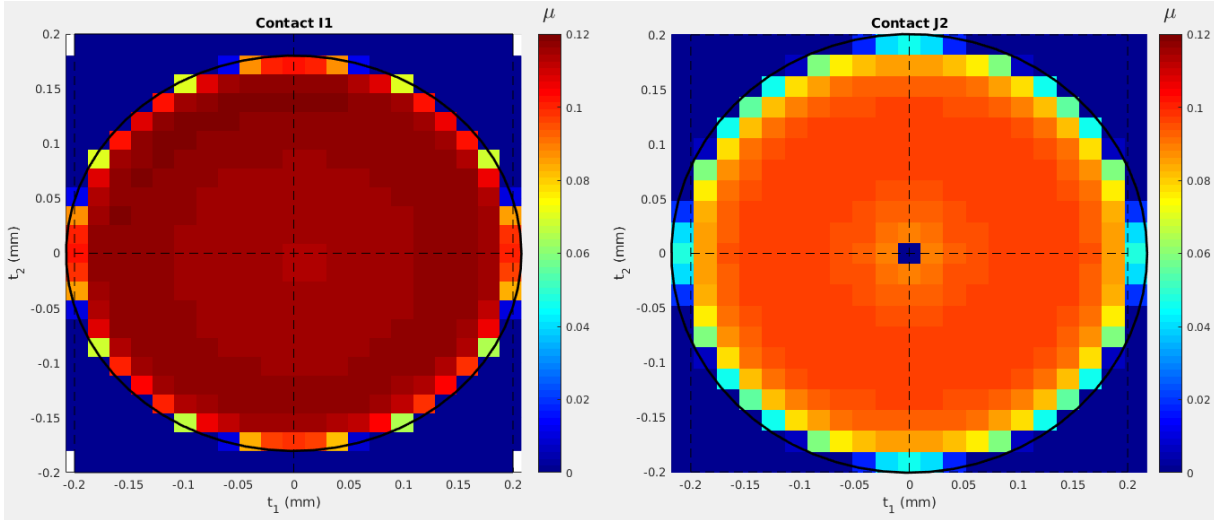


Figure 2.9: Discrete friction coefficient for the PRS in Fig. 2.4. Numerical simulation of experiment #6 in Fig. 2.5. Normal loads  $N_I = 223\text{N}$  ( $P_{hI} = 2.5\text{ GPa}$ ),  $N_J = 197\text{N}$  ( $P_{hJ} = 2.1\text{ GPa}$ ),  $N_1 = N_2 = 21$  points,  $\epsilon = 0.3730$  and  $\omega_{s/n} = 400\text{ rpm}$ . Lubricant (SKF LGWA2):  $\eta_0 = 166.5\text{ mPas}$ ,  $\alpha = 30\text{ GPa}^{-1}$ ,  $\tau_0 = 12\text{ MPa}$ .

of the velocity fields shown in Fig. 2.8 (which leads to a nil vector at point  $J$ ) and the pressure dome given by Eq. 2.28, which changes the viscosity.

Globally, however,  $\mu_D$  does not vary that much inside the contact area, which leads us to believe that a simple Coulomb model would also be sufficiently accurate in predicting power dissipation, provided that relevant friction coefficients are given for  $I$  and  $J$ . One way to obtain these constant coefficients would be to use the described numerical model to compute an average  $\mu_a$  for all  $N_a$  points inside the ellipse:

$$\mu_a = \frac{1}{N_a} \sum \mu_D \quad (2.40)$$

For the example given in Fig. 2.9,  $\mu_a = 0.111$  for  $I$  and  $\mu_a = 0.083$  for  $J$ . It would also be interesting to see how the model behaves when different lubricant parameters and slip ratios are chosen. Figure 2.10 shows the computed average friction coefficient  $\mu_a$  for several lubricants, with a detailed legend in table 2.2.

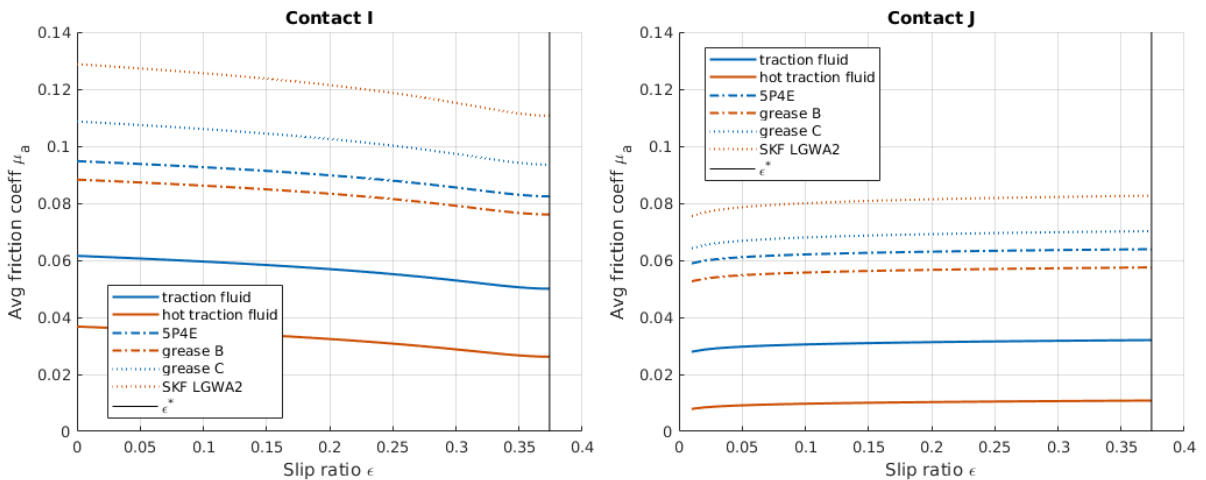


Figure 2.10: Influence of  $\epsilon$  and lubricant parameters on the average friction coefficient  $\mu_a$  in Fig. 2.9

The figure shows that higher slip ratio values, which are closer to the ideal  $\epsilon^*$ , decrease the friction coefficient at  $I$ . This is due to a reduction in the screw-roller sliding velocity when  $\epsilon$  increases. An opposite, but less pronounced tendency is observed for  $J$ , where very low  $\epsilon$  values mean that the rollers turn too slow, which leads to almost no spin at the nut-roller contact. Finally, friction coefficients decrease with viscosity and the Eyring stress, as expected.

Lubricant	$T$ ( $^{\circ}\text{C}$ )	$\alpha$ ( $\text{GPa}^{-1}$ )	$\eta_0$ (mPas)	$\tau_0$ (MPa)
traction fluid [47]	40	28.7	28.4	8
hot traction fluid [47]	100	16.5	4.6	8
5P4E [47]	40	35.0	266.0	8
grease B	-	30.0	166.5	8
grease C	-	30.0	166.5	10
SKF LGWA2	40	30.0	166.5	12

Table 2.2: Lubricant parameters used in Fig. 2.10. The Eyring stress  $\tau_0$  was chosen by the user.

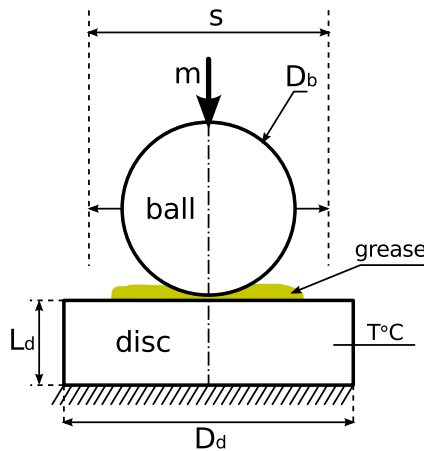
In conclusion, the numerical Jacod [47] model described earlier in this chapter appears to provide a reasonable method for calculating friction in the threaded contacts of a PRS mechanism, even when applied locally to a point inside the contact area. Based on the general formula proposed by Jacod et al. [47], the model can predict a friction coefficient for both sliding and spin. However, it assumes smooth surfaces and thermal effects are limited to a modification of the ambient viscosity and maybe  $\alpha$ . In the end, the fundamental problem of the Coulomb law remains unsolved, as one of the lubricant parameters (the Eyring stress  $\tau_0$ ) still has to be carefully chosen by the user.

Reference [47] used a limited range of  $\tau_0$  values (4, 6 and 8 MPa) to verify Eq. 2.26. As shown in Fig. 2.10, even the highest value (8 MPa) leads to relatively low friction coefficients for the most viscous lubricants. In reality, we would expect friction to be higher due to surface roughness, starvation and other phenomena, which is why  $\tau_0$  was increased for the greases used in table 2.2.

Nevertheless, the choice of a realistic Eyring stress value remains an open point. In chapter 3, we show that  $\tau_0 = 12$  MPa leads to numerical results which are close enough to experiments in terms of efficiency and dissipated power. Another option would be to measure the friction coefficient in conditions similar to the actual threaded contacts in a PRS. This possibility is investigated in the next section.

## 2.4 HFRR measurements

In this section, we measure the friction coefficient and relative film thickness using a classic HFRR rig in order to compare the behavior of two different greases commonly used in the roller screw industry and hopefully extract realistic values for  $\mu_a$  and  $\tau_0$  to use in the local numerical model described earlier.



ball diameter	$D_b$	6 mm
disc diameter	$D_d$	10 mm
disc thickness	$L_d$	3 mm
load mass	$m$	500 g
gravitational acceleration	$g$	$9.81 \text{ ms}^{-2}$
stroke length	$s$	1 mm
oscillation frequency	$f$	20 Hz
ball roughness	$R_a^b$	$< 0.05 \mu\text{m}$
disc roughness	$R_a^d$	$< 0.02 \mu\text{m}$
ball/disc materials: steel	$E'$	230.77 GPa

Figure 2.11: High frequency reciprocating rig (HFRR) diagram and characteristics

The experimental device is based on the contact between an oscillating ball and a fixed disc, as schematized in Fig. 2.11. The ball is fixed with a pressure screw (not shown) such that it

cannot roll on the disc surface; it only slides in the horizontal direction at a fixed frequency  $f$ . A load of 500 g ensures permanent contact.

The disc is heated to a temperature of 30°C and then measurement points are taken every second for 10 minutes. Afterwards, the device stops to allow the disc temperature a rise of 20°C. A new set of measurement points is taken in the next 10 minutes and the process is repeated up to a maximum of 110°C.

This device can measure the horizontal friction force on the ball and thus deduce the friction coefficient  $\mu$ . Using the electrical resistance between the two surfaces, it can also obtain a relative value of the average lubrication film thickness. These results are plotted in Fig. 2.12 for two greases commonly used in the roller screw industry.

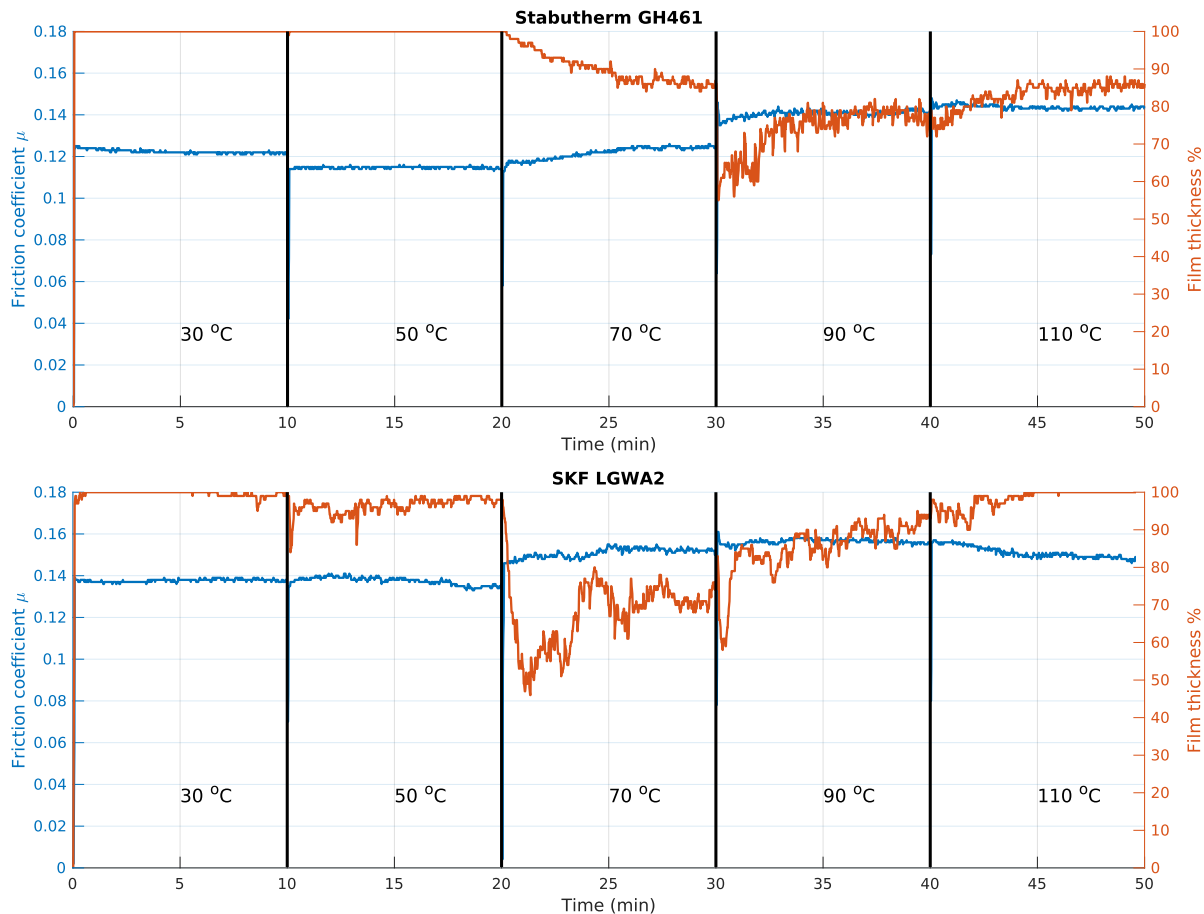


Figure 2.12: HFRR results for two common greases: Stabutherm GH461 and SKF LGWA2

As shown in the figure, friction coefficients are slightly lower for the first grease (Stabutherm GH461), although the stable  $\mu$  signals indicate good performance for both samples. There is a noticeable increase in terms of friction and a lubrication film drop at 90°C for the first grease and 70°C for the second. Therefore, the first grease seems to be better suited for the temperature range in which roller screws usually operate.

For both cases, the friction coefficient is roughly comprised between 0.11 and 0.16, which are higher than the values we obtained previously with the numerical contact model ( $\mu_a = 0.111$  for  $I$  and  $\mu_a = 0.083$  for  $J$ , see Fig. 2.9). The model used lubricant properties ( $\eta_0$ ,  $\alpha$ ) found in the product description of the second grease (SKF LGWA2), since for the first grease this information was unavailable.

In any case, some of the HFRR test conditions were not as close as we would have liked to real PRS contacts. For example, the dry Hertzian pressure which corresponds to the experimental device can be calculated as:

$$P_h^{HFRR} = \frac{3mg}{2\pi a_b^2} \quad \text{where } a_b = \sqrt[3]{\frac{3mgD_b}{4E'}} \quad (2.41)$$

which leads to a value of  $P_h^{HFRR} = 1.12$  GPa. This is only around half the pressure we would expect in actual roller screws. On the other hand, in order to obtain 2.5 GPa on the HFRR machine, we would need to use a mass load of roughly 5.5 kg, which was impossible given the rather small dimensions of the experimental device. It would be interesting to perform these friction coefficient measurements on a setup which can create higher contact pressures.

In terms of the sliding speed, a maximum value is obtained on the HFRR device when the ball passes by the central position of its oscillatory motion. For a sinusoidal speed signal imposed on the ball, this maximum value can be determined as:

$$v_{max}^{HFRR} = \frac{\pi}{2} v_{avg}^{HFRR} \quad \text{where } v_{avg}^{HFRR} = 2sf \quad \Rightarrow \quad v_{max}^{HFRR} = \pi sf = 62.8 \text{ mm/s} \quad (2.42)$$

which is consistent with the order of magnitude of sliding speeds commonly encountered in real PRS. In Fig. 2.8, for example, we had obtained 107 mm/s for the  $I$  contact, for a screw rotation speed of  $\omega_{s/n} = 400$  rpm.

In conclusion, the HFRR experiments allowed us to compare the performance of two greases and choose the better one based on a friction and film separation analysis (results might evolve with other criteria). Friction coefficients are comprised between 0.11 and 0.16, which are higher than what we had expected through the Jacod [47] lubrication model. This indicates that an Eyring stress value of minimum 12 MPa should be used in the numerical calculations. However, the measurement device did not allow ideal test conditions to be achieved, as the real threaded contacts in a PRS are characterized by higher pressures. The development of a better suited experimental procedure might be interesting for future research, but in the current work we chose the torque and efficiency measurements in Fig. 2.5 for calibrating the numerical models. This investigation is detailed in the next chapter.

## 2.5 Conclusion

The current chapter introduces an analytical kinematic model of the PRS centered around the amount of circumferential slip. This slip is quantified using a non-dimensional ratio  $\epsilon$  which can only take values in a specific interval. Since the ratio is difficult to control in practice, we treat it as an unknown which is measured. Experiments confirm that stationary values are very close to the theoretical ideal (the difference is less than 1%), which leaves little room for kinematic improvement.

The model works for both standard and inverted PRS and is able to express all the mechanism's stationary regime kinematics as a function of this slip ratio  $\epsilon$  and the input speed on the screw. Sliding velocity vectors at contact centers are calculated in order to determine the minimal and maximal allowed values for  $\epsilon$ . One of the two extremes corresponds to pure sliding, when the mechanism behaves like the usual friction screw, while the other represents the theoretical ideal  $\epsilon^*$  for which sliding velocity gets minimized.

Kinematic constraints are developed to show that the leads of the screw and the nut must always be identical, while previous research assumes this condition is only due to geometry. Furthermore, contact areas are discretized to calculate the local sliding velocity vector at any point contained inside. This information is used to show that roller-screw and roller-nut interfaces are very different in terms of kinematics: one of them is characterized by a motion of pure spin, while the other has a combination of spin and uniform sliding, where the latter is predominant.

Finally, these results are used in a numerical model to deduce local friction coefficients, which are very influential parameters in terms of the PRS efficiency and dissipated power. Classic grease lubrication tests are performed to verify the consistency of the obtained values and identify the best available lubricant.

## Chapter 3

# Dynamics and dissipated power

### 3.1 Introduction

The goal of the current chapter is to quantify the power dissipated in the PRS mechanism, which is an important result for any further study related to efficiency or temperature distribution. Furthermore, it can be used as a design criterion in choosing the optimal parameters for a given application. Based on the main hypotheses used throughout this memoir (rigid solids, parallel rollers, etc.), a numerical force model is developed, which computes the dissipated power at steady-state. The model determines the slip ratio reached during stationary equilibrium and uses the result to deduce all the kinematic and dynamic unknowns that were considered. A glimpse of this research has already been published by the authors in an article [14].

This subject has received limited attention in current literature. The mechanism efficiency and load capacity were first analyzed by Velinsky et al. [2], who used a simple Coulomb model, single-point contacts and only considered friction caused by rolling and sliding. Jones et al. [44] continued the research, integrating viscous friction and more realistic contact point locations. Spin torques were later modeled by Ma et al. [12, 32], who included other power dissipation sources as well.

The most complete numerical dynamic model to date was published by Fu et al. [28]. It works for both the transient and stationary regimes and considers the transversal movement of roller axes as well, such that normal contact forces on the threads follow a linear distribution. Five sources of friction are taken into account, including the planet carrier and gears. While this ambitious and rather complex model seems to provide consistent results, it lacks a pragmatic approach in terms of power dissipation. Friction coefficients are set to be higher for the roller-carrier contacts, in comparison with threaded contacts (0.1 versus 0.03 or 0.05). Furthermore, we believe that in reality, the carrier turns inside the nut with a higher radial play (0.5 mm versus 0.01 mm in the cited paper). In our view, these auxiliary friction sources should have a much lower impact and most of the dissipated power is expected to come from the threaded roller-screw and roller-nut contacts.

Moreover, the model in reference [28] was only developed for standard roller screws and no information on the shape of the threaded profiles is given. The present model was verified for both standard and inverted PRS and special attention is put on the influence of thread geometry and other design parameters on efficiency and the dissipated power. We consider a constant load distribution among threads, such that the rollers and screw axis remain parallel at all times.

### 3.2 Stationary equilibrium model

Most roller screws can be used in two ways: either to transform rotation into translation (actuator mode) or the other way around (generator mode). In this thesis, only the actuator mode is considered. A simplified dynamic diagram for both standard and inverted PRS in this case is shown in Fig. 3.1. It can be seen that standard PRS turn the input torque on the screw into a linear translation of the nut, while inverted PRS turn the nut rotation into screw translation.

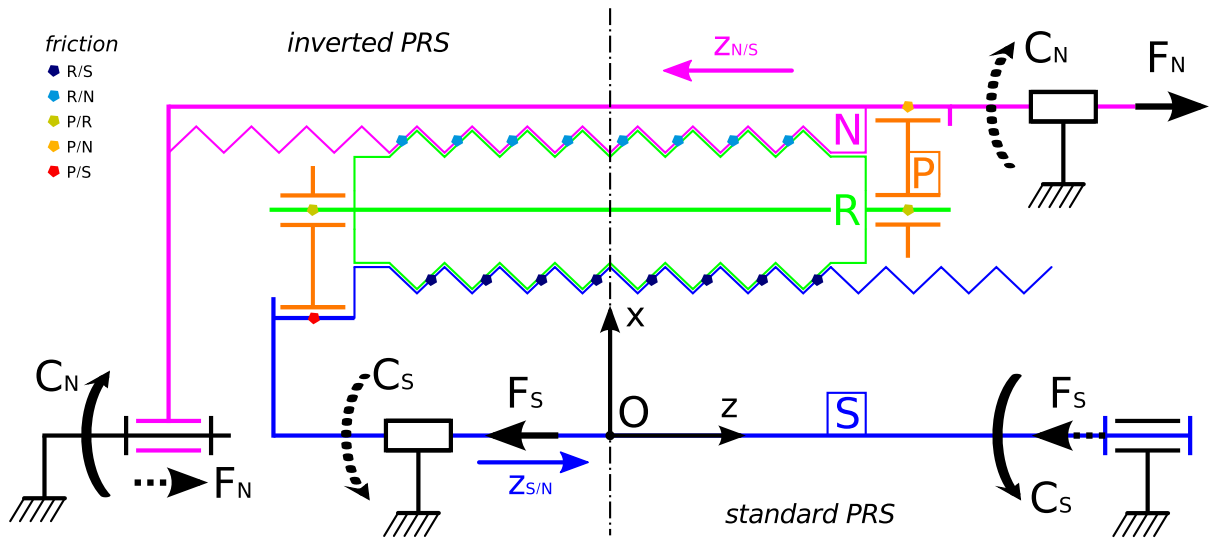


Figure 3.1: Dynamic diagram and friction sources for the standard and inverted PRS in actuator mode (rotation  $\rightarrow$  translation). Continuous lines for input forces and torques and dotted lines for link reactions.

This explains why the placement of pivot and slider links is different on the left and right sides of the figure.

The numerical dynamic model developed in this work assumes that a stationary regime has been reached, such that components turn or advance with constant velocities. In the previous chapter, we have shown that these steady-state speeds can be linked (see table 2.1), such that it becomes possible to deduce all the kinematic unknowns from only one degree of freedom, identified as the slip ratio  $\epsilon$ . We defined this ratio as the rotation speed of the planet carrier compared to the one of the screw and explained that its value is potentially influenced by lubrication conditions, loads, the input speed, etc. An experimental approach for measuring  $\epsilon$  was also presented. The dynamic model which will be described here proposes a way of calculating this slip ratio numerically using a relevant set of equilibrium equations. However, the model can also compute forces and powers for an imposed value of  $\epsilon$ , without taking these equations into account.

Let us first consider the case of a standard PRS, where an external motor applies a positive input torque  $C_S$  on the screw, making it turn at a constant speed  $\omega_{s/n}$  with respect to the nut. This will cause the nut assembly to translate in the negative  $z$  direction with a speed  $\dot{z}_{n/s}$  given by Eq. 2.5. Some amount of pushing load will accompany this movement, which means that a positive, reaction force  $F_N$  should also be applied by external means on the nut. For inverted PRS, a similar analysis can be performed with the input torque  $C_N$  on the nut and the input reaction force  $F_S$  on the screw.

Since the current work assumes all solids to be infinitely rigid, the input force gets entirely transmitted through the mechanism to the pivot links where the motor torque is applied, such that the link reaction is always its opposite:

$$F_S = -F_N \quad (3.1)$$

From now on, we will assume that the external force on the nut  $F_N$  is constant and imposed, just like the rotation speed of the screw. For both standard and inverted PRS, the signs of these two parameters have to be linked in order to correctly describe a mechanism in actuator mode:

$$F_N \cdot \omega_{s/n} > 0 \quad (3.2)$$

Figure 3.1 also places the five sources of friction which were considered. Apart from the main power losses through the roller-screw ( $R/S$ ) and roller-nut ( $R/N$ ) contacts, the model takes into account a few auxiliary sources related to the planet carrier, including friction with roller heads ( $P/R$ ), the screw ( $P/S$ ) and the nut ( $P/N$ ). For standard PRS, the  $P/S$  friction is nil, since

there is usually no contact between the two components (unless wipers are used [1]). The same is true for the  $P/N$  friction in the case of inverted roller screws.

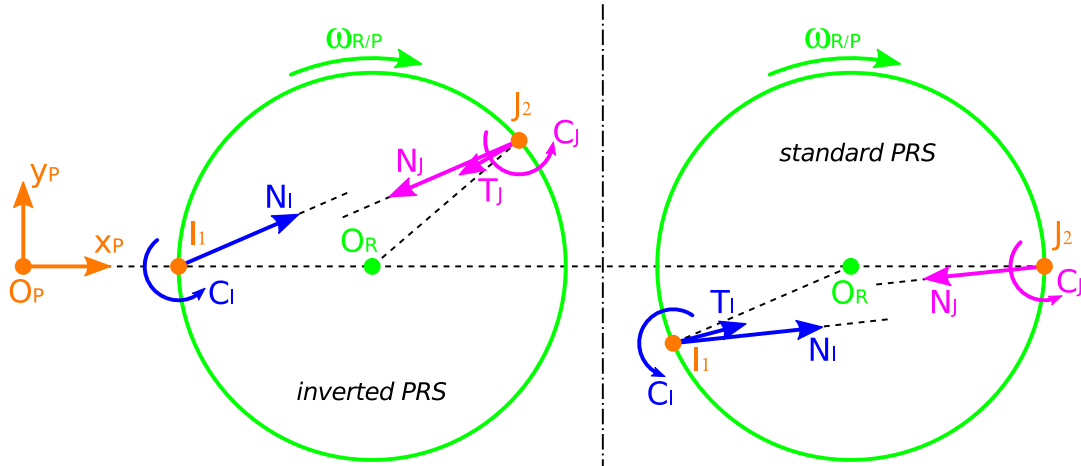


Figure 3.2: 2D view of the 3D contact forces and spin torques on the roller for the  $I_1J_2$  configuration.

We start the stationary dynamic analysis by studying the contact forces and torques on the roller for a single pair of  $I$  and  $J$  contacts. The common scenario for the  $I_1J_2$  configuration is represented in Fig. 3.2, which is a 2D view in the  $xy$  plane. Forces are 3D vectors, so we only see their radial/circumferential projection. For the torques, only the axial ( $z$ ) projection is represented.

The left side of the figure corresponds to inverted PRS and the right side to standard PRS. Depending on the type of roller screw studied, the contact points location varies accordingly. However, the position of only one of the points is shifted, while the other is almost always placed on the  $O_P O_R$  line. Exceptions can occur if component geometry is imposed<sup>1</sup>, but in all cases the shift of the second point is much smaller.

In the general case, there will always be a contact normal load and a smaller tangential force due to sliding friction. Usually, the *no sliding* condition occurs for one of the contacts, leading to a nil relative velocity at the center of the ellipse, as shown in Fig. 2.8. In this case, the resulting tangential force should also be nil. As for the friction caused by the spin motion, it can be modeled by a torque applied in the direction of the surface normal vector. If  $\vec{n}_I$  and  $\vec{n}_J$  denote these external unit vectors for the roller, it means that we can express the associated contact wrenches as:

$$\mathcal{F}_{S/R}(I) \begin{cases} T_I \vec{t}_I - N_I \vec{n}_I = -N_I \vec{m}_I \\ C_I \vec{n}_I \end{cases} \quad (3.3)$$

$$\mathcal{F}_{N/R}(J) \begin{cases} T_J \vec{t}_J - N_J \vec{n}_J = -N_J \vec{m}_J \\ C_J \vec{n}_J \end{cases} \quad (3.4)$$

A better understanding of the equilibrium model can be achieved if we introduce two friction coefficients  $\mu_I$  and  $\mu_J$  such that:

$$\begin{cases} T_I = \mu_I N_I \\ T_J = \mu_J N_J \end{cases} \Rightarrow \begin{cases} \vec{m}_I = \vec{n}_I - \mu_I \vec{t}_I \\ \vec{m}_J = \vec{n}_J - \mu_J \vec{t}_J \end{cases} \quad (3.5)$$

These coefficients are nil unless sliding friction is present, which modifies the direction of the normal contact load. They do not have the same meaning as the average coefficient  $\mu_a$  described by Eq. 2.40 and can therefore take other values. Also note that  $\vec{n}_{I,J}$  and  $\vec{t}_{I,J}$  are unit vectors, while the modified direction  $\vec{m}_{I,J}$  has a different module.

<sup>1</sup>see *simulation* list of parameters in table 1.3

### 3.2.1 Sliding friction

It would be interesting to compute  $\overrightarrow{m_{I,J}}$  in order to see how much of a difference the sliding friction makes. This requires the calculation of the tangential force vector. If the contact ellipse is discretized as shown in Fig. 2.7, we can define this vector as the sum of local contributions such that:

$$T_M \overrightarrow{t_M} = \sum \overrightarrow{T_D} \Rightarrow \mu_M N_M \overrightarrow{t_M} = \sum \mu_D P_D \frac{\overrightarrow{v_D}}{|\overrightarrow{v_D}|} ds \quad (3.6)$$

where point  $M$  is either  $I$  or  $J$  and  $P_D$  the local contact pressure on a small surface  $ds$  around  $D$  given by:

$$ds = \frac{4ab}{N_1 N_2} \quad (3.7)$$

The local friction coefficient  $\mu_D$  can be imposed by a simple Coulomb law or calculated with a lubrication model like the one given by Eq. 2.27. As for the local pressure  $P_D$ , it can be calculated according to the Hertzian dry contact model used in Eq. 2.28. Finally, since in the current work we neglect the normal component of the sliding velocity ( $\overrightarrow{v_D} \cdot \overrightarrow{n_M} \approx 0$ ), it follows that:

$$\overrightarrow{m_M} = \overrightarrow{n_M} - \frac{6}{\pi N_1 N_2} \sum \left( \mu_D \sqrt{1 - \left(\frac{t_{1D}}{a}\right)^2 - \left(\frac{t_{2D}}{b}\right)^2} \cdot \frac{(\overrightarrow{n_M} \times \overrightarrow{v_D}) \times \overrightarrow{n_M}}{\sqrt{(\overrightarrow{v_D} \cdot \overrightarrow{t_1})^2 + (\overrightarrow{v_D} \cdot \overrightarrow{t_2})^2}} \right) \quad (3.8)$$

where the local relative velocity  $\overrightarrow{v_D}$  can be determined with Eq. 2.22.

The numerical application of Eq. 3.8 yields results which are very close to the normal surface vector  $\overrightarrow{n_M}$ , which means that the tangential sliding friction force is usually much smaller than the normal contact load and therefore does not change its direction much. However, since purely normal contact forces do not dissipate power, the tangential sliding friction becomes important in estimating power losses. Later in this chapter, we show that it actually has the largest contribution, accounting for more than 90% of the total power lost.

### 3.2.2 Spin torques

The second largest source of power dissipation is usually caused by the axial projection of the contact spin torques  $C_I$  and  $C_J$  represented in Fig. 3.2. If point  $M$  denotes either  $I$  or  $J$ , these torques can be computed from local sliding friction moments as:

$$C_M \overrightarrow{n_M} = \sum \overrightarrow{M_D} \times \overrightarrow{T_D} \quad (3.9)$$

When using the same assumptions as before ( $\overrightarrow{v_D} \cdot \overrightarrow{n_M} \approx 0$  and  $ds$  given by Eq. 3.7), this eventually leads to:

$$C_M = \frac{6N_M}{\pi N_1 N_2} \sum \left( \mu_D \sqrt{1 - \left(\frac{t_{1D}}{a}\right)^2 - \left(\frac{t_{2D}}{b}\right)^2} \cdot \frac{(\overrightarrow{v_D} \cdot \overrightarrow{t_2})t_{1D} - (\overrightarrow{v_D} \cdot \overrightarrow{t_1})t_{2D}}{\sqrt{(\overrightarrow{v_D} \cdot \overrightarrow{t_1})^2 + (\overrightarrow{v_D} \cdot \overrightarrow{t_2})^2}} \right) \quad (3.10)$$

The numerical application of Eq. 3.10 shows that the axial projections of the contact spin torques at  $I$  and  $J$  always oppose the angular velocity of the roller, for both standard and inverted PRS. This confirms their dissipative nature. Also note that spin torques are caused by the presence of a contact area: if single point contacts are considered ( $N_1 = N_2 = 1$ ), they become nil. Discretization quality affects the results for low  $N_1$  and  $N_2$ , but we show later that convergence is achieved for sufficiently high values.

### 3.2.3 Normal loads

We have seen how both the tangential friction and the contact spin torque can be expressed as functions of the local sliding velocity field  $\vec{v}_D$ , the friction coefficient and the normal load. Here we propose a way of determining this load from the total external force on the nut  $F_N$ , which is supposed to be constant and imposed in the stationary regime.

In the current work, we assume that all rollers are parallel and identical, such that  $F_N$  gets equally distributed among all roller-nut contacts. If we write Newton's second law to describe the axial  $z$  force equilibrium of the nut in Fig. 3.1, it leads to:

$$\frac{F_N}{N_R N_C} + N_J \vec{m}_J \cdot \vec{z} = 0 \quad \Leftrightarrow \quad N_J = -\frac{F_N}{N_R N_C \vec{m}_J \cdot \vec{z}} \quad (3.11)$$

where  $N_R$  represents the number of rollers and  $N_C$  the number of roller-nut (or roller-screw) contacts per roller. Figure 3.1 was drawn for  $N_C = 8$  to privilege clarity, although real values are usually higher. The modified direction  $\vec{m}_J$  was used in order to include the axial projection of sliding friction, even though its contribution is usually small.

In a similar way, we can write the  $z$  force equilibrium of the roller to deduce that:

$$-N_I \vec{m}_I \cdot \vec{z} - N_J \vec{m}_J \cdot \vec{z} = 0 \quad \Leftrightarrow \quad N_I = \frac{F_N}{N_R N_C \vec{m}_I \cdot \vec{z}} \quad (3.12)$$

Once the normal contact loads are known, it becomes possible to determine the total external torques  $C_S$  and  $C_N$  on the screw and nut, respectively. With the assumptions made so far, there is no reason for these torques to have the same modulus; this is only true for the external axial forces  $F_S$  and  $F_N$  (see Eq. 3.1). Instead, the torques should be deduced from the  $z$  moment equilibrium equations of the screw and nut:

$$C_S + C_{P/S} + N_R N_C \left( \vec{OI} \times N_I \vec{m}_I - C_I \vec{n}_I \right) \cdot \vec{z} = 0 \quad (3.13)$$

$$C_N + C_{P/N} + N_R N_C \left( \vec{OJ} \times N_J \vec{m}_J - C_J \vec{n}_J \right) \cdot \vec{z} = 0 \quad (3.14)$$

where point  $O$  is situated on the screw (and nut) axis of rotation and  $C_{P/S}$  and  $C_{P/N}$  are possible friction torques exerted by the planet carrier, as shown in Fig. 3.1. When using the contact points location described in Fig. 1.7, it leads to the following results:

$$C_S = N_R N_C \left( C_I \vec{n}_I \cdot \vec{z} - N_I r_{IS} \begin{pmatrix} -\sin \theta_{IS} \\ \cos \theta_{IS} \\ 0 \end{pmatrix} \cdot \vec{m}_I \right) - C_{P/S} \quad (3.15)$$

$$C_N = N_R N_C \left( C_J \vec{n}_J \cdot \vec{z} - N_J r_{JN} \begin{pmatrix} -\sin \theta_{JN} \\ \cos \theta_{JN} \\ 0 \end{pmatrix} \cdot \vec{m}_J \right) - C_{P/N} \quad (3.16)$$

### 3.2.4 Static equilibrium

Let us now investigate the simplest scenario, where the PRS mechanism is axially loaded ( $F_N \neq 0$ ), but none of the components move ( $\omega_{s/n} = 0$ ). In this case, the local sliding velocity fields will be nil, which means that  $\vec{m}_M = \vec{n}_M$  according to Eq. 3.8. There is no spin and contact wrenches are reduced to the sole presence of normal loads.

We already know that the axial  $z$  force equilibrium of the nut and rollers is satisfied, since that is how normal loads are deduced (see Eqs. 3.11 – 3.12). The same can be said about the screw, due to the obtained results and Eq. 3.1. We would like to discuss equilibrium in terms of other degrees of freedom.

If we suppose that the planet carrier does not cause any friction in the static case, it means that the external  $z$  torques on the screw and nut can be expressed as:

$$C_S^0 = F_N r_{IS} \frac{\vec{n}_I \cdot \begin{bmatrix} \sin \theta_{IS} \\ -\cos \theta_{IS} \\ 0 \end{bmatrix}}{\vec{n}_I \cdot \vec{z}} \quad C_N^0 = -F_N r_{JN} \frac{\vec{n}_J \cdot \begin{bmatrix} \sin \theta_{JN} \\ -\cos \theta_{JN} \\ 0 \end{bmatrix}}{\vec{n}_J \cdot \vec{z}} \quad (3.17)$$

Some of the geometrical properties of the contact normal vectors detailed in Eq. 2.13 allow a very interesting simplification of these results:

$$C_S^0 = \frac{F_N l_s}{2\pi} \quad C_N^0 = -\frac{F_N l_n}{2\pi} \quad (3.18)$$

which means that the external torques on the screw and nut take identical, but opposite values. Moreover, these values are not nil, which means that in the static case, the motor has to apply the corresponding torque to prevent the system from moving.

The  $z$  moment equilibrium of the screw and nut were guaranteed by Eqs. 3.15 – 3.16. However, the condition is also true for the rollers, since in this case the only contributions to their axial torque is due to normal loads, which lead to moments of equal modulus and opposite signs in view of the geometrical properties given in Eq. 2.13.

The  $x$  and  $y$  torque equilibrium equations are not discussed in the current memoir, because the corresponding rotations are supposed to be forbidden for all PRS components. The screw, nut and all the roller axes are assumed to be parallel at all times. Therefore, the only remaining equations to be checked describe radial  $x$  and circumferential  $y$  forces.

For the screw and nut, these two equations will always be verified due to the symmetric distribution of identical rollers. In statics, the resulting  $y$  contact force on a roller would be written as:

$$\vec{F}_{c/R} \cdot \vec{y} = -N_I \vec{n}_I \cdot \vec{y} - N_J \vec{n}_J \cdot \vec{y} = \frac{F_N}{N_R N_C} \left( -\frac{\vec{n}_I \cdot \vec{y}}{\vec{n}_I \cdot \vec{z}} + \frac{\vec{n}_J \cdot \vec{y}}{\vec{n}_J \cdot \vec{z}} \right) = \frac{-F_N (n_{Iy} + n_{Jy})}{N_R N_C \gamma_I} \quad (3.19)$$

On the other hand, Eqs. 2.9 – 2.13 can be combined to deduce a much simpler expression for  $n_{Iy}$ :

$$\begin{bmatrix} \sin \theta_{IS} & -\cos \theta_{IS} \\ \sin \theta_{IR} & -\cos \theta_{IR} \end{bmatrix} \cdot \begin{bmatrix} n_{Ix} \\ n_{Iy} \end{bmatrix} = \frac{\gamma_I}{2\pi} \begin{bmatrix} l_s/r_{IS} \\ l_r/r_{IR} \end{bmatrix} \quad (3.20)$$

$$\begin{bmatrix} n_{Ix} \\ n_{Iy} \end{bmatrix} = \frac{\gamma_I}{2\pi r_{IS} r_{IR} (\sin \theta_{IR} \cos \theta_{IS} - \sin \theta_{IS} \cos \theta_{IR})} \begin{bmatrix} -\cos \theta_{IR} & \cos \theta_{IS} \\ -\sin \theta_{IR} & \sin \theta_{IS} \end{bmatrix} \cdot \begin{bmatrix} l_s r_{IR} \\ l_r r_{IS} \end{bmatrix} \quad (3.21)$$

$$n_{Iy} = \frac{\gamma_I (l_r - l_s) r_{IS} \sin \theta_{IS}}{2\pi r_{IS} \sin \theta_{IS} (r_{IS} \cos \theta_{IS} - r_{IR} \cos \theta_{IR})} = \frac{\gamma_I (l_r - l_s)}{2\pi c} \quad (3.22)$$

The same can be done with  $n_{Jy}$  to obtain that:

$$n_{Iy} + n_{Jy} = \frac{\gamma_I (l_r - l_s)}{2\pi c} + \frac{\gamma_J (l_r - l_n)}{2\pi c} = 0 \quad \Rightarrow \quad \vec{F}_{c/R} \cdot \vec{y} = 0 \quad (3.23)$$

which means that the  $y$  force equilibrium on the roller is also satisfied in the static case, when only normal loads are present. We showed that this is due to several geometric properties relating normal surface vectors and the location of the contact points.

Finally, we have to check the  $x$  force equation on the roller. The corresponding total load is written as:

$$\vec{F}_{c/R} \cdot \vec{x} = -N_I \vec{n}_I \cdot \vec{x} - N_J \vec{n}_J \cdot \vec{x} = \frac{-F_N (n_{Ix} + n_{Jx})}{N_R N_C \gamma_I} \neq 0 \quad (3.24)$$

Unfortunately, numerical results confirmed that this force is not nil like in the previous case for  $y$ . This means that even in the simplest scenario which corresponds to statics and purely normal contact forces, it is impossible to satisfy all the equilibrium equations with the stationary model presented so far (screw + nut + rollers). However, the problem can be solved by including the equilibrium of the other PRS components, like the planet carrier. In the static case, we could imagine that a positive resulting contact force in  $x$  would push the rollers towards the outside until their heads touch the cylindrical wall of the carrier, as shown in Fig. 3.3 for a standard PRS. At that point, an additional load on the rollers coming from the planet carrier would appear; this load would make sure that every roller  $x$  force equilibrium is satisfied. Due to the symmetric distribution of rollers, the carrier would also be in equilibrium.

### 3.2.5 Auxiliary contributions

In the previous section, we showed that static equilibrium could be ensured if radial  $x$  forces on the planet carrier were taken into account. The dynamic stationary model presented in this memoir includes resistive torques on the carrier caused by possible friction with the screw or nut. Therefore, we should also include an active component, which makes the carrier turn and guarantees its constant rotation speed. This component can only exist in the form of a circumferential  $y$  force exerted by the roller heads.

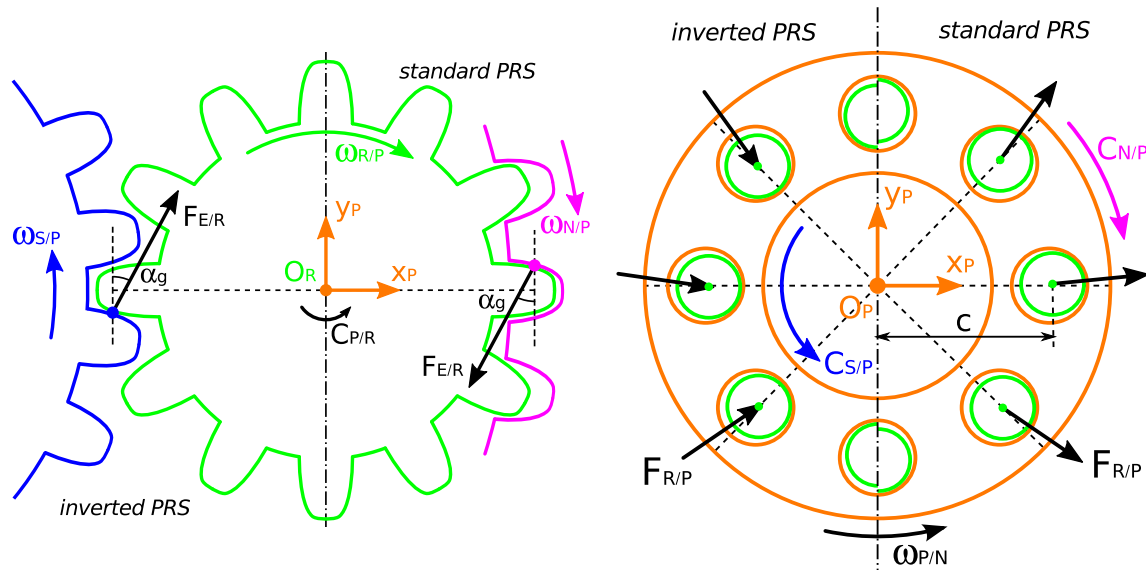


Figure 3.3: Auxiliary forces and torques on the roller and the planet carrier

The right side of Fig. 3.3 depicts the typical scenario which occurs for standard and inverted PRS. In both cases,  $c$  represents the radial distance between the screw/nut/carrier and roller axes during the stationary regime, such that the contact points location is calculated accordingly. The cylindrical holes machined in the planet carrier are usually larger than the roller heads and ensure a relatively large amount of radial play (around 0.2 mm). Nevertheless, the model should include an auxiliary friction torque at this level. This torque will be called  $C_{P/R}$  and will quantify the friction exerted by the carrier on both roller heads (see Fig. 3.1).

The  $z$  moment equilibrium equation for the planet carrier can then be written as:

$$N_R c \overrightarrow{F_{R/P}} \cdot \overrightarrow{y} - C_{P/S} - C_{P/N} - N_R C_{P/R} = 0 \quad (3.25)$$

which allows us to compute the active force required by a roller to move the carrier:

$$\overrightarrow{F_{R/P}} \cdot \overrightarrow{y} = \frac{N_R C_{P/R} + C_{P/N} + C_{P/S}}{c N_R} \quad (3.26)$$

This circumferential force should produce an active torque which has the same sign as  $\omega_{p/n}$ . The friction moment  $C_{N/P}$ , which usually exists for standard PRS only, opposes this movement. On the other hand, the screw always turns faster than the carrier, which means that the screw friction torque  $C_{S/P}$  and  $\omega_{p/n}$  should have the same direction for both the standard and inverted cases. This explains the way arrows were drawn in Fig. 3.3.

Numerical results show that the radial force contributions  $\overrightarrow{F_{R/P}} \cdot \overrightarrow{x}$  are much higher than their circumferential counterparts given by Eq. 3.26. This means that rollers tend to be pushed towards the outside for a standard PRS and inwards for the inverted type. However, there is no reason for these forces to be equal to the combined (screw + nut) contact loads on the roller. As detailed in Eq. 3.24, this is only true in the static case. For the stationary regime, the resulting contact force disequilibrium gets balanced by the combined effect of the planet carrier and the gears, as shown in Fig. 3.3.

In the general case, we can write the resulting disequilibrium force per  $I$  and  $J$  contact pair as:

$$\overrightarrow{F_{c/R}} = -N_I \overrightarrow{m_I} - N_J \overrightarrow{m_J} \quad (3.27)$$

When also taking gears and the planet carrier into account, the roller  $y$  force equilibrium equation is written as:

$$N_C \overrightarrow{F_{c/R}} \cdot \overrightarrow{y} + \overrightarrow{F_{E/R}} \cdot \overrightarrow{y} - \overrightarrow{F_{R/P}} \cdot \overrightarrow{y} = 0 \quad \Rightarrow \quad \overrightarrow{F_{E/R}} \cdot \overrightarrow{y} = \overrightarrow{F_{R/P}} \cdot \overrightarrow{y} - N_C \overrightarrow{F_{c/R}} \cdot \overrightarrow{y} \quad (3.28)$$

which in combination with Eq. 3.26 allows us to compute the circumferential component of the gears' action on the roller. If we consider that steady state is characterized by only one pair of intermeshed teeth, such that  $\overrightarrow{F_{E/R}}$  is aligned with the gear line of action as shown on the left side of Fig. 3.3, the radial  $x$  component can then also be deduced using a simple geometrical formula:

$$\overrightarrow{F_{E/R}} \cdot \overrightarrow{x} = (1 - 2\chi) |\overrightarrow{F_{E/R}} \cdot \overrightarrow{y}| \tan \alpha_g \quad (3.29)$$

where  $\alpha_g$  is the gear pressure angle (usually  $20^\circ$ ) and  $\chi$  a boolean variable equal to 1 for standard roller screws and 0 for the inverted type. Note that the sign of the  $x$  component only depends on the PRS type, while the sign of the  $y$  component is a function of contact loads and friction. Figure 3.3 depicts the typical scenario where  $C_{P/N}$  and  $C_{P/S}$  are negligible. We can see that in this case, gears help the roller turn by producing an active  $z$  torque, which has the same sign as  $\omega_{r/p}$ .

The gear parts for the screw or nut are machined separately, then fixed to the threaded components. Due to the symmetric distribution of rollers,  $\overrightarrow{F_{E/R}}$  does not need to be retaken into account in the screw or nut force equilibrium equations. Furthermore, considering the geometry represented in Fig. 3.3, we can usually neglect the  $z$  torque produced by  $\overrightarrow{F_{E/R}} \cdot \overrightarrow{x}$ , since its moment arm is small (around half the tooth thickness). However, the circumferential gear force component creates a non-negligible torque which should be added to Eqs. 3.15 – 3.16 to obtain:

$$C_S = N_R N_C \left( C_I \overrightarrow{n_I} \cdot \overrightarrow{z} - N_I r_{IS} \begin{pmatrix} -\sin \theta_{IS} \\ \cos \theta_{IS} \\ 0 \end{pmatrix} \cdot \overrightarrow{m_I} \right) - C_{P/S} + (1 - \chi) N_R (c - r_R) \overrightarrow{F_{E/R}} \cdot \overrightarrow{y} \quad (3.30)$$

$$C_N = N_R N_C \left( C_J \overrightarrow{n_J} \cdot \overrightarrow{z} - N_J r_{JN} \begin{pmatrix} -\sin \theta_{JN} \\ \cos \theta_{JN} \\ 0 \end{pmatrix} \cdot \overrightarrow{m_J} \right) - C_{P/N} + \chi N_R (c + r_R) \overrightarrow{F_{E/R}} \cdot \overrightarrow{y} \quad (3.31)$$

where  $r_R$  is the nominal radius of the roller, where the gear contact is supposed to take place.

Finally, once  $\overrightarrow{F_{E/R}}$  is known, we can write the roller equilibrium in terms of radial  $x$  forces to deduce  $\overrightarrow{F_{R/P}} \cdot \overrightarrow{x}$ :

$$N_C \overrightarrow{F_{c/R}} \cdot \overrightarrow{x} + \overrightarrow{F_{E/R}} \cdot \overrightarrow{x} - \overrightarrow{F_{R/P}} \cdot \overrightarrow{x} + F_{cf} = 0 \quad \Rightarrow \quad \overrightarrow{F_{R/P}} \cdot \overrightarrow{x} = \overrightarrow{F_{E/R}} \cdot \overrightarrow{x} + N_C \overrightarrow{F_{c/R}} \cdot \overrightarrow{x} + F_{cf} \quad (3.32)$$

In the previous expression,  $F_{cf}$  quantifies a possible contribution of the centrifugal force, which tends to push the rollers outwards at high speeds:

$$F_{cf} = m_R c \omega_{p/n}^2 \quad (3.33)$$

where  $m_R$  represents the mass of a roller. Unless the carrier rotation speed is high ( $> 500$  rpm) and the studied PRS is very large and heavy ( $m_R \approx 1$  kg), the effect of this force is usually negligible in comparison to the other contributions.

In conclusion, the  $x$  and  $y$  auxiliary forces caused by gears and the planet carrier can be determined from the resulting contact disequilibrium on the roller  $\overrightarrow{F_{c/R}}$  and the auxiliary friction torques  $C_{P/S}$ ,  $C_{P/N}$  and  $C_{P/R}$ . These torques can be imposed or calculated with a small model.

In the context of the current work,  $C_{P/S}$  and  $C_{P/N}$  are directly specified by the user and usually assumed to be nil due to the large radial play available to the planet carrier (around 0.5 mm), as well as the geometry of the retaining rings which make the  $P/S$  and  $P/N$  contacts possible. The implementation of a dedicated model was only investigated for  $C_{P/R}$ .

As suggested in Fig. 3.3, the cylindrical contacts between roller heads and the corresponding holes in the planet carrier could be treated as plain journal bearings. The friction torque  $C_{P/R}$  can then be obtained from many formulas available in current literature.

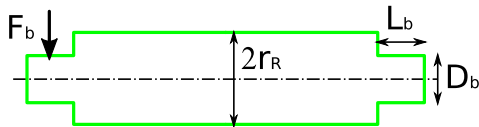


Figure 3.4: Simplified roller geometry such that  $L_b \approx D_b \approx r_R$

In practice [1], roller heads are commonly machined such that their length and diameter take close values, as shown in Fig. 3.4. For finite length bearings and a  $L_b/D_b$  ratio of 1, the non-dimensional friction torque  $\overline{C}_a$  can be found in tables [48, p. 140] as a function of the Sommerfeld number  $S$  defined by:

$$S = \frac{\eta_0 L_b D_b^3 |\omega_{r/p}|}{4e_b^2 F_b} \quad (3.34)$$

where  $\omega_{r/p}$  is the rotation speed of the roller inside the planet carrier and  $e_b$  is the maximum allowed eccentricity or half the radial play. In the current work,  $e_b = 0.1$  mm is a common value. We assume that the bearing uses the same lubricant as the threaded contacts and that its viscosity  $\eta_0$  is the one measured at ambient pressure. Finally, the load  $F_b$  per roller head should be calculated from:

$$F_b = \frac{1}{2} \sqrt{(\overrightarrow{F_{R/P}} \cdot \vec{x})^2 + (\overrightarrow{F_{R/P}} \cdot \vec{y})^2} \quad (3.35)$$

However, this approach becomes an iterative problem, since we already need  $C_{P/R}$  to calculate  $\overrightarrow{F_{R/P}}$ , according to Eq. 3.26. We can get around this by assuming that  $\overrightarrow{F_{R/P}} \cdot \vec{y}$  is much lower than  $\overrightarrow{F_{R/P}} \cdot \vec{x}$ , such that  $F_b$  is mostly caused by the resulting contact disequilibrium in the radial  $x$  direction. This assumption was confirmed by numerical results. From Eq. 3.28, 3.29 and 3.32, it leads to:

$$F_b \approx \frac{1}{2} N_C \left| \overrightarrow{F_{c/R}} \cdot \vec{x} + (1 - 2\chi) |\overrightarrow{F_{c/R}} \cdot \vec{y}| \tan \alpha_g + \frac{F_{cf}}{N_C} \right| \approx \frac{1}{2} N_C |\overrightarrow{F_{c/R}} \cdot \vec{x}| \quad (3.36)$$

In the end, the global torque  $C_{P/R}$  for the entire roller can be computed as:

$$C_{P/R} = 2 \operatorname{sgn}(\omega_{s/n}) \overline{C}_a S e_b F_b \quad (3.37)$$

where the sign function was added to make sure that it always opposes the roller movement.

### 3.2.6 Dynamic equilibrium

In the previous sections, we saw that the static equilibrium of the idealized PRS mechanism studied in this work can be achieved by including radial forces between roller heads and the planet carrier. The stationary, dynamic case also requires gears to be taken into account in order to satisfy the equilibrium equations. We now investigate if all of these equations have been considered for the available degrees of freedom.

Table 3.1 summarizes the kinematic and dynamic unknowns and equations used in the current model. Since the  $x$  and  $y$  rotations which correspond to transversal movements are not studied because the  $R$ ,  $S$ ,  $N$  and  $P$  axes are assumed to be parallel, we can see that all the other

		Unknowns		Equations						
Kinematic		$S/N$ rotation speed	$\omega_{s/n}$	4	imposed input speed	$\omega_{s/n}$	3			
		$R$ rotation ratio	$\lambda$			perfect gear condition		Eq. 2.4 for $\lambda$		
		slip ratio	$\epsilon$			stable displacement		Eq. 2.5 for $\dot{z}_{n/s}$		
		lead speed	$\dot{z}_{n/s}$							
Dynamic	external	$N$ actions	$F_N, C_N$	4	imposed force on the nut	$F_N$	2			
		$S$ actions	$F_S, C_S$			gear line of action		Eq. 3.29		
	contact	normal loads	$N_I, N_J$	6	models	sliding friction	Eq. 3.8 for $I$ and $J$	7		
		modified normals	$\vec{m}_I, \vec{m}_J$			spin torques	Eq. 3.10 for $I$ and $J$			
		spin torques	$C_I, C_J$			imposed by user	$C_{P/N}, C_{P/S}$			
	journal bearing					Eq. 3.37 for $C_{P/R}$				
	auxiliary	$P/R$ friction torque	$C_{P/R}$	7	equilibrium	$P$	$S$	$N$	$R$	9
		$P/N$ friction torque	$C_{P/N}$			$F_x$	symmetric distribution		Eq. 3.32	
		$P/S$ friction torque	$C_{P/S}$			$F_y$	of rollers		Eq. 3.28	
		$R/P$ $x, y$ force	$\vec{F}_{R/P}$			$F_z$	0	Eq. 3.1	Eq. 3.11	
gear $x, y$ force		$\vec{F}_{E/R}$	$C_x$			not available				
			$C_y$			in this model				
		$C_z$	Eq. 3.26	Eq. 3.30	Eq. 3.31	Eq. 3.43				
			21					21		

Table 3.1: Stationary dynamic model summary

equilibrium equations have already been written and considered, except for the  $z$  moment on the roller. In our view, this last equation should help us calculate a numerical value for the slip ratio  $\epsilon$ , which would otherwise remain unknown. This makes sense because friction and external actions should have an influence on the mechanism kinematics, as explained in chapter 2.

Of course, it remains possible for the user to impose the value of  $\epsilon$ , based on measurements for example. This allows all the kinematic and dynamic unknowns to be determined and satisfies the equilibrium equations written so far, but does not guarantee a nil  $z$  moment on the roller. However, we could imagine an iterative process which eventually gets close enough. This would allow us to obtain the numerical value of  $\epsilon$  reached during stationary equilibrium. The flowchart for such an algorithm is presented in Fig. 3.5.

As shown in the figure, the model first computes the normal contact loads and external torques in the static case. The  $I$  and  $J$  contact ellipse sizes can therefore be determined and we can geometrically discretize these areas. Afterwards, we have to choose a reasonable value for  $\epsilon$ , situated in the interval allowed by the PRS type and the ideal slip ratio  $\epsilon^*$  given in Eqs. 2.16 – 2.17. It was explained in chapter 2 that once  $\epsilon$  and the input speed  $\omega_{s/n}$  are known, any other kinematic unknown can be determined. We can thus compute local sliding velocity fields and deduce the friction coefficient  $\mu_D$  according to a lubrication model like the one given in Eq. 2.27. Alternatively, a simple Coulomb model could be used instead.

This allows us to quantify sliding friction through the modified directions  $\vec{m}_I$  and  $\vec{m}_J$ . Equations 3.12 – 3.11 are then applied in order to obtain normal loads which satisfy the new equilibrium. Spin torques can then also be deduced, as well as the auxiliary forces due to gears and the planet carrier. Finally, all of these actions cause a certain amount of  $z$  torque on the roller and we have to check that the sum of individual contributions is nil. Most of the time, this will not be the case, but the sign of the total residue can help us choose a more suitable value for  $\epsilon$  and repeat the process, until we get close enough to zero (dichotomy method). If measurements were performed and we already know  $\epsilon$  precisely, then the algorithm stops after the first iteration, ignoring the residue. In the end, Eqs. 3.30 – 3.31 allow us to compute the stationary external torques on the screw and nut and proceed to power dissipation and efficiency calculations.

Note that contact areas are calculated and discretized using static normal loads. All the geometry remains constant during the dichotomy loop, although normal contact loads change at every iteration. This choice simplifies the algorithm and improves its performance: the equilibrium value of  $\epsilon$  is obtained almost instantly on a modern desktop computer. It is justified by the fact that sliding friction is usually much smaller than  $N_I$  and  $N_J$ , such that dynamic

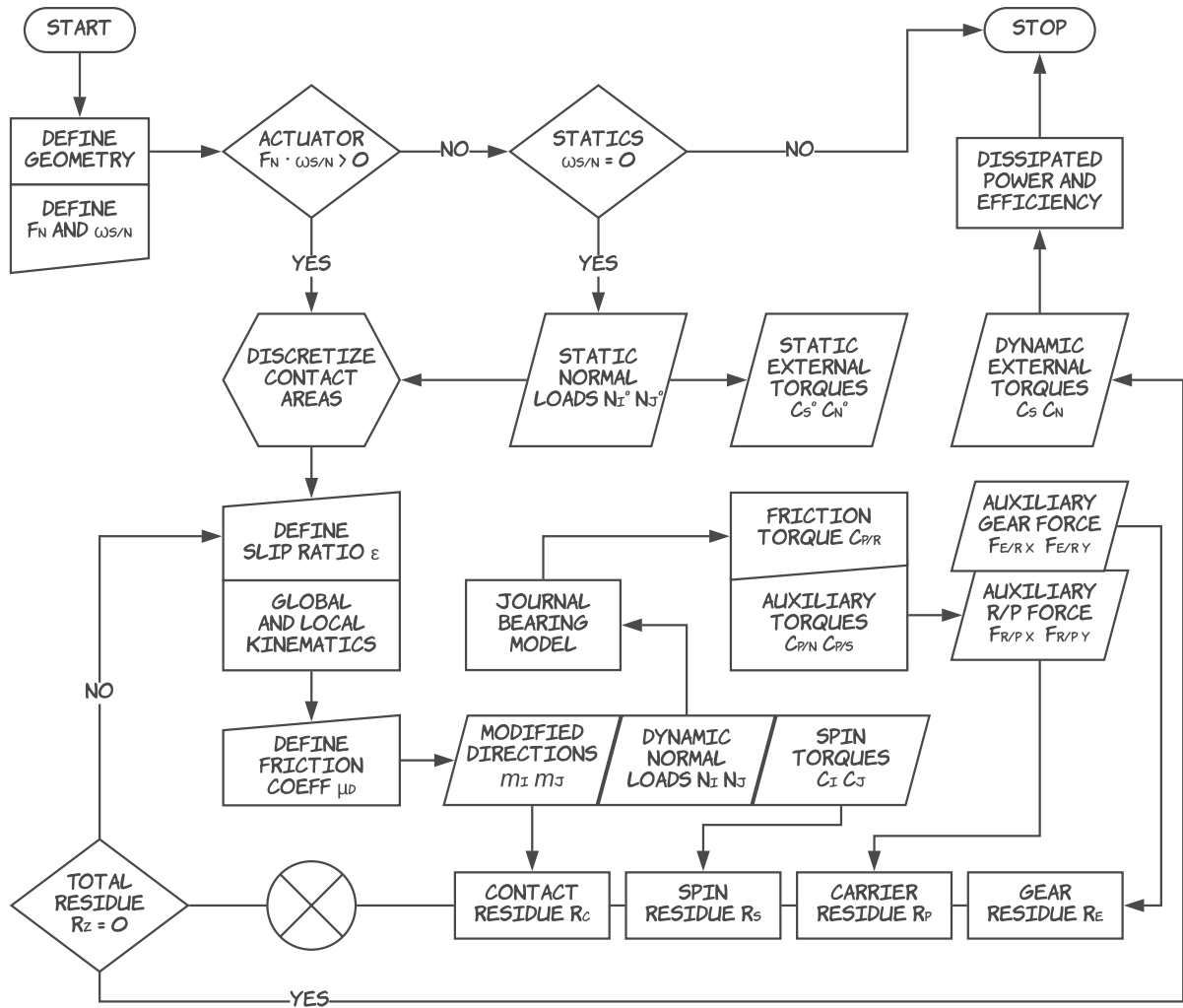


Figure 3.5: Stationary dynamic model flowchart. Trapezoid = process where user input is allowed or required, parallelogram = computed data,  $\otimes$  = sum, hexagon = loop preparation.

normal loads only increase slightly in comparison with the static case. For the sake of precision, it is possible to recalculate the size of contact areas during the loop, using the computed dynamic loads. However, the effect of this change on the dissipated power is negligible.

Let us now investigate the  $z$  moment equilibrium equation on the roller more closely. In the stationary dynamic case, it can be written as:

$$N_C \left( C_I \vec{n}_I + C_J \vec{n}_J - \overline{O_R I} \times N_I \vec{m}_I - \overline{O_R J} \times N_J \vec{m}_J \right) \cdot \vec{z} + C_{P/R} + (2\chi - 1)r_R \overline{F_{E/R}} \cdot \vec{y} = 0 \quad (3.38)$$

We then use Eqs. 3.11 – 3.12 and multiply everything by  $N_R/c|F_N|$  to obtain a non-dimensional total residue  $R_z$  as the sum of individual contributions due to contact forces (dynamic normal loads + sliding friction), spin torques, gears and the planet carrier:

$$R_c = \left( \frac{r_{IR}}{c} \cdot \frac{\vec{m}_I \cdot \begin{pmatrix} \sin \theta_{IR} \\ -\cos \theta_{IR} \\ 0 \end{pmatrix}}{\vec{m}_I \cdot \vec{z}} - \frac{r_{JR}}{c} \cdot \frac{\vec{m}_J \cdot \begin{pmatrix} \sin \theta_{JR} \\ -\cos \theta_{JR} \\ 0 \end{pmatrix}}{\vec{m}_J \cdot \vec{z}} \right) \text{sgn}(F_N) \quad (3.39)$$

$$R_s = \frac{(C_I \vec{n}_I \cdot \vec{z} + C_J \vec{n}_J \cdot \vec{z}) \frac{N_R N_C}{c|F_N|}}{\quad} \quad (3.40)$$

$$R_p = \frac{N_R C_{P/R}}{c|F_N|} \quad (3.41)$$

$$R_e = (2\chi - 1) \frac{r_R N_R \vec{F}_{E/R} \cdot \vec{y}}{c|F_N|} \quad (3.42)$$

---


$$R_z = 0 \quad (3.43)$$

This residue quantifies the resulting  $z$  torque on the roller and should be nil when stationary equilibrium is reached. According to the dichotomy (bisection) method, if  $[\epsilon_1, \epsilon_2]$  (where  $\epsilon_1 < \epsilon_2$ ) represents the initial interval where the slip ratio  $\epsilon$  is defined, the sign of the total residue  $R_z$  should help us choose better limits at every iteration and narrow down the interval until it virtually becomes a single point. In practice, we use the interval size to stop the iterative process when sufficient precision is reached:

$$\text{initial} \begin{cases} \epsilon_1 = (1 - \chi)\epsilon^* \\ \epsilon_2 = (1 - \chi) + \chi\epsilon^* \end{cases} \quad (3.44)$$

$$\text{then } \epsilon = \frac{\epsilon_1 + \epsilon_2}{2} \Rightarrow \begin{cases} \epsilon_1 = \epsilon & \text{if } (2\chi - 1) \text{sgn}(\omega_{s/n})R_z < 0 \\ \epsilon_2 = \epsilon & \text{otherwise} \end{cases} \quad \text{until } \epsilon_2 - \epsilon_1 < 1e - 10 \quad (3.45)$$

The fact that we can use  $R_z$  to modify  $\epsilon$  like this can be explained by the following example: on a standard PRS ( $\chi = 1$ ) which turns counterclockwise ( $\omega_{s/n} > 0$ , like drawn in Fig. 3.1), a negative  $z$  torque residue helps the rollers turn. If this torque became nil, rollers would have to turn more and the amount of slip would decrease. Therefore,  $\epsilon$  should increase to reach stationary equilibrium, which is why the lower limit of the  $[\epsilon_1, \epsilon_2]$  interval is set to be higher. We can generalize this reasoning for inverted PRS ( $\chi = 0$ ) through the equations written above.

One could argue that it only works if  $R_z$  is a strictly monotonous function of  $\epsilon$  which changes signs over the initial  $[\epsilon_1, \epsilon_2]$  interval, such that the  $\epsilon$  solution which corresponds to  $R_z = 0$  is unique. Figure 3.6 in the next section shows that it is indeed the case, for both standard and inverted PRS.

### 3.2.7 Algorithm convergence

In order to illustrate the convergence of the proposed model, we use a typical set of input parameters, detailed in table 3.2. In view of the hypotheses and equations used in the current work, this list compiles a minimum number of inputs required to fully define the mechanism geometry, steady-state kinematics and force balance unknowns. It was chosen to match as much as possible experiment #6 on the standard roller screw described in Fig. 2.4. This way, numerical results can be compared to some of the performed measurements.

The PRS geometry is defined using the *design* method detailed in table 1.3 in order to better control the axial backlash and make sure that no surface interpenetration occurs. For friction coefficients, the Jacod [47] model characterized by Eq. 2.26 is preferred, because it provides a more realistic distribution of friction in the contact areas. Alternatively, a simple Coulomb model could also be used. Finally, the mechanism is lubricated using SKF LGWA2 with the shown properties and a chosen value of 12 MPa for the Eyring stress.

The dimensional value of the total residue ( $R_z \cdot c|F_N|/N_R$ ) is represented on the top side of Fig. 3.6 for different slip ratios and we can recognize a strictly monotonous function. A zoom

	Notation	Value	Meaning
<b>Geometry</b>	$\chi$	1	PRS type: 1 for standard and 0 for inverted
	-	design	geometry definition method: design or simulation
	$2r_S$	30 mm	rounded pitch radius for the screw
	$l_S$	10 mm	lead of the screw (or nut)
	$n_S$	5	number of starts on the screw (or nut)
	$n_R$	1	number of starts on the roller
	$\alpha_n$	45°	normal profile pressure angle
	$r_{BS}$	$\infty$	screw profile curvature radius (straight)
	$r_{BR}$	6 mm	roller profile curvature radius (convex)
	$r_{BN}$	$\infty$	nut profile curvature radius (straight)
	$D_{zS}$	0	desired roller-screw axial backlash
	$D_{zN}$	0	desired roller-nut axial backlash
	$N_R$	9	number of rollers
	$N_C$	28	number of roller-screw or roller-nut contacts per roller
	$D_b$	6 mm	roller head diameter
	$L_b$	6 mm	roller head length
	$e_b$	0.1 mm	maximum allowed eccentricity for $P/R$ bearing
	$\alpha_g$	20°	gear pressure angle
$L_r$	70 mm	total roller length for mass calculation	
<b>Loading</b>	$F_N$	35 kN	external force on the nut
	$\omega_{s/n}$	400 rpm	steady-state rotation speed of the screw
<b>Materials</b>	$E'$	230.77 GPa	relative modulus of elasticity for threaded contacts
	$\rho_r$	7810 kg/m <sup>3</sup>	roller density for mass calculation
<b>Friction</b>	$N_1 = N_2$	21	number of points for contact area discretization
	-	Jacod	friction coefficient model: Coulomb or Jacod [47]
	$\eta_0$	166.5 mPas	lubricant ambient viscosity
	$\alpha$	30 GPa <sup>-1</sup>	pressure-viscosity coefficient
	$\tau_0$	12 MPa	Eyring stress for the lubricant
	$C_{P/N}$	0	auxiliary $P/N$ friction torque, same sign as $\omega_{s/n}$
	$C_{P/S}$	0	auxiliary $P/S$ friction torque, opposite sign to $\omega_{s/n}$

Table 3.2: Reference example: input parameters

around the ideal  $\epsilon^*$  shows a change in the function sign, as expected. Therefore, the steady-state solution in terms of the slip ratio is located at the intersection with the  $R_z = 0$  axis. It can be seen from the figure that this solution is closely below  $\epsilon^*$  and above the measurement performed through experiment #6. This makes sense because  $\epsilon^*$  cannot be exceeded for a standard PRS and we would expect slightly more slip in practice than in the numerical model, which represents an idealized approximation of the real mechanism. The bottom side of the figure shows the results obtained for an inverted PRS with the same list of input parameters, i.e. table 3.2.

It is possible to perform a more in-depth analysis of the total residue  $R_z$  to compare the relative influence of individual contributions. As shown on the left side of Fig. 3.7, the circumferential gear force is the only active component in terms of the rollers rotation  $\omega_{r/p}$  around their axes, while spin torques, the planet carrier bearing and contact forces are all resistive. When stationary equilibrium is reached, the sum of these contributions becomes nil. This confirms that gears are an essential component of the PRS mechanism, required to move the rollers to their correct position as they turn.

The contribution of the journal bearing between roller heads and the planet carrier appears to be very small, compared to the others. This is because the maximum allowed eccentricity  $e_b$  takes a relatively high value in this example, which is based on the real mechanism used to perform experiments. This leads to a very low value of the Sommerfeld number  $S$ , situated outside the table given in reference [48]. In order to obtain the small friction torque that corresponds to this bearing model, a linear extrapolation was performed, as shown on the right

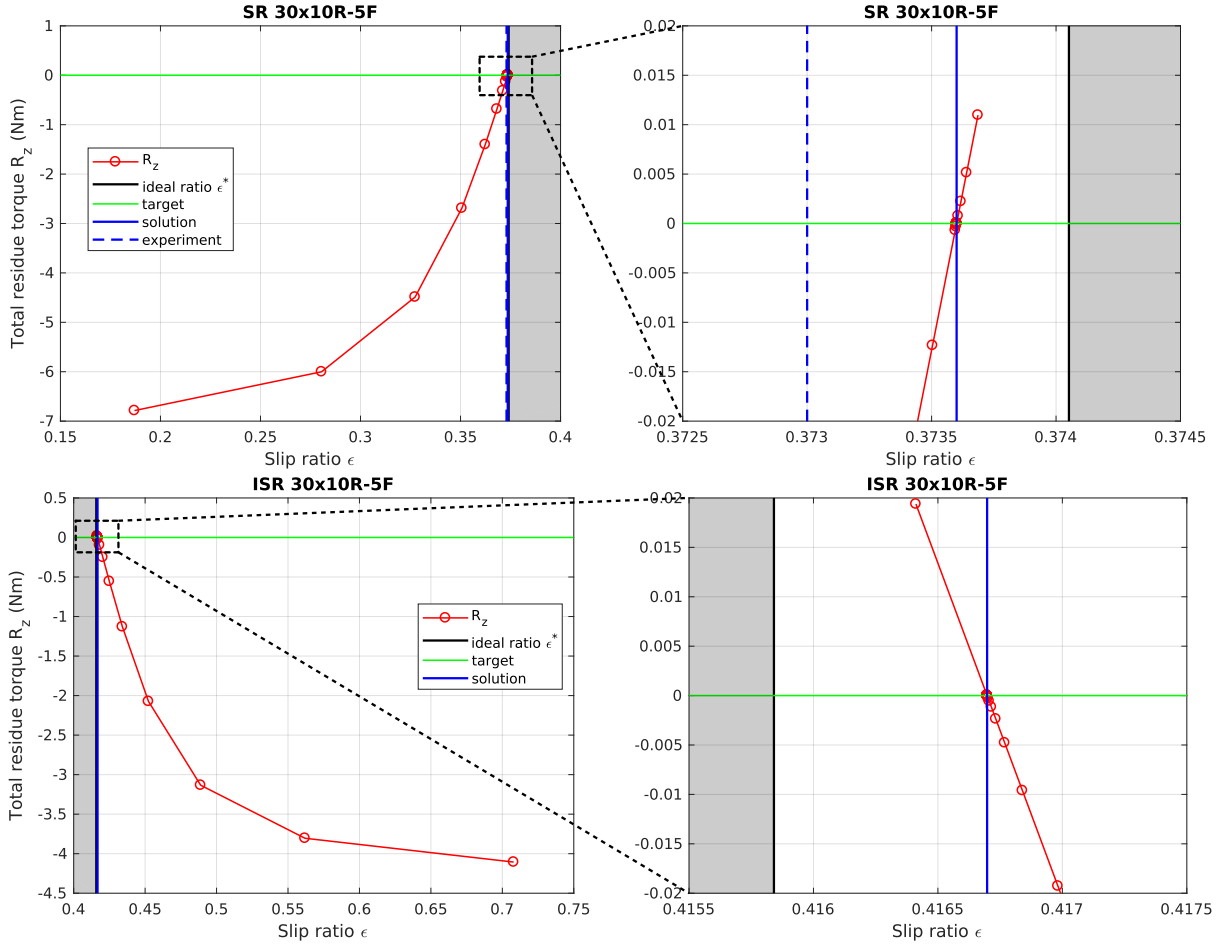


Figure 3.6: Dimensional residue torque  $R_z \cdot c|F_N|/N_R$  for the reference example and an inverted PRS, with zoom around the stationary solution

side of Fig. 3.7.

Once the algorithm converges and the stationary slip ratio solution is found, the model can use Eqs. 3.30 – 3.31 and calculate the external steady-state torques  $C_S$  and  $C_N$  applied on the screw and nut. Unless the user imposes a different value for the slip ratio, it is possible to verify that the two torques are consistently equal in modulus and of opposite signs, within numerical error:

$$C_N \approx -C_S \quad \text{for the stationary value of } \epsilon \quad (3.46)$$

This dynamic torque is always higher than the one obtained in statics through Eq. 3.18, as expected. Such results can be used to check the validity of the model proposed in this chapter.

### 3.2.8 Power dissipation

The numerical model presented in the previous sections can compute the total power dissipated by the PRS mechanism in two ways. The first option consists in summing up all the individual contributions caused by the five sources of friction presented in Fig. 3.1. If  $W_t$  denotes the complete sum, we have:

$$W_t = N_R (N_C (W_I + W_J) + W_{P/R}) + W_{P/S} + W_{P/N} \quad (3.47)$$

The convention used in this memoir is that dissipation should be negative, while input power

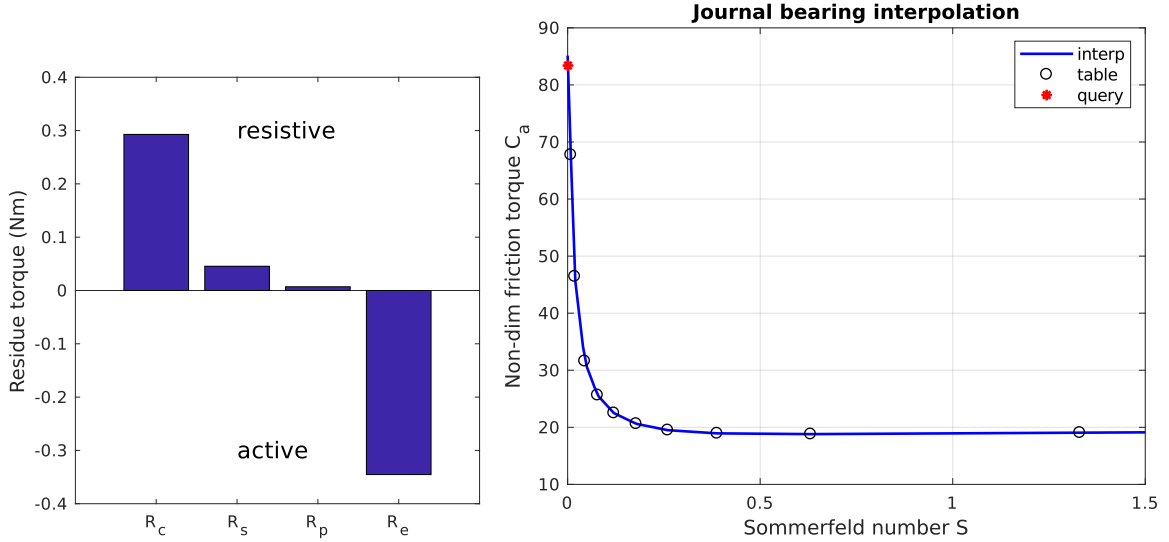


Figure 3.7: Stationary solution of the reference example. Left: dimensional residue torque contributions. Right: non-dimensional friction torque  $C_a$ , found using a linear extrapolation of table values given in reference [48]

is positive. Therefore, the contributions due to the planet carrier can easily be expressed as:

$$W_{P/R} = C_{P/R} \cdot \omega_{r/p} = C_{P/R} \cdot \lambda \omega_{s/n} \quad (3.48)$$

$$W_{P/S} = C_{P/S} \cdot \omega_{s/p} = C_{P/S} \cdot (1 - \epsilon) \omega_{s/n} \quad (3.49)$$

$$W_{P/N} = C_{P/N} \cdot \omega_{n/p} = -C_{P/N} \cdot \epsilon \omega_{s/n} \quad (3.50)$$

where  $\lambda$  is a kinematic variable related to the slip ratio  $\epsilon$  by the perfect gears Eq. 2.4.

For the  $I$  and  $J$  contact wrenches, purely normal loads should not dissipate any power because surfaces do not interpenetrate and there is no relative movement in this direction. Furthermore, spin torques were computed as the sum of local sliding friction moments, so we must avoid counting this contribution twice. In the end, the power dissipated within the contact areas should be calculated as:

$$W_M = - \int_d \vec{T}_D \cdot \vec{v}_D \approx - \frac{6N_M}{\pi N_1 N_2} \sum \left( \mu_D \sqrt{1 - \left(\frac{t_{1D}}{a}\right)^2 - \left(\frac{t_{2D}}{b}\right)^2} \cdot \sqrt{(\vec{v}_D \cdot \vec{t}_1)^2 + (\vec{v}_D \cdot \vec{t}_2)^2} \right) \quad (3.51)$$

where  $M$  is either  $I$  or  $J$  and the normal component of the local sliding velocity field was neglected ( $\vec{v}_D \cdot \vec{n}_M \approx 0$ ) for all the discretization points shown in Fig. 2.7.

It would be interesting to see how  $W_I$  and  $W_J$  vary with the number of discretization points, to ensure that the value  $N_1 = N_2 = 21$  specified in table 3.2 is high enough to guarantee accurate results. As shown in Fig. 3.8, the numerical dissipated power calculated using Eq. 3.51 converges relatively fast and sufficient precision is reached for  $N_1 = N_2 = 21$  points. For practical reasons, the figure displays results for both the Jacod and Coulomb friction models. While the  $\tau_0$  and  $\mu_a$  values have been set according to our best understanding of the real mechanism, it is important to remember that the model is not set in stone and depends on the user input.

Figure 3.8 illustrates another important result: for  $N_1 = N_2 = 1$ , the predicted power dissipation is very bad. In this case, contact areas are not discretized; in other words, single point contacts are considered. Therefore, spin torques at both  $I$  and  $J$  are assumed to be nil, according to Eq. 3.10. Although this simplifying assumption might appear tempting and is used by the most advanced numerical models currently available in literature [28], Fig. 3.8 clearly shows that the corresponding results are incorrect. Spin torques cannot be neglected in terms of power dissipation.

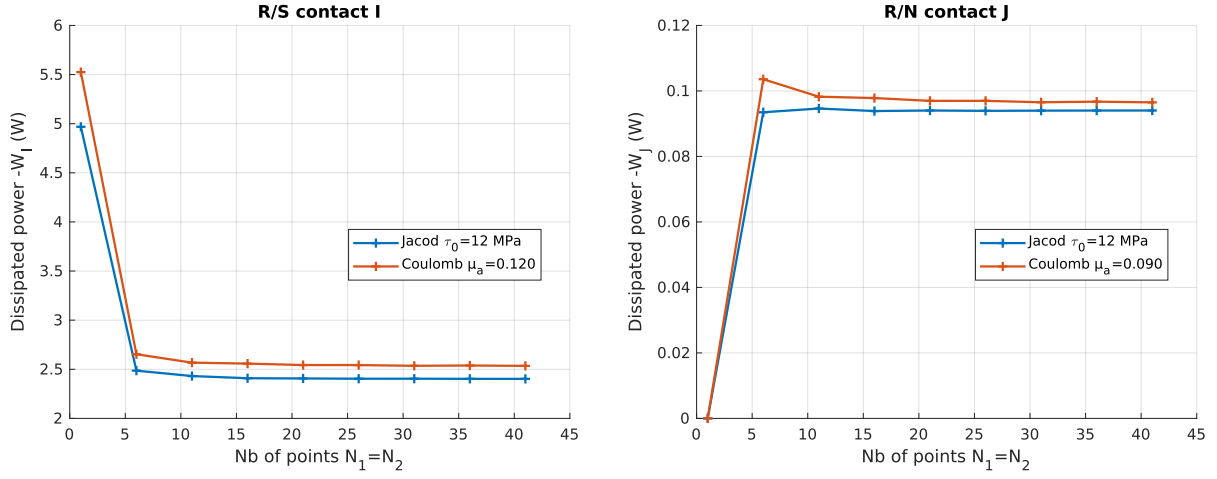


Figure 3.8: Power dissipated at a single  $I$  or  $J$  contact for the reference example. Friction model comparison for increasing  $N_1 = N_2$  discretization points.

### 3.2.9 Efficiency

The second method for calculating the total power dissipated by the PRS makes use of the mechanism efficiency, defined as:

$$H = -\frac{W_{useful}}{W_{input}} = \begin{cases} -\frac{F_N \dot{z}_{n/s}}{C_S \omega_{s/n}} = \frac{F_N l_s}{2\pi C_S} & \text{if standard PRS} \\ -\frac{F_S \dot{z}_{s/n}}{C_N \omega_{n/s}} = \frac{F_S l_s}{2\pi C_N} & \text{if inverted PRS} \end{cases} \quad (3.52)$$

where the stable displacement Eq. 2.5 has been used. Also note that the two expressions for standard and inverted PRS are in fact equivalent for the equilibrium value of the slip ratio, since the external forces  $F_S$  and  $F_N$  on the screw and nut were considered to be equal in modulus and of opposite sign (Eq. 3.1) and the same was numerically found to be true for  $C_S$  and  $C_N$ , as mentioned in the previous section.

The total power dissipated by the mechanism can then be expressed as:

$$W_t = -W_{input} - W_{useful} = (H - 1)W_{input} = \begin{cases} (H - 1)C_S \omega_{s/n} & \text{if standard PRS} \\ -(H - 1)C_N \omega_{s/n} & \text{if inverted PRS} \end{cases} \quad (3.53)$$

and again, the formulas for standard and inverted PRS are equivalent when  $\epsilon$  takes the stationary value determined by the numerical model.

Compared to the first method which consists in calculating and summing up all the individual contributions, the second option only needs to determine the external torque  $C_S$  or  $C_N$  on the screw or nut (Eq. 3.30 – 3.31). The other variables are input parameters, according to the example given in table 3.2. Therefore, the two methods are fundamentally different, but should lead to the same result. In practice, we can verify that it is always the case, within numerical error. The only required condition is that  $\epsilon$  takes the calculated equilibrium value and is not imposed differently by the user. This numerical equivalence of the two options confirms the reliability of the proposed model.

## 3.3 Parametric study

In this section, we attempt to identify new ways of improving the mechanism performance by analyzing the effect of different design parameters on efficiency and dissipated power. We use the example in table 3.2 as a reference for numerical simulations, in which parameters judged

important are varied one at a time. As a first approach, we will stick to standard PRS and always use the *design* method to define the mechanism geometry.

For the reference example, the numerical model predicts an efficiency value of 78.6% for the stationary regime. Keeping the other parameters constant, the nominal screw diameter is then varied and results are plotted according to Fig. 3.9. The five power contributions of individual friction sources are stacked as percentages with respect to the total value in the reference case. The figure also plots the measurement performed on the test bench described in Fig. 2.4.

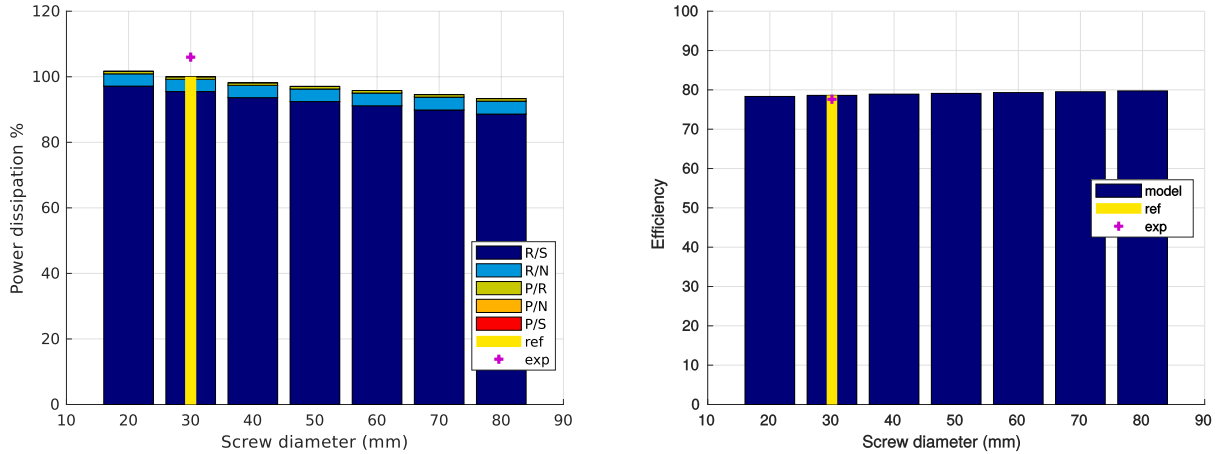


Figure 3.9: Relative power dissipation  $W_t/W_t^{ref}$  and efficiency  $H$  (as percentages) for different values of the screw nominal diameter. Contributions from the 5 friction sources are stacked. Reference example marked with yellow. Measured values marked with +.

First of all, we notice that more than 90% of the power is dissipated through the roller-screw contacts. The contribution of spin at the roller-nut interface is much smaller, but cannot be neglected. Of course, this can only be true for a standard PRS and we would expect things to work the other way around for the inverted type. Furthermore, due to the relatively large eccentricity for the  $P/R$  journal bearing ( $e_b = 0.1$  mm), the corresponding power contribution is very small, unlike what is mentioned in current literature [28].

Secondly, the dissipated power seems to decrease slightly as the screw diameter increases, while efficiency is more or less constant. This might be a bit surprising, but makes sense since larger mechanisms require less torque from the motor to obtain the same axial force  $F_N$ .

Finally, the experimental value falls relatively close to the predicted numerical result, which indicates that the chosen Eyring stress  $\tau_0 = 12$  MPa was not too bad. Of course, it remains possible for us to perform a finer adjustment of friction coefficients, so that numerical values fall exactly on the measured ones, but the interest of such a study would be limited. The goal here is to observe major tendencies and identify possible design solutions.

For the other studied parameters, the corresponding power-efficiency figures are shown in appendix C to facilitate reading. In terms of geometry, these parameters include the screw lead, normal pressure angle, screw and roller profile curvatures and the number of rollers. Some of the friction inputs are then investigated, like the  $P/R$  bearing eccentricity  $e_b$  and the auxiliary torque  $C_{P/N}$ , as well as the ambient viscosity and Eyring stress of the lubricant. Finally, we analyze the influence of loading conditions in terms of input speed on the screw and external force on the nut.

Results show that PRS efficiency is relatively constant for most of these parameter variations, except lubrication variables: the ambient viscosity  $\eta_0$  and the Eyring stress  $\tau_0$ . Increasing these values means that friction coefficients are higher, which lowers the mechanism efficiency. More precise variation laws could be deduced by plotting more points, but a first approximation of the results in the figures allows us to say that:

$$H \approx H(\tau_0, \eta_0) \quad \text{such that} \quad \begin{cases} \partial H / \partial \tau_0 = \text{cst.} < 0 \\ \partial H / \partial \ln \eta_0 = \text{cst.} < 0 \end{cases} \quad \text{and} \quad \begin{cases} \tau_0 = 0 \Rightarrow H = 1 \quad \forall \eta_0 \\ \eta_0 = 0 \Rightarrow H = 1 \quad \forall \tau_0 \end{cases} \quad (3.54)$$

which means that efficiency could be approximated by a function of the form:

$$H \approx B_1 - B_2 \tau_0 \ln \eta_0 \quad (3.55)$$

where  $\tau_0$  is in MPa,  $\eta_0$  in mPa·s and  $B_{1,2}$  are two constants determined from the figures:  $B_1 = 98.1\%$  and  $B_2 = 0.32\%$ . Of course, Eq. 3.55 is not as accurate as the complete numerical model, but it provides an easy to use formula which points out the relative influence of important parameters.

The dissipated power, on the other hand, is affected by more inputs than efficiency. As shown in appendix C,  $W_t$  increases linearly with the screw speed  $\omega_{s/n}$  and the external force on the nut  $F_N$ . Both of these curves pass by the (0,0) origin, as expected. Since the reference example used here was chosen to be a match of the real PRS used in the kinematic experiments, we were able to plot some of the measurement points as well and thus confirm the observed numerical behavior.

Obviously, lubrication properties influence power dissipation too and we can observe the proportionality between  $W_t$  and the Eyring stress  $\tau_0$ , as well as the logarithm of ambient viscosity  $\ln \eta_0$ . Any auxiliary friction torques like  $C_{P/N}$  also seem to increase  $W_t$  linearly, although their contribution is questionable in view of the results obtained for the radial play  $2e_b$ . This parameter is used in the journal bearing model to calculate friction between roller heads and the planet carrier. We can see that precise machining is required to cause an amount of dissipated power comparable to that of  $R/N$  contact spin. Besides, this scenario is unlikely to occur in practice because the carrier is usually designed with relatively high radial plays, between 0.2 and 0.5 mm.

The stationary equilibrium model developed in the current chapter was mainly put together in hopes of identifying opportunities for improving the mechanism performance. Geometrical parameters were our best bet, yet the numerical results shown in appendix C proved somewhat disappointing. It is shown that profile curvatures and the number of rollers do not decrease power dissipation significantly enough to make a difference. The customary value of the normal pressure angle ( $45^\circ$ ) also appears to be good enough. The only geometrical parameter to considerably affect  $W_t$  remains the screw (and nut) lead  $l_S$ . Higher leads increase the useful power output, but also dissipate more, such that in the end efficiency remains constant.

### 3.4 Conclusion

In this chapter, we investigate the numerical prediction of PRS efficiency and dissipated power. A stationary force equilibrium model is developed, which distinguishes five different friction sources. Results are used to perform a parametric study which identifies the important variables and their relative influence. The main purpose of this study is to uncover design options which could boost roller screw performance.

The model is specifically built to work for both standard and inverted PRS, such that the slip ratio  $\epsilon$  can be either imposed by the user or calculated numerically. It is assumed that all rollers are identical, with parallel axes situated at a fixed distance from the central screw-nut-carrier axis. Only the actuator mode is considered, where rotation is transformed into translation.

Threaded contact forces are a combination of normal loads, sliding friction and spin torques. It is shown that sliding friction is usually responsible for more than 90% of the total power dissipated by the mechanism. Since normal loads do not dissipate at all, the remaining percentage gets split between spin and any auxiliary friction torques caused by the planet carrier.

The force equilibrium model also shows that the combined effects of contact forces push the rollers towards the nut for a standard PRS and towards the screw for inverted PRS. In the static case, this action is balanced by the presence of the carrier. Steady-state equilibrium, on the other hand, additionally requires gears to be taken into account as active components.

The obtained numerical values for the slip ratio are in accordance with the kinematic model and experiments described in the previous chapter. Two different ways of calculating power

dissipation are used to reach an identical result and thus ensure the accuracy of the proposed method.

Parametric study results show that PRS efficiency is high (around 80%), but difficult to control. Only lubricant properties seem to affect it significantly. Power dissipation is influenced by a higher number of parameters, including the screw diameter, lead, speed and input force. Nevertheless, the list remains small and most of these parameters are usually imposed by the application. More accessible design variables, like profile curvatures, the pressure angle or the number of rollers have a negligible effect on the dissipated power, which leaves designers with limited options when trying to improve mechanism performance.

# Main conclusions

Instead of rewriting the detailed conclusions from each chapter using different words, we prefer providing the reader with a summarizing list of the most important scientific results, as well as some ideas for future research.

1. It is convenient to use the planet carrier as a reference, because the radial and circumferential coordinates of the contact points remain constant in this frame when components move. Furthermore, these coordinates have to be determined numerically, since it is impossible to obtain an analytical solution directly, without making approximations.
2. Current literature intuitively assumes that principal directions of curvature for threaded surfaces are known. In the current work, differential geometry is used to show that the result should be different.
3. Threaded contacts in a PRS are not necessarily non-conforming. However, conforming curvatures are usually small such that the classic Hertzian theory can still be applied if sufficient care is taken to modify some of the equations.
4. During the roller screw design process, at least one of the threaded components needs to be rectified in order to guarantee backlash. This operation consists in adjusting the nominal diameter of the screw (for standard PRS) or the nut (for inverted PRS), which results in slightly different values from the rounded numbers normally found in product catalogs.
5. The minimum and maximum threaded profile radii should vary with pitch, such that the roller-screw contact points in a standard PRS are found closer to the outer radius when pitch increases.
6. The stationary regime kinematics in a PRS can be fully defined by only two variables: the input rotation speed and a non-dimensional ratio which quantifies the amount of circumferential slip present in the roller screw. Furthermore, this ratio places the mechanism somewhere between a friction screw and an epicyclic gear train and can be measured through the rotation speed of the planet carrier.
7. Slip cannot be entirely eliminated in a roller screw, but it is possible to calculate its minimum amount. The corresponding value of the slip ratio only depends on geometrical quantities.
8. Experiments show that the amount of slip in real PRS is very close to the minimal value calculated theoretically, which leaves little room for improvement in terms of steady-state kinematics. Numerical results exhibit the same tendency.
9. The roller-screw and roller-nut interfaces are very different in terms of local kinematics: one is characterized by a movement of pure spin, while the other has a spin which gets dissolved in a much more important field of uniform sliding.
10. The sliding velocity vector at the center of contact areas is usually not aligned with the principal directions of the ellipse. Depending on profile curvatures, the Hertzian ellipse can turn anywhere between 0 and 90° around the contact point. This makes classic EHL lubrication theory difficult to apply.

11. Local friction coefficients can be obtained using numerical, non-linear lubrication models. However, results show that the field is relatively uniform, which means that a simple Coulomb friction model could also be used without too much inaccuracy.
12. In the static case, it is impossible to satisfy all the force equilibrium equations considering only the screw, the rollers and the nut. For the steady-state scenario, other components such as gears and the planet carrier must also be taken into account.
13. Sliding friction is responsible for more than 90% of the total power dissipated by the mechanism. Spin has the second largest contribution and should not be neglected. Other friction sources, mainly related to the planet carrier, only have a small effect.
14. Roller screw efficiency is high (around 80%), but very difficult to control. It is almost independent of geometrical parameters and loading; only the lubrication conditions seem to influence it significantly.

## Future research

1. In this work, the influence of local deformations on the global geometry and location of the contact points was neglected. In other words, solids are considered to be infinitely rigid and the Hertzian theory is only applied as a result. Future studies could include thread deflection as a secondary effect of normal loads. A more expensive way of considering deformable solids would be to use finite elements.
2. The test bench presented in Fig. 2.4 could be improved by using a motor which allows a wider range of rotation speeds to be studied. Unfortunately, the hydraulic system used to load the nut axially cannot impose low forces at high speeds, which is why the corresponding experimental points in Fig. 2.5 are missing. A different measurement strategy could avoid this problem.
3. The HFRR device used in friction coefficient measurements was not well adapted for the high pressures (2.5 GPa) commonly encountered in roller screws. In order to simulate these threaded contacts better, a specific apparatus should be developed.
4. The lubricant remains the most influential parameter in terms of efficiency and power dissipation, yet experimental data was only obtained for two greases in the current work. A wider range of samples could be studied in the future.
5. The amount of power dissipated by the mechanism could be directly used as an input for a thermal model of the roller screw. This study could uncover solutions for reducing the fast rise in temperature when the PRS is heavily loaded.

## Appendix A

# Contact points location algorithm

This section explains how Eq. 1.27 for the external unit normal vector at any point can be used to deduce the location of the contact points between two threaded surfaces. We consider infinitely rigid solids and a curved profile (convex or concave) for at least one of the surfaces. This ensures that the contact is a collection of single points; curves would be obtained if both surfaces were straight [13]. Some exotic curvature combinations can even lead to contacts situated beyond or on the edges of the threads, but the model signals these cases out with an error.

Since the resulting non-linear equations have to be solved numerically, explanations are given for a very efficient Newton-Raphson algorithm which computes the unique solution when it exists. The case of two external threads is used for presenting the algorithm, but the model works and has been verified for internal threads as well if the user specifies the shape of the air volume contained within (complementary volume). The algorithm only yields the contact points location in the  $xy$  (radial-circumferential) plane. The axial  $z$  coordinates depend on backlash and are deduced separately.

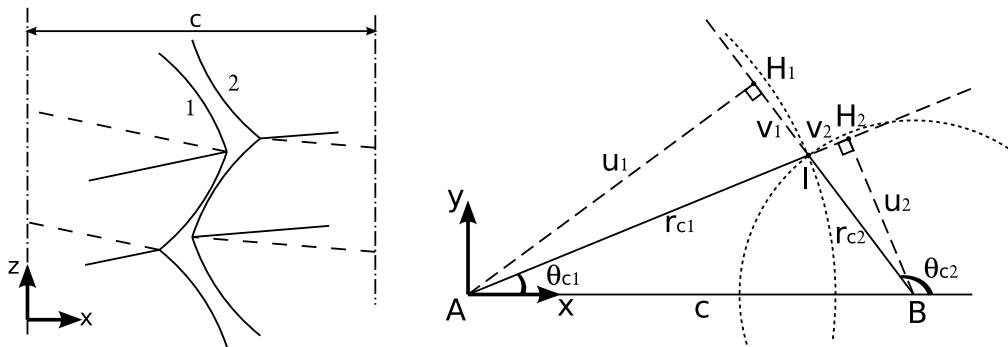


Figure A.1: Location of the  $I_2$  contact point in the  $xy$  plane in the general case

Figure A.1 shows the axial  $zx$  cut of the two external, right-handed threads in contact. As shown by Jones and Velinsky [33], the contact points do not necessarily exist in this plane. If the two thread axes remain parallel, the points are generally on a line which passes through  $I$  and is also parallel to the axes. This is due to the difference in helix angles and/or profile curvatures. In the general case, it is possible to build the triangle  $AIB$  with the shown dimensions.

Although reference [33] presents a method for calculating the coordinates of point  $I$ , it uses one geometrical assumption that we found inaccurate. In particular, it assumes that the two normal surface vectors are contained in the same predefined plane, perpendicular to the helix of surface 1. The current work does not make this assumption and uses the general Eq. 1.27 deduced previously.

Some authors have tried to find the coordinates of point  $I$  (called "meshing point" [34]) using purely analytical formulas, but they had to use small approximations to neglect some terms in the expression. Others have proposed numerical methods employing a grid [36]. A comparison with both the results obtained in reference [34] and [36] is provided in the examples of the first

chapter in the current work.

Here, the analysis focuses on finding the coordinates of point  $I$  in the  $xy$  plane, i.e. unknowns  $r_{C1}, r_{C2}, \theta_{C1}, \theta_{C2}$ . The distance  $c$  between the two axes is taken as a parameter, as well as both surface geometries. By default, all vectors are expressed in Cartesian ( $\vec{x}, \vec{y}, \vec{z}$ ) coordinates. A basic analysis of triangle  $AIB$  yields the following:

$$\begin{bmatrix} r_{C1} & 0 \\ 0 & r_{C1} \end{bmatrix} \cdot \begin{bmatrix} \cos \theta_{C1} \\ \sin \theta_{C1} \end{bmatrix} - \begin{bmatrix} r_{C2} & 0 \\ 0 & r_{C2} \end{bmatrix} \cdot \begin{bmatrix} \cos \theta_{C2} \\ \sin \theta_{C2} \end{bmatrix} = \begin{bmatrix} c \\ 0 \end{bmatrix} \quad (\text{A.1})$$

This expression, however, only contains two equations and in order to solve for the four unknowns we need at least two more. They can be obtained by writing that the corresponding surface normals are opposite vectors at the point of contact, yielding:

$$\begin{aligned} & \frac{1}{\sqrt{\left(\frac{h'_1}{\cos \beta_1}\right)^2 + \left(\frac{l_1}{2\pi r_{C1}}\right)^2 + 1}} \begin{bmatrix} \frac{h'_1}{\cos \beta_1} \cos \theta_{C1} - \frac{\gamma_1 l_1}{2\pi r_{C1}} \sin \theta_{C1} \\ \frac{h'_1}{\cos \beta_1} \sin \theta_{C1} + \frac{\gamma_1 l_1}{2\pi r_{C1}} \cos \theta_{C1} \\ -\gamma_1 \end{bmatrix} = \quad (\text{A.2}) \\ & = \frac{-1}{\sqrt{\left(\frac{h'_2}{\cos \beta_2}\right)^2 + \left(\frac{l_2}{2\pi r_{C2}}\right)^2 + 1}} \begin{bmatrix} \frac{h'_2}{\cos \beta_2} \cos \theta_{C2} - \frac{\gamma_2 l_2}{2\pi r_{C2}} \sin \theta_{C2} \\ \frac{h'_2}{\cos \beta_2} \sin \theta_{C2} + \frac{\gamma_2 l_2}{2\pi r_{C2}} \cos \theta_{C2} \\ -\gamma_2 \end{bmatrix} \end{aligned}$$

and since contact takes place between the top face of one thread and the bottom of the other:

$$\gamma_1 = -\gamma_2 \quad (\text{A.3})$$

These considerations are true for the contact between two externally threaded shafts. If one of the threads is internal, we would impose normals and  $\gamma$ 's to be equal instead of opposite. However, it can be shown that this does not change the three resulting equations, which can be written in all cases under the form:

$$\left\{ \begin{array}{l} \left(\frac{h'_1}{\cos \beta_1}\right)^2 + \left(\frac{l_1}{2\pi r_{C1}}\right)^2 = \left(\frac{h'_2}{\cos \beta_2}\right)^2 + \left(\frac{l_2}{2\pi r_{C2}}\right)^2 \\ \begin{bmatrix} \frac{\gamma_1 h'_1}{\cos \beta_1} & -\frac{l_1}{2\pi r_{C1}} \\ \frac{l_1}{2\pi r_{C1}} & \frac{\gamma_1 h'_1}{\cos \beta_1} \end{bmatrix} \cdot \begin{bmatrix} \cos \theta_{C1} \\ \sin \theta_{C1} \end{bmatrix} = \begin{bmatrix} \frac{\gamma_2 h'_2}{\cos \beta_2} & -\frac{l_2}{2\pi r_{C2}} \\ \frac{l_2}{2\pi r_{C2}} & \frac{\gamma_2 h'_2}{\cos \beta_2} \end{bmatrix} \cdot \begin{bmatrix} \cos \theta_{C2} \\ \sin \theta_{C2} \end{bmatrix} \end{array} \right. \quad (\text{A.4})$$

Only two of these equations are independent, but if we add equation A.1 we obtain a total of four independent equations to solve for the location of the contact points. As the 4x4 system is non-linear, however, it requires a numerical algorithm to approximate the solution when it exists. Computation time can be highly improved by eliminating the angles  $\theta_{C1}$  and  $\theta_{C2}$  analytically in order to obtain a 2x2 system. This can be done by expressing the  $\theta_{C1}$  vector in equation A.4

as a function of the  $\theta_{C2}$  vector and then replacing the result in equation A.1. We obtain:

$$\begin{bmatrix} -r_{C2} - v_1 & u_1 \\ -u_1 & -r_{C2} - v_1 \end{bmatrix} \cdot \begin{bmatrix} \cos \theta_{C2} \\ \sin \theta_{C2} \end{bmatrix} = \begin{bmatrix} c \\ 0 \end{bmatrix} \quad \text{where} \quad (\text{A.5})$$

$$v_1 = -r_{C1} \frac{\left( \frac{\gamma_1 \gamma_2 h'_1 h'_2}{\cos \beta_1 \cos \beta_2} + \frac{l_1 l_2}{4\pi^2 r_{C1} r_{C2}} \right)}{\left( \frac{h'_1}{\cos \beta_1} \right)^2 + \left( \frac{l_1}{2\pi r_{C1}} \right)^2} \quad u_1 = r_{C1} \frac{\left( \frac{\gamma_2 h'_2 l_1}{2\pi r_{C1} \cos \beta_2} - \frac{\gamma_1 h'_1 l_2}{2\pi r_{C2} \cos \beta_1} \right)}{\left( \frac{h'_1}{\cos \beta_1} \right)^2 + \left( \frac{l_1}{2\pi r_{C1}} \right)^2} \quad (\text{A.6})$$

which means that angle  $\theta_{C2}$  is such that:

$$\begin{bmatrix} \cos \theta_{C2} \\ \sin \theta_{C2} \end{bmatrix} = \begin{bmatrix} -\frac{(r_{C2} + v_1)c}{(r_{C2} + v_1)^2 + u_1^2} \\ \frac{u_1 c}{(r_{C2} + v_1)^2 + u_1^2} \end{bmatrix} \quad (\text{A.7})$$

Using the fact that  $\sin^2 \theta_{C2} + \cos^2 \theta_{C2} = 1$ , an interesting relationship is obtained:

$$u_1^2 + (r_{C2} + v_1)^2 = c^2 \quad (\text{A.8})$$

which can be developed by replacing the  $u_1$  and  $v_1$  notations to get:

$$f_2(r_{C1}, r_{C2}) = \left( \frac{r_{C1} \gamma_1 h'_1}{c \cos \beta_1} - \frac{r_{C2} \gamma_2 h'_2}{c \cos \beta_2} \right)^2 + \left( \frac{l_1 - l_2}{2\pi c} \right)^2 - \left[ \left( \frac{h'_1}{\cos \beta_1} \right)^2 + \left( \frac{l_1}{2\pi r_{C1}} \right)^2 \right] = 0 \quad (\text{A.9})$$

Furthermore, Eq. A.4 can be used to write:

$$f_1(r_{C1}, r_{C2}) = \left( \frac{h'_1}{\cos \beta_1} \right)^2 + \left( \frac{l_1}{2\pi r_{C1}} \right)^2 - \left( \frac{h'_2}{\cos \beta_2} \right)^2 - \left( \frac{l_2}{2\pi r_{C2}} \right)^2 = 0 \quad (\text{A.10})$$

The functions  $f_1$  and  $f_2$  are dimensionless and must be nil at the location of the contact point. Together, they constitute the 2x2 system we have to solve numerically. For the purposes of this work, we chose to employ a Newton-Raphson algorithm and to calculate the necessary Jacobian matrix analytically by differentiating  $f_1$  and  $f_2$ :

$$\frac{\partial f_1}{\partial r_{C1}} = \frac{2h'_1 h''_1}{\cos^2 \beta_1} - \frac{l_1^2}{2\pi^2 r_{C1}^3} \quad (\text{A.11})$$

$$\frac{\partial f_1}{\partial r_{C2}} = -\frac{2h'_2 h''_2}{\cos^2 \beta_2} + \frac{l_2^2}{2\pi^2 r_{C2}^3} \quad (\text{A.12})$$

$$\frac{\partial f_2}{\partial r_{C1}} = \frac{2}{c^2} \left( \frac{r_{C1} \gamma_1 h'_1}{\cos \beta_1} - \frac{r_{C2} \gamma_2 h'_2}{\cos \beta_2} \right) \frac{\gamma_1 (h'_1 + r_{C1} h''_1)}{\cos \beta_1} \quad (\text{A.13})$$

$$\frac{\partial f_2}{\partial r_{C2}} = -\frac{2}{c^2} \left( \frac{r_{C1} \gamma_1 h'_1}{\cos \beta_1} - \frac{r_{C2} \gamma_2 h'_2}{\cos \beta_2} \right) \frac{\gamma_2 (h'_2 + r_{C2} h''_2)}{\cos \beta_2} \quad (\text{A.14})$$

The algorithm was tested for the whole range of PRS geometries available on the market [1] and in all cases it was found that ten iterations are largely enough to achieve convergence with a machine precision relative error ( $< 1e-13$ ) on  $f_1$  and  $f_2$ . Calculations were performed such that one of the two surfaces always had a straight profile. For more complex curvature combinations, the program may require a few hundred iterations to converge, but computing time remains negligible on a modern desktop computer.

The solution does not always exist: imagine the case of two external, concave threads, for example. We also tested a few special cases when the algorithm converges, but the solution is not physical. Fake solutions can be avoided by verifying for both radii of contact that:

$$r_{min} < r_C < r_{max} \quad (\text{A.15})$$

where  $r_{min}$  and  $r_{max}$  are the minimum and maximum profile radii for the corresponding surface.

The angles  $\theta_{C1}, \theta_{C2} \in [-\pi, \pi]$  can be easily deduced once  $r_{C1}$  and  $r_{C2}$  are known. From the above calculations, it can be shown that:

$$\begin{bmatrix} \cos \theta_{C2} \\ \sin \theta_{C2} \end{bmatrix} = \begin{bmatrix} -\frac{r_{C2} + v_1}{c} \\ \frac{u_1}{c} \end{bmatrix} \quad \begin{bmatrix} \cos \theta_{C1} \\ \sin \theta_{C1} \end{bmatrix} = \begin{bmatrix} \frac{c^2 - r_{C2}(r_{C2} + v_1)}{r_{C1}c} \\ \frac{r_{C2}u_1}{r_{C1}c} \end{bmatrix} \quad (\text{A.16})$$

where  $u_1$  and  $v_1$  are functions of the two contact radii and basic geometrical parameters, as detailed before. A graphical interpretation of these quantities is shown in Fig. A.1: distance  $AH_1$  is equivalent to  $u_1$  in absolute value and the difference  $BH_1 - r_{C2}$  is equivalent to  $v_1$ . Using the properties of triangles  $AH_1I$  and  $BH_2I$  which are similar, we can rediscover the relationships presented throughout this section.

It is worth it to note that if both  $\gamma_1$  and  $\gamma_2$  are switched,  $v_1$  does not change sign while  $u_1$  does. Furthermore, the contact radii stay the same, while contact angles become opposite. An important symmetry is thus deduced: the 1-*top*/2-*bottom*<sup>1</sup> contact location can be deduced from the 1-*bottom*/2-*top* configuration simply by changing the sign of the contact angles, while keeping the radii constant.

---

<sup>1</sup>1 and 2 refer to surfaces 1 and 2 in Fig. A.1

## Appendix B

# Principal curvatures and directions

The current section explains how principal curvatures and directions of curvature can be calculated at any point on a threaded surface. These results are important because they represent inputs to the Hertzian elliptical model, which proposes a way of determining the shape, size and orientation of the contact areas. In the current work, differential geometry equations are applied to convex, straight or concave threaded surfaces which can be modeled by Eq. 2.2. The curvature results we obtain are found to be in agreement with current literature. However, directions of curvature are different and possibly less intuitive. While our results come from the direct application of classical theory, literature usually uses pre-made assumptions.

Let us first consider an externally threaded shaft centered on the  $z$  axis, like the one in Fig. 1.1. When the surface equation  $z_m = f(r_m, \theta_m)$  is known, it is possible to define a parametrization such that the position of point  $M$  can be expressed as a vector-valued function:

$$\begin{aligned} \vec{\omega} : \mathbb{R}^2 &\rightarrow \mathbb{R}^3 \\ (r_m, \theta_m) &\rightarrow \begin{bmatrix} r_m \\ 0 \\ z_m \end{bmatrix}_{cyl} = \begin{bmatrix} r_m \cos \theta_m \\ r_m \sin \theta_m \\ f(r_m, \theta_m) \end{bmatrix}_{xyz} \end{aligned} \quad (\text{B.1})$$

The partial derivatives of  $\vec{\omega}$  with respect to  $r_m$  and  $\theta_m$  are denoted  $\vec{\omega}_r$  and  $\vec{\omega}_\theta$ , respectively. Both of them are surface tangent vectors at  $M$  and thus constitute a basis for the tangent plane [49]. Depending on the equation, they are not always perpendicular, but can be used to write the surface fundamental coefficients:

$$\begin{aligned} E &= \vec{\omega}_r \cdot \vec{\omega}_r & L &= \vec{\omega}_{rr} \cdot \vec{n} \\ F &= \vec{\omega}_r \cdot \vec{\omega}_\theta & M &= \vec{\omega}_{r\theta} \cdot \vec{n} \\ G &= \vec{\omega}_\theta \cdot \vec{\omega}_\theta & N &= \vec{\omega}_{\theta\theta} \cdot \vec{n} \end{aligned} \quad (\text{B.2})$$

where  $\vec{n}$  denotes a surface unit normal vector at point  $M$  such that:

$$\vec{n} = \frac{\vec{\omega}_r \times \vec{\omega}_\theta}{\|\vec{\omega}_r \times \vec{\omega}_\theta\|} \quad (\text{B.3})$$

The fundamental coefficients are used to define the first and second fundamental forms of the surface, as well as the shape operator (or Weingarten map [49])  $S$  such that:

$$I = \begin{bmatrix} E & F \\ F & G \end{bmatrix} \quad II = \begin{bmatrix} L & M \\ M & N \end{bmatrix} \quad S = I^{-1} \cdot II \quad (\text{B.4})$$

It can be proven that the Weingarten map is self-adjoint on the tangent space [49], which means that its corresponding matrix  $S$  is Hermitian in an orthonormal basis. We can thus diagonalize  $S$ , its eigenvalues are always real and the corresponding eigenvectors always perpendicular. They are denoted principal curvatures and principal directions of curvature, respectively. As

sketched in Fig. 1.11, these quantities represent the widest and thinnest section view curves we would obtain by cutting the surface with a plane containing the normal vector at  $M$ .

By definition, a curvature is the signed inverse of a radius. In order to avoid sign problems caused by surface orientation, we use the following formula to calculate principal curvatures for an externally threaded surface:

$$\rho_{1,2} = \gamma \lambda_{1,2} \quad (\text{B.5})$$

where  $\lambda_{1,2}$  are the computed eigenvalues of matrix  $S$ . The symbol  $\gamma$  is a function equal to  $-1$  for the *top* face of the thread and  $1$  for the *bottom* face. Adding  $\gamma$  provides significant advantage, because it makes the principal curvatures independent of the side chosen on the thread. This way, bumped/convex threads will always have positive principal curvatures, while hollow/concave threads will have at least one curvature which is negative. For straight profiles like the one used in Fig. 1.1, we expect one curvature to be close to 0 (due to the shape of the profile) and the other close to the positive inverse of the pitch radius (due to the cylindrical shape of the shaft).

As for the corresponding principal directions of curvature, they are calculated using:

$$\vec{t}_1 = \frac{v_{11}\vec{\omega}_r + v_{12}\vec{\omega}_\theta}{\|v_{11}\vec{\omega}_r + v_{12}\vec{\omega}_\theta\|} \quad \vec{t}_2 = \frac{v_{21}\vec{\omega}_r + v_{22}\vec{\omega}_\theta}{\|v_{21}\vec{\omega}_r + v_{22}\vec{\omega}_\theta\|} \quad (\text{B.6})$$

where  $v_1$  and  $v_2$  are the computed right eigenvectors of matrix  $S$  and the second subscript denotes their first or second component. Under matrix form, this can be expressed as:

$$V = \begin{bmatrix} v_{11} & v_{21} \\ v_{12} & v_{22} \end{bmatrix} \quad D = \begin{bmatrix} \lambda_1 & 0 \\ 0 & \lambda_2 \end{bmatrix} \quad D = V^{-1} \cdot S \cdot V \quad (\text{B.7})$$

Note that the above equations do not impose a specific order for  $\rho_1$  and  $\rho_2$  and the corresponding directions. In practice, however, it is useful to establish a rule for verifying results and separating different cases. For example, we can decide that the first curvature should always be the minimum of the two in absolute value, i.e.

$$|\rho_1| \leq |\rho_2| \quad (\text{B.8})$$

and interchange the two curvatures/directions whenever this condition is not satisfied. This way, we ensure that the first curvature is always the closest to the curvature of a plane, which has an absolute minimal value of 0.

For the particular case of surfaces which can be modeled by Eq. 1.22, the derivatives of the vector-valued function  $\vec{\omega}$  are expressed as:

$$\vec{\omega}_r = \begin{bmatrix} 1 \\ 0 \\ \frac{\gamma}{\cos \beta} h' \end{bmatrix}_{cyl} ; \quad \vec{\omega}_\theta = \begin{bmatrix} 0 \\ r_m \\ \frac{l}{2\pi} \end{bmatrix}_{cyl} ; \quad \vec{\omega}_{rr} = \begin{bmatrix} 0 \\ 0 \\ \frac{\gamma}{\cos \beta} h'' \end{bmatrix}_{cyl} ; \quad \vec{\omega}_{\theta\theta} = \begin{bmatrix} -r_m \\ 0 \\ 0 \end{bmatrix}_{cyl} ; \quad \vec{\omega}_{r\theta} = \vec{\omega}_{\theta r} = \begin{bmatrix} 0 \\ 1 \\ 0 \end{bmatrix}_{cyl} \quad (\text{B.9})$$

with all vectors in cylindrical coordinates. This leads to the following fundamental coefficients:

$$\begin{aligned}
E &= 1 + \left( \frac{h'}{\cos \beta} \right)^2 & L &= \frac{\gamma h''}{\cos \beta \sqrt{\left( \frac{h'}{\cos \beta} \right)^2 + \left( \frac{l}{2\pi r_m} \right)^2 + 1}} \\
F &= \frac{\gamma h' l}{2\pi \cos \beta} & M &= -\frac{l}{2\pi r_m \sqrt{\left( \frac{h'}{\cos \beta} \right)^2 + \left( \frac{l}{2\pi r_m} \right)^2 + 1}} \\
G &= r_m^2 + \left( \frac{l}{2\pi} \right)^2 & N &= \frac{\gamma r_m h'}{\cos \beta \sqrt{\left( \frac{h'}{\cos \beta} \right)^2 + \left( \frac{l}{2\pi r_m} \right)^2 + 1}}
\end{aligned} \tag{B.10}$$

which can be calculated at any point  $M(r_m, \theta_m, z_m)$  on the surface. However, we can see that only the radius  $r_m$  appears as a variable. This is due to the axisymmetry of the threaded surface, which makes the fundamental coefficients independent of the  $\theta_m$  coordinate.

Throughout this section, we only discussed the case of an external thread. For internal threads (the nut in a roller screw, for example), it is possible to consider the geometry of the space contained within (complementary volume). The theory presented above allows to calculate its principal directions and curvatures, denoted  $\vec{t}_{1,2}$  and  $\rho_{1,2}$ , respectively. And since it only takes a change in orientation to obtain the corresponding internally threaded surface, we can state that:

$$\rho_{1,2 \text{ internal}} = -\rho_{1,2} \tag{B.11}$$

$$\vec{t}_{1,2 \text{ internal}} = \vec{t}_{1,2} \tag{B.12}$$

This makes the method detailed in this thesis applicable to both internal and external threads.

## B.1 Numerical application

In order to verify the equations proposed earlier, we implemented them in a Matlab program which draws the surface geometry, as shown in Fig. B.1. The figure was obtained by simulating a threaded shaft with a profile based on Eq. 1.22 and the parameters presented in table B.1.

$r$	$l$	$n$	$\alpha_n$	$r_B$	$\gamma$	$r_m$	$\theta_m$	$z_m$
5mm	2mm	1	45°	$\frac{r}{\sin \alpha_n} = 7.07\text{mm}$	1	5.0178mm	-172.7935°	-1.4778 mm

Table B.1: Surface parameters and chosen point coordinates used for drawing Fig. B.1

As it can be seen from the figure, the principal directions of curvature  $\vec{t}_1$  and  $\vec{t}_2$  are perpendicular at the randomly chosen point on the surface. However, they point in directions which cannot be easily guessed without performing the calculation. This is contradictory to the ideas proposed by other authors who studied principal curvatures in the context of roller screws. Jones and Velinsky [33], for example, assume that  $\vec{t}_2$  is along the thread's helix, while  $\vec{t}_1$  is contained in the normal plane, where we defined the profile shape. Ma et al. [12] do not give specific details for the principal directions, but calculate curvatures using a different approach. A comparison with both the results obtained in [33] and [12] is given in table B.2. In all cases, the same geometry was used, i.e. the one described in table B.1.

The Gaussian curvature  $\mathcal{K}$  and mean curvature  $\mathcal{H}$  used in reference [33] are defined using the fundamental coefficients as:

$$\mathcal{K} = \frac{LN - M^2}{EG - F^2}; \quad \mathcal{H} = \frac{2FM - (EN + GL)}{2(EG - F^2)} \tag{B.13}$$

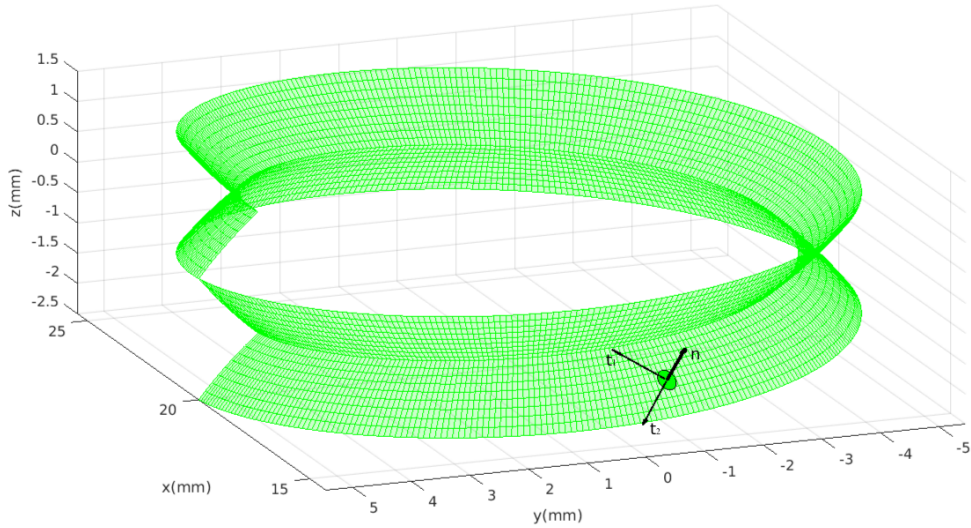


Figure B.1: Principal directions of curvature at a chosen point on the threaded surface

As pointed out by the results in table B.2, we obtain identical values in terms of principal curvatures with reference [33] when the same fundamental coefficients are used. This validates both methods. In terms of principal directions, however, our solution is different. Even though it is less intuitive, we believe it to be more systematic and general, since it was calculated using fundamental properties of differential geometry, instead of assuming it from the start.

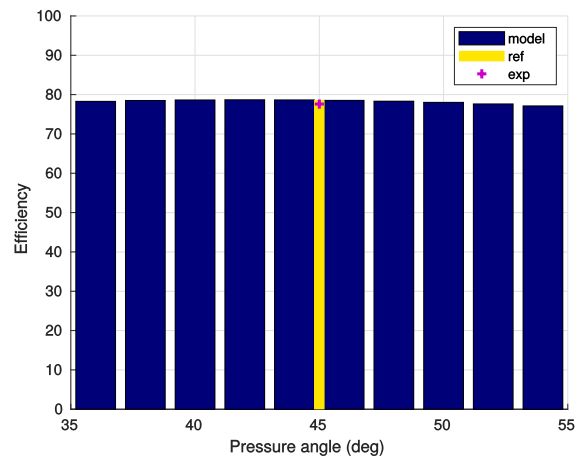
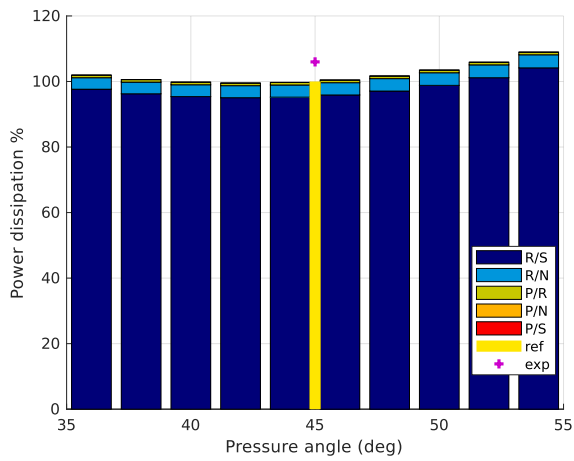
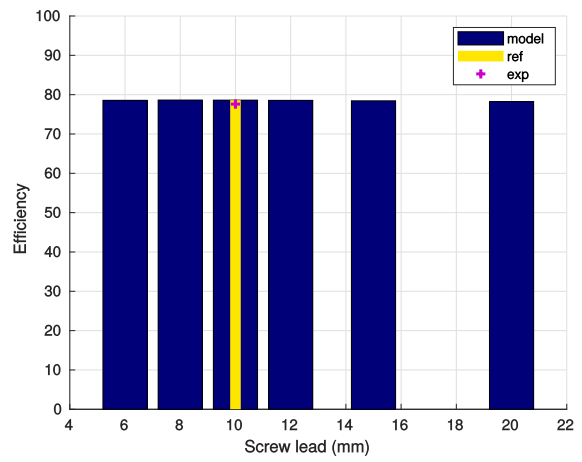
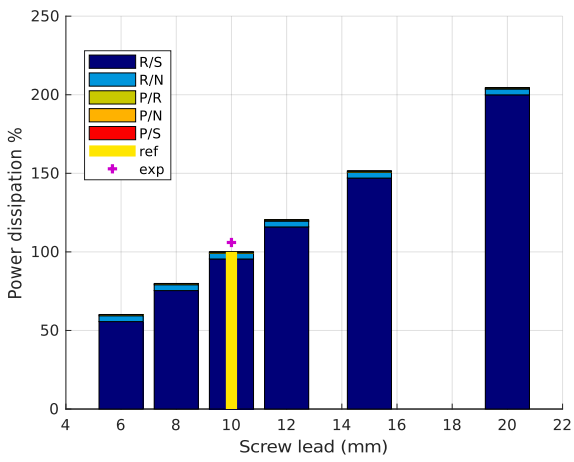
The fact that we obtain different principal directions has a direct impact on the orientation of the contact ellipse with respect to the relative surface velocity vector. This might be important if lubrication calculations are to be performed on these elliptical contacts, as the principal axes of the ellipse will generally not be aligned with the sliding velocity direction.

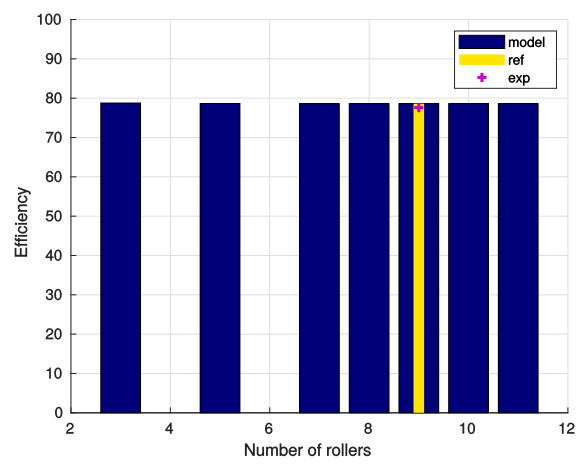
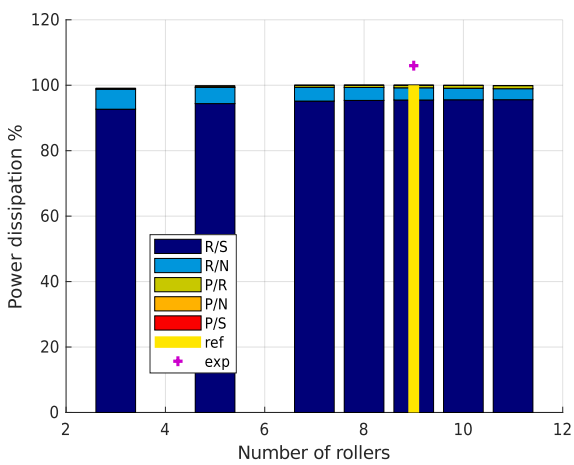
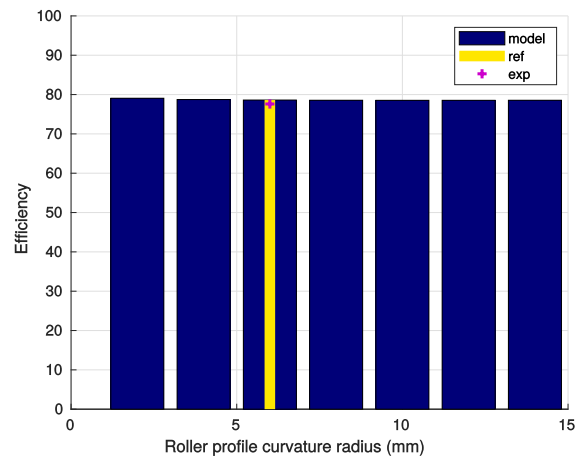
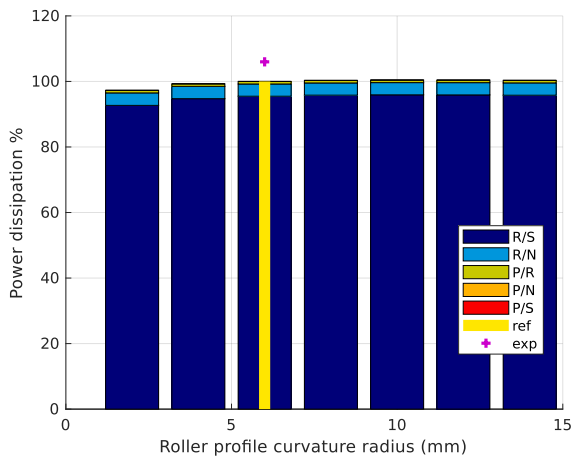
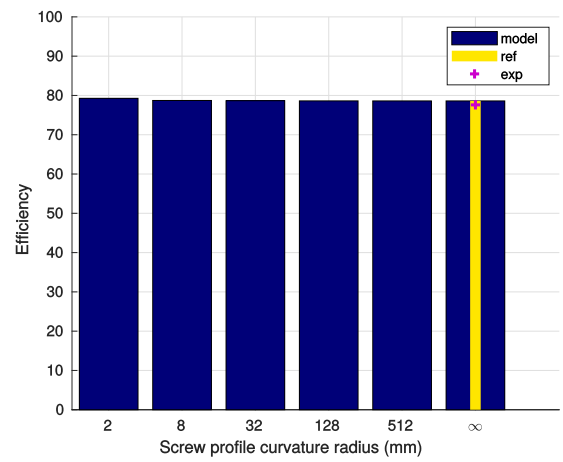
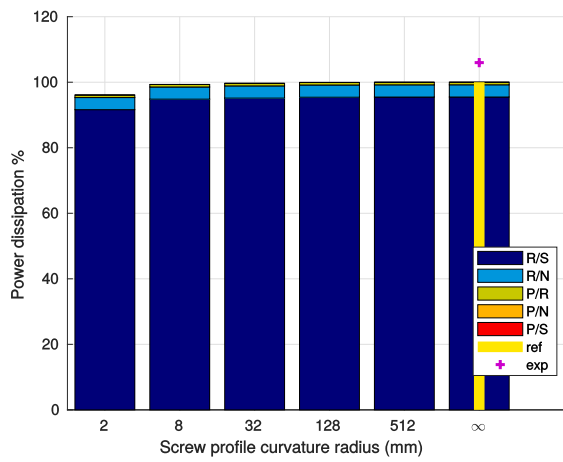
	$\rho_1$		$\rho_2$	
	formula	value ( $\text{mm}^{-1}$ )	formula	value ( $\text{mm}^{-1}$ )
current work	Eq. B.5	0.1289	Eq. B.5	0.1542
Jones & Velinsky [33]	$\mathcal{H} - \sqrt{\mathcal{H}^2 - \mathcal{K}}$	0.1289	$\mathcal{H} + \sqrt{\mathcal{H}^2 - \mathcal{K}}$	0.1542
Ma et al. [12]	$1/r_B$	0.1414	$1/r_B$	0.1414

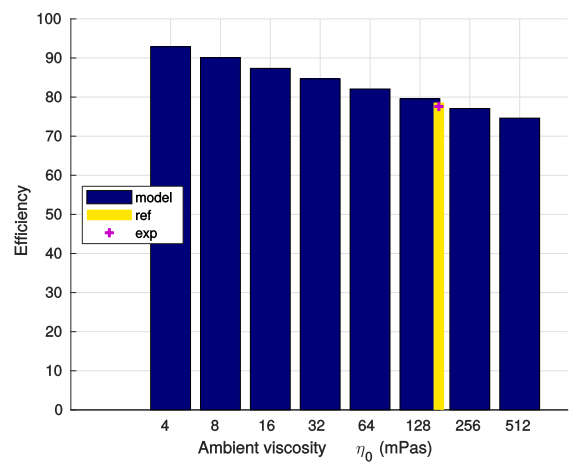
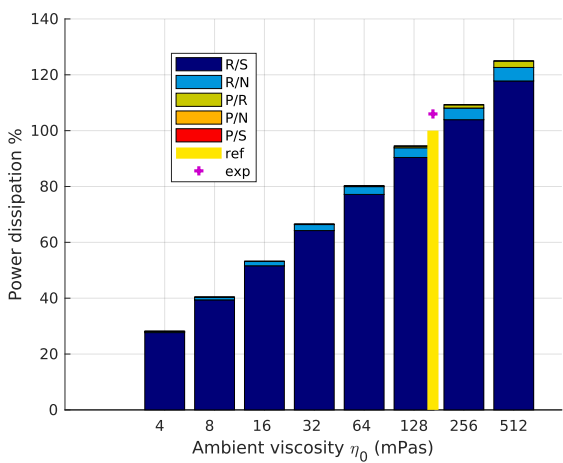
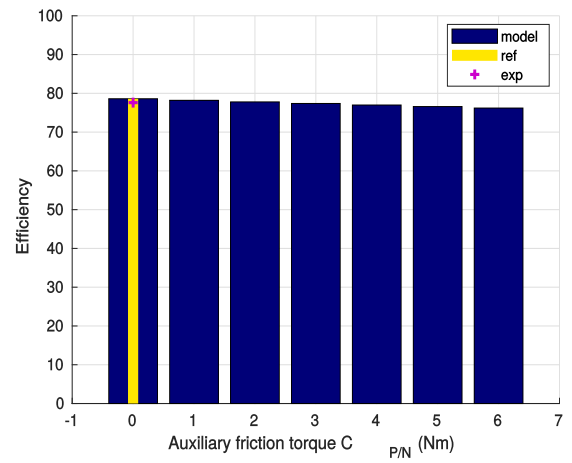
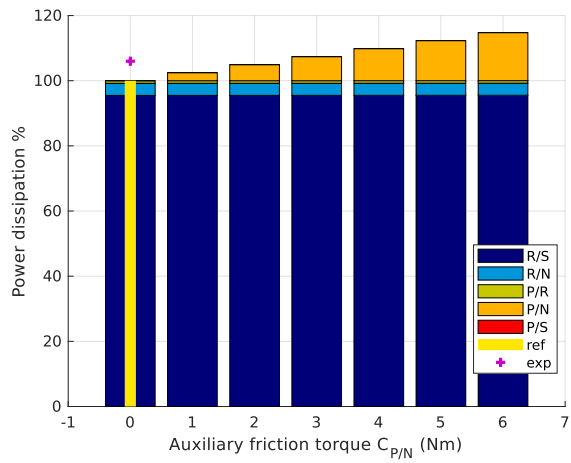
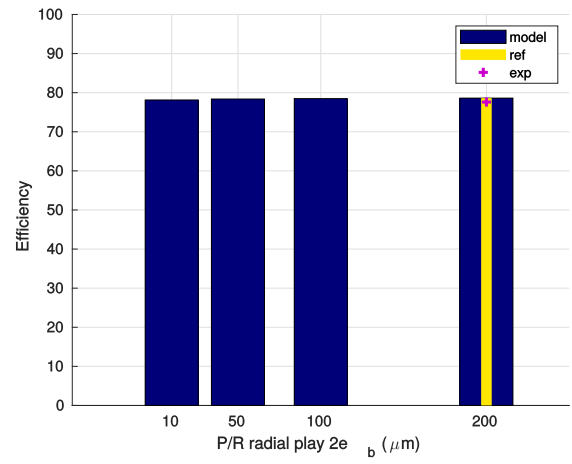
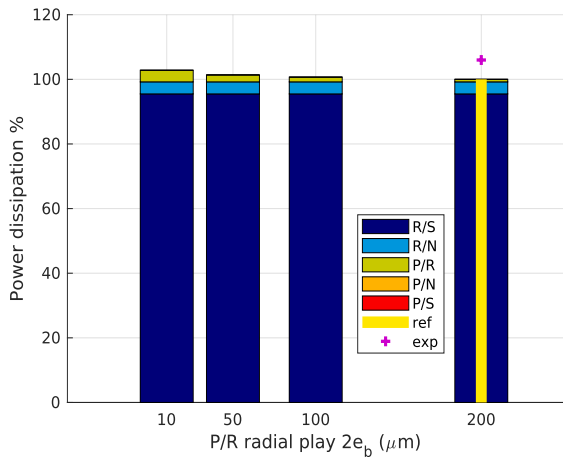
Table B.2: Principal curvature results - Comparison with literature

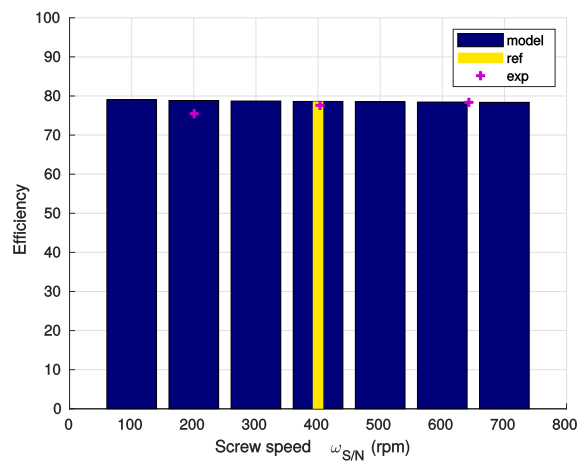
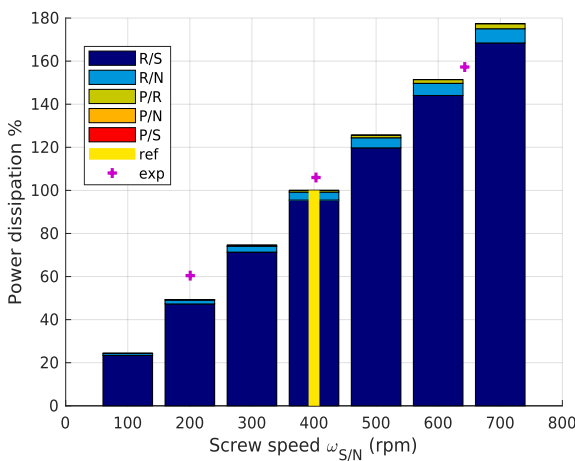
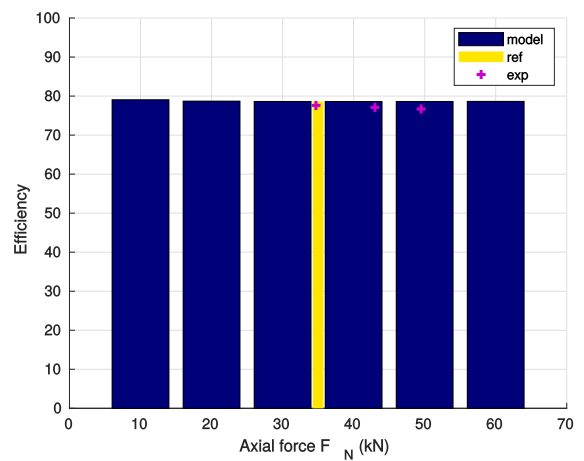
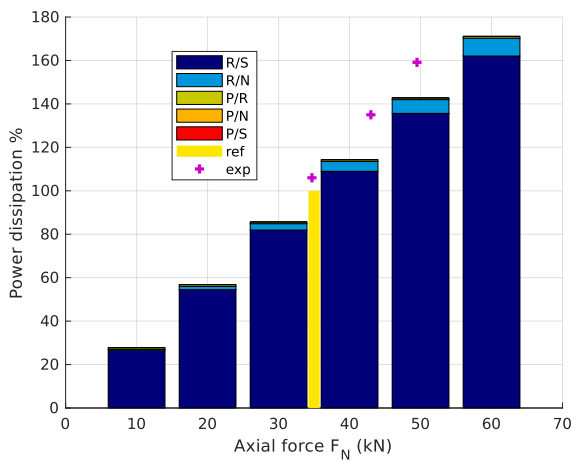
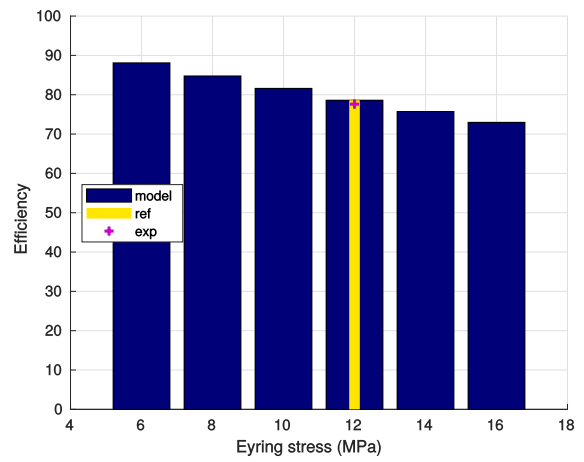
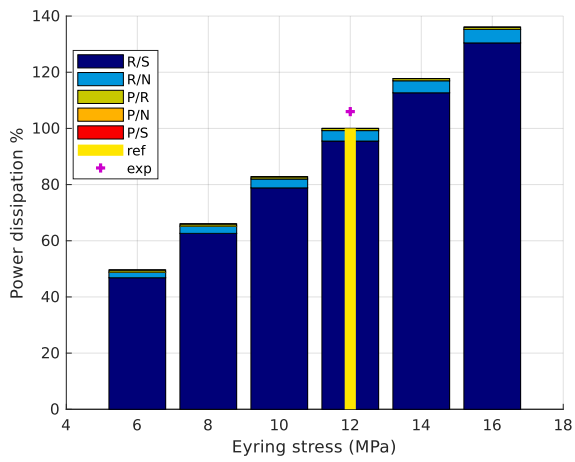
# Appendix C

## Parametric study figures









# Bibliography

- [1] SKF Group, 148 rue Felix Esclangon, 73024 Chambéry, France, Roller screws, product catalog (04 2014).
- [2] S. A. Velinsky, B. Chu, T. A. Lasky, Kinematics and efficiency analysis of the planetary roller screw mechanism, *ASME Journal of Mechanical Design* 131 (1) (2009) 011016.
- [3] C. B. Strandgren, Rolling on rollers for helical or circular movement, Nice, France, patent FR 888,281 (in French) (08 1943).
- [4] C. B. Strandgren, Perfected roller rolling device for helical or circular movement, Paris, France, patent FR 995,011 (in French) or US 2,683,379 (in English) (08 1951).
- [5] C. B. Strandgren, Perfected screw and nut device, Paris, France, patent FR 1,130,790 (in French) (10 1956).
- [6] C. B. Strandgren, Perfected roller rolling device for helical movement, Paris, France, patent FR 1,199,429 (in French) (06 1959).
- [7] C. B. Strandgren, Screw and nut device with threaded satellite rollers, Saint-Etienne, France, patent FR 1,345,893 (in French) or US 3,173,304 (in English) (11 1963).
- [8] C. B. Strandgren, Roller rolling device, Saint-Etienne, France, patent FR 1,361,431 (in French) (04 1964).
- [9] C. B. Strandgren, Screw and nut device with threaded satellite rollers, by mail, patent FR 1,477,775 (in French) (03 1967).
- [10] F. Abevi, Developing a pre-dimensioning assistance tool for satellite roller screws under complex loading conditions, Ph.D. thesis, University of Toulouse, France, (in French) (2013).
- [11] S. Sandu, N. Biboulet, D. Nelias, F. Abevi, An efficient method for analyzing the roller screw thread geometry, *Mechanism and Machine Theory* 126 (2018) 243–264.
- [12] S. Ma, G. Liu, R. Tong, X. Zhang, A new study on the parameter relationships of planetary roller screws, *Mathematical Problems in Engineering* 2012 (2012) 1–29, article ID 340437.
- [13] Y. Liu, J. Wang, H. Cheng, Y. Sun, Kinematics analysis of the roller screw based on the accuracy of meshing point calculation, *Mathematical Problems in Engineering* 2015 (2015) 1–10, article ID 303972.
- [14] S. Sandu, N. Biboulet, D. Nelias, F. Abevi, Analytical prediction of the geometry of contact ellipses and kinematics in a roller screw versus experimental results, *Mechanism and Machine Theory* 131 (2018) 115–136.
- [15] M. H. Jones, S. A. Velinsky, Kinematics of roller migration in the planetary roller screw mechanism, *ASME Journal of Mechanical Design* 134 (1) (2012) 061006.
- [16] D.-W. Zhang, S.-D. Zhao, New method for forming shaft having thread and spline by rolling with round dies, *International Journal of Advanced Manufacturing Technology* 70 (2014) 1455–1462.

- [17] D.-W. Zhang, S.-D. Zhao, S.-B. Wu, Q. Zhang, S.-Q. Fan, J. Li, Phase characteristic between dies before rolling for thread and spline synchronous rolling process, *International Journal of Advanced Manufacturing Technology* 81 (2015) 513–528.
- [18] S. Ma, T. Zhang, G. Liu, R. Tong, X. Fu, Kinematics of planetary roller screw mechanism considering helical directions of screw and roller threads, *Mathematical Problems in Engineering* 2015 (2015) 1–11, article ID 459462.
- [19] M. Mamaev, V. Morozov, O. Fedotov, V. Filimonov, Precision of a roller screw actuator transmission for a radio telescope, *Russian Engineering Research* 35 (12) (2015) 919–923.
- [20] M. Mamaev, V. Morozov, O. Fedotov, V. Filimonov, Harmonic analysis of the kinematic error in a planetary roller screw, *Russian Engineering Research* 36 (7) (2016) 515–519.
- [21] A. S. Tselishchev, I. S. Zharov, Elastic elements in roller-screw mechanisms, *Russian Engineering Research* 28 (11) (2008) 1040–1043.
- [22] J. Rys, F. Lisowski, The computational model of the load distribution between elements in a planetary roller screw, *Journal of Theoretical and Applied Mechanics* 52 (3) (2014) 699–705.
- [23] F. Abevi, A. Daidie, M. Chaussumier, M. Sartor, Static load distribution and axial stiffness in a planetary roller screw mechanism, *ASME Journal of Mechanical Design* 138 (1) (2015) 012301.
- [24] F. Abevi, A. Daidie, M. Chaussumier, S. Orieux, Static analysis of an inverted planetary roller screw mechanism, *ASME Journal of Mechanisms and Robotics* 8 (4) (2016) 041020.
- [25] S. Ma, G. Liu, R. Tong, X. Fu, A frictional heat model of planetary roller screw mechanism considering load distribution, *Mechanics Based Design of Structures and Machines* 43 (2015) 164–182.
- [26] M. H. Jones, S. A. Velinsky, Stiffness of the roller screw mechanism by the direct method, *Mechanics based design of structures and machines* 42 (1) (2014) 17–34.
- [27] W. Zhang, G. Liu, R. Tong, S. Ma, Load distribution of planetary roller screw mechanism and its improvement approach, *Proceedings of the Institution of Mechanical Engineers, Part C: Journal of Mechanical Engineering Science* 230 (18) (2016) 3304–3318.
- [28] X. Fu, G. Liu, R. Tong, S. Ma, T. C. Lim, A nonlinear six degrees of freedom dynamic model of planetary roller screw mechanism, *Mechanism and Machine Theory* 119 (2018) 22–36.
- [29] G. Auregan, V. Fridrici, P. Kapsa, F. Rodrigues, Experimental simulation of rolling-sliding contact for application to planetary roller screw mechanism, *Wear* 332-333 (2015) 1176–1184.
- [30] G. Auregan, V. Fridrici, P. Kapsa, F. Rodrigues, Wear behavior of martensitic stainless steel in rolling-sliding contact for planetary roller screw mechanism: Study of the wc/c solution, *Tribology Online* 11 (2) (2016) 209–217.
- [31] P. A. Sokolov, D. S. Blinov, O. A. Ryakhovskii, E. E. Ochkasov, A. Y. Drobizheva, Promising rotation-translation converters, *Russian Engineering Research* 28 (10) (2008) 949–956.
- [32] S. Ma, G. Liu, G. Qiao, X. Fu, Thermo-mechanical model and thermal analysis of hollow cylinder planetary roller screw mechanism, *Mechanics Based Design of Structures and Machines* 43 (2015) 359–381.
- [33] M. H. Jones, S. A. Velinsky, Contact kinematics in the roller screw mechanism, *ASME Journal of Mechanical Design* 135 (7) (2013) 051003.

- [34] Y. Liu, Y. Shang, J. Wang, Mathematical analysis of the meshing performance of planetary roller screws applying different roller thread shapes, *Advances in Mechanical Engineering* 9 (5) (2017) 1–11.
- [35] X. Fu, G. Liu, S. Ma, R. Tong, T. C. Lim, A comprehensive contact analysis of planetary roller screw mechanism, *ASME Journal of Mechanical Design* 139 (1) (2017) 012302.
- [36] M. Fedosovsky, S. Aleksanin, R. Puctozarov, Use of numerical method for determination of contact points position in roller screw threads, *Biosciences Biotechnology Research Asia* 12 (2015) 721–730.
- [37] V. V. Morozov, V. I. Panyukhin, A. V. Zhdanov, Increasing the load capacity and rigidity of roller-screw mechanisms by adjusting the screw surfaces, *Russian Engineering Research* 36 (5) (2016) 345–351.
- [38] Y. Hojjat, M. Agheli, A comprehensive study on capabilities and limitations of roller-screw with emphasis on slip tendency, *Mechanism and Machine Theory* 44 (2009) 1887–1899.
- [39] K. Johnson, *Contact mechanics*, 9th Edition, Cambridge University Press, 1985.
- [40] B. Hamrock, D. Dowson, Isothermal elastohydrodynamic lubrication of point contacts: Part iii—fully flooded results, *ASME Journal of Lubrication Technology* 99 (2) (1977) 264–275.
- [41] B. Hamrock, D. Brewe, Simplified solution for stresses and deformations, *ASME Journal of Lubrication Technology* 105 (2) (1983) 171–177.
- [42] J.-F. Antoine, C. Visa, C. Sauvey, G. Abba, Approximate analytical model for hertzian elliptical contact problems, *ASME Journal of Tribology* 128 (2006) 660–663.
- [43] T. A. Harris, M. N. Kotzalas, *Rolling Bearing Analysis*, 5th Edition, Taylor and Francis, 2007.
- [44] M. H. Jones, S. A. Velinsky, T. A. Lasky, Dynamics of the planetary roller screw mechanism, *ASME Journal of Mechanisms and Robotics* 8 (1) (2016) 014503.
- [45] C. Barus, Isothermals, isopiestic and isometrics relative to viscosity, *Am. J. of Science* 45 (1893) 87–96.
- [46] C. J. A. Roelands, Correlational aspects of the viscosity temperature - pressure relationship of lubricating oils, Ph.D. thesis, Technical University Delft, The Netherlands (1966).
- [47] B. Jacod, C. H. Venner, P. M. Lugt, A generalized traction curve for ehl contacts, *ASME Journal of Tribology* 123 (2001) 248–253.
- [48] J. Frene, D. Nicolas, B. Degueurce, D. Berthe, M. Godet, *Hydrodynamic lubrication - Bearings*, Editions Eyrolles, 1990, (in French).
- [49] A. Pressley, *Elementary Differential Geometry*, 2nd Edition, Springer, 2010.







## FOLIO ADMINISTRATIF

### THÈSE DE L'UNIVERSITÉ DE LYON OPERÉE AU SEIN DE L'INSA LYON

NOM : SANDU

DATE de SOUTENANCE : 07 Décembre 2018

Prénoms : Sebastian

TITRE : Developing a power dissipation model for planetary roller screws

NATURE : Doctorat

Numéro d'ordre : 2018LYSEI096

École doctorale : MEGA

Spécialité : Mécanique

#### RÉSUMÉ :

Les vis à rouleaux convertissent la rotation en translation de manière très efficace et sont utilisées dans des nombreuses industries. Mais même s'il présente beaucoup d'avantages, le mécanisme reste complexe et relativement difficile à comprendre. Le principal but de cette thèse est de quantifier la puissance dissipée par les vis à rouleaux standard et inversées, qui est un résultat important pour toute étude liée à l'efficacité ou la distribution de température. De plus, il s'agit d'un critère de conception dans le choix de paramètres optimaux pour une certaine application.

À cause des travaux peu nombreux en termes de recherche et des hypothèses restrictives faites dans la littérature courante, ce mémoire commence avec une analyse géométrique de base du mécanisme et envisage de généraliser les équations des surfaces filetées pour les différents types de profils et conditions de jeu. La position des points de contact peut ensuite être déduite avec un algorithme de type Newton-Raphson très rapide. Cette information est cruciale pour toute étude ultérieure de force. Après, les équations classiques de Hertz sont adaptées à des contacts peu conformes pour déterminer la forme, les dimensions et l'orientation des ellipses de contact rouleau-vis et rouleau-douille. Il est prouvé que les directions principales de courbure obtenues ici par géométrie différentielle sont différentes de celles supposées dans les précédents travaux de recherche.

Ensuite, la cinématique du mécanisme est étudiée avec un modèle stationnaire, qui établit des liens entre les mouvements uniformes de tous les composants et permet de calculer d'une manière simplifiée le champ de vitesse de glissement en tout point de l'aire de contact. Le mouvement local apparaît comme une combinaison de spin et de glissement uniforme. Le modèle est calibré sur un seul degré de liberté qui prend la forme d'un quotient de glissement, qui dépend de conditions de lubrification et équations d'équilibre dynamique. Un banc expérimental est conçu pour mesurer ce quotient et permettre donc la comparaison avec des valeurs numériques, ainsi que les quelques modèles analytiques disponibles dans la littérature. Les résultats montrent que les mesures sont très proches des conditions de fonctionnement idéales, ce qui fait que les propriétés du lubrifiant et les coefficients de frottement deviennent les paramètres les plus influents dans le peu de marge disponible pour l'amélioration cinématique.

Finalement, un modèle numérique en forces est développé et permet de calculer la puissance dissipée pendant l'équilibre stationnaire. L'algorithme itératif détermine d'abord le quotient de glissement atteint à l'équilibre et utilise ensuite le résultat pour déduire les autres variables cinématiques et dynamiques liées au calcul. Une étude paramétrique est réalisée dans le but d'identifier les facteurs importants pour l'efficacité et la puissance dissipée, ainsi que leur contribution relative.

**MOTS-CLÉS :** contact filet, quotient de glissement, couple de spin, puissance dissipée, vis à rouleaux

Laboratoire de recherche : Laboratoire de Mécanique des Contacts et des Structures  
UMR CNRS 5259 - INSA de Lyon  
Bâtiment Sophie Germain, Av. Jean Capelle  
69621 Villeurbanne Cedex FRANCE

Directeurs de thèse: Daniel Nelias et Nans Biboulet

Président du jury : Jean-Marc Linares

Composition du jury : Guingand, Michele  
Maré, Jean-Charles  
Linares, Jean-Marc  
Jones, Matthew  
Biboulet, Nans  
Nelias, Daniel  
Giraudeau, Jean-Paul